# INFORMATION TO USERS

This manuscript has been reproduced from the microfilm master. UMI films the text directly from the original or copy submitted. Thus, some thesis and dissertation copies are in typewriter face, while others may be from any type of computer printer.

**The quality of this reproduction is dependent upon the quality of the copy submitted.** Broken or indistinct print, colored or poor quality illustrations and photographs, print bleedthrough, substandard margins, and improper alignment can adversely affect reproduction.

In the unlikely event that the author did not send UMI a complete manuscript and there are missing pages, these will be noted. Also, if unauthorized copyright material had to be removed, a note will indicate the deletion.

Oversize materials (e.g., maps, drawings, charts) are reproduced by sectioning the original, beginning at the upper left-hand corner and continuing from left to right in equal sections with small overlaps.

# UMI®

University of Alberta

CORRELATIONS BETWEEN SEISMIC AND MAGNETIC SUSCEPTIBILITY ANISOTROPY
IN SERPENTINIZED PERIDOTITE

by

Zhigang Han

©

A thesis submitted to the Faculty of Graduate Studies and Research in partial fulfillment of
the

requirements for the degree of **Master of Science**

in

Geophysics

Department of Physics

Edmonton, Alberta

*Fall 2005*

**Canada**

To my parents, my wife Ruth, and my daughter Martha.

# Abstract

Rock fabrics deduced from either the anisotropy of magnetic susceptibility (AMS) or of seismic anisotropy have been widely discussed. Ophiolite from the Pindos and Vourinos Island in Greece is to be explored if there are some correlations between these characteristics. Laboratory measurements include compressional and shear-wave velocities at confining pressures to 300 MPa, density, velocity anisotropy, and shear-wave splitting, which all generally decrease with increasing degree of serpentinization. In contrast, the $V_p/V_s$ ratio and the Poisson's ratio are inversely correlated with an increasing degree of serpentinization. Magnetic fabrics, sensitive indicators of low-intensity strain, were further obtained from AMS measurements on the same samples. The directions of acoustic and magnetic anisotropy compare favorably. These results motivate the development of additional methods to use the magnetic fabric, as deduced from simple and fast AMS measurements, as a proxy for finding the directions of elastic anisotropy in traditional ultrasonic laboratory methods.

# Ackonwledgement

First of all, I should express my sincere gratitude to my supervisors, Dr. Douglas R. Schmitt and Dr. Vadim A. Kravchinsky, for their guidance, intelligent advice, and support. Both their mentorship and friendship have made the last two years at the University of Alberta exciting and enjoyable.

I wish to thank all my committee members and Dr. C. D. Rokosh for their revisions and suggestions to my thesis, which have significantly enhanced the quality of the dissertation. I also want to thank the staff of the physics department for their help; special thanks to Lynn Chandler and Sarah Derr for their hard work in helping the graduate students in our department.

I also like to extend my appreciations to Y. Zhang, Dr. M. Mah, and other friends and fellow students in the University of Alberta for their kindness, support, and encourage. Needless to say, I will express my gratitude to M. Welz, J. Havestock, J. Mackinnon, O. Catuneanu, and D. Caird for their technical assistances. I should especially mention L. Tober, a man of experience and knowledge. He is very patient and is ready to help at any time. He always knows how to solve the unexpected questions I posed.

I am grateful to my wife Ruth, who has undertaken many of the family chores during the past few years. She has dedicated her love to our success now and in the future.

Finally, I sincerely appreciate my parents and brother for all their spiritual encouragement and love, even from far away, which always gave me courage and confidence during my study in Canada.

# Contents

# List of Tables

# List of Figures

# List of symbols

This list includes most symbols for the physical quantities discussed in the text. Suffixes of vector and tensor quantities take the values 1, 2, 3.

$P$ Pressure

$T$ Temperature

$\sigma_{ij}$ Component of the second order stress tensor

$c_{ijkl}$ Component of the forth-rank elasticity tensor

$\varepsilon_{ij}$ Component of the second order strain tensor

$\lambda$ and $\mu$ Lamé parameter

$\rho$ Mass density

$u_i$ The ith component of the displacement

$U_i$ Amplitude

$\nu$ Phase velocity

$\delta_{ik}$ Kronecker delta

$\Gamma_{ik}$ Component of the Kelvin-Christoffel matrix

$V_{xx}$ P-wave velocity along X-axis; Similarly, $V_{yy}$ and $V_{zz}$

$V_{xy}$ and $V_{xz}$ Two shear wave velocities propagating along the direction of X-axis and be polarized in the directions of Y- and Z-axis, respectively. Similarly, $V_{yx}$ and $V_{yz}$; $V_{zx}$ and $V_{zy}$

$V_p$ P-wave velocity

$V_s$ S-wave velocity

$A$ Velocity anisotropy

$\Delta V_s$ Shear wave splitting

$M$ Induced magnetization

$K$ Magnetic susceptibility

$H$ Inducing magnetic field

$\chi$ Mass susceptibility

$K_{ij}$ Component of the second-order magnetic susceptibility tensor

$K_1$ or $K_{max}$ Maximum susceptibility axis

$K_2$ or $K_{int}$ Intermediate susceptibility axis

$K_3$ or $K_{min}$ Minimum susceptibility axis

$P_J$ and $T$ Jelinek corrected anisotropy degree and shape parameters

$K_m = (K_1 + K_2 + K_3)/3$ The mean magnetic susceptibility

$\beta$ Serpentine ratio as estimated from density

$F_{o90}$ 90 % Fosterite

$E_{n90}$ 90 % Enstatite

# Chapter 1

# Introduction

The physical properties of earth materials generally depend on the direction from which the measurements of the properties are made; materials with such characteristics are said to be anisotropic. This anisotropy influences geophysical observations at all scales but until recently it has mostly been ignored in their analysis. However, as our concepts of earth structure and processes become more sophisticated it is important to account for such anisotropy. Two of the most important geophysical observations are of the Earth's magnetic and seismic wave fields. The magnetism and elasticity, respectively, directly influence these observations and both are anisotropic. The induced magnetic field strength of a sample will depend on the orientation of the rock fabric or minerals with respect to that of the induced magnetic field and is manifest by variations in the magnetic susceptibility with direction. This behavior has long been called the 'Anisotropy of Magnetic Susceptibility' (AMS); this characteristic of rocks is well known in rock magnetic fabric measurements. Similarly, for various reasons rocks are generally elastically anisotropic and this characteristic is manifest as variations in the speed of both P and S waves with direction and complicated further by shear wave birefringence.

Both of these properties depend to some degree on the 'texture' or 'fabric' of the rock. In the context of this thesis, we take these two terms to describe the crystallographic orientation of the mineral components. Other names for this in the literature are 'lattice preferred orientation' (LPO) or 'crystal preferred orientation' (CPO) but these essentially mean the various crystallographic orientations of each of the minerals within a rock may be described by a statistical distribution function (*Cholach*, 2005). Although there are a

1

number of methods to obtain such information including microscopic thin section analysis on universal stages (e.g. *Christensen*, 2004), X-ray or neutron goniometry (*Covey-Crump et al.*, 2003; *Ullemeyer et al.*, 2000), or electron backscatter diffraction (e.g. *Bascou et al.*, 2001), these can remain time consuming to both collect and analyze. AMS cannot directly provide such detailed fabric information, but it does have the advantage that it yields some information on the principal directions of the sample's symmetry; and this latter information is crucial in making elastic property measurements. While it has long been known that both measurements rely on the material's fabric, there have not to our knowledge been any studies that have explored the correlation between them; this thesis presents some initial results on the comparison of the anisotropy between elastic wave velocities and magnetic susceptibility in a suite of olivine-rich serpentinized peridotites from the Hellenic ophiolites of Greece.

This chapter provides some of the basic background information on the importance and causes of anisotropy of the elastic and magnetic properties in brief, particularly in the context of the oceanic crust. Some of the more general observations related to mafic and ultramafic rocks and their anisotropy will also be reviewed. As part of this it includes some discussion of ophiolite complexes in general and how they relate both geologically and geophysically to our understanding of the uppermost parts of the oceanic lithosphere. The role of serpentine minerals is also discussed.

Chapter 2 contains background information more specific to this study. This includes an overview of the Tethyan Hellenic ophiolites from which the serpeninite samples were taken. However, it must be kept in mind that this is a preliminary study which focuses on the measurement and comparison of two different physical properties, this study was not designed to solve some of the questions that arise in the first chapter but only to set the stage for future work. In this line, a number of the physical characteristics of the samples chosen are given.

The theory relating elastic wave anisotropy to the material elasticity is reviewed first in Chapter 3. This then leads to a description and the results of the laboratory measurements of both compressional and shear waves and their anisotropy under pressure. Chapter 4 follows a similar pattern but for the magnetic AMS measurements. This differing information is compared and a synopsis of the results provided in Chapter 5. As well,

2

although this work is principally motivated as a technical study comparing two physical property measurements, the results may have broader implications that are useful in our understanding of the structure of the oceanic crust. Consequently, Chapter 6 concludes with plans for future work.

## 1.1 Background

To describe the magnetism of the Earth and the magnetic fabric of rocks, knowledge of the magnetic behavior of rocks and their constituent minerals is necessary. AMS is a relatively simple measurement that provides insight of the microstructure of materials to be gained on the basis of their magnetic fabric. Consequently, the anisotropy of low field magnetic susceptibility has also being a useful tool that has been successfully used in rock fabric studies. Similarly, the seismic anisotropy of rocks depends in part on the preferential alignment of its constituent minerals. One might reasonably expect both properties to have been influenced by the rock's history, and hence, there to be some degree of correlation between the two. Consequently it may be possible to use AMS measurements as proxies for elastic wave anisotropy.

Much of our present knowledge on the deep continental crust and the upper mantle was obtained by seismic methods. In the past [see the compilation by *Holbrook et al.* (1992)], most studies of deep crustal composition have assumed the deeper crust to be elastically isotropic. The assumption of isotropy is scale sensitive and valid only in the materials with uniformly and randomly oriented minerals, microcracks, and pores. For example, even a suite of isotropic layers will overall display seismic anisotropy at long wave lengths. Use of the isotropic assumption, simplifies the construction of the Earth models based on seismic observation. However, in reality most rocks are elastically anisotropic, this anisotropy is caused by a number of different factors. Generally, seismic anisotropy is due to an ordered arrangement of elements of the rock that are small compared to the wavelengths employed. Conversely, a randomly oriented assembly of crystals is equivalent to an isotropic medium(*Helbig*, 1994). He listed a few causes for ordering of other elements:

- Preferential orientation of elongated mineral grains by the flow of melt in igneous

3

or of water in sedimentary rocks;

- Preferential settling of 'flat' phyllosilicates in still water;

- Re-orientation of mineral grain axes during compaction or phase transformation (e.g. transition of clays to illite);

- Oriented fracturing and joint production arising from anisotropic tectonic stresses;

- Ductile strain resulting from defect motion in an anisotropic stress field producing metamorphic lineation and foliation field elements;

- Preferential opening or closing of compliant cracks and pores by a non-hydrostatic stress state.

- Fine layering at a dimensional scale smaller than the seismic wavelengths that pass through the material;

As this list suggests, seismic anisotropy can result singularly or in combination from the preferential orientation of mineral grains, the presence of orientated cracks of various sizes, or the occurrence of layering that is 'thin' relative to the seismic wavelengths. These characteristics are of great interest by themselves as they reveal additional information on the Earth's structure. As our observational capabilities improve, seismic anisotropy cannot be neglected in seismic studies of the Earth's crust.

Consequently, the questions that naturally arise are related to how to evaluate the potential contribution of anisotropy in these rocks to variations in seismic velocity, what is the cause of the anisotropy, and how this anisotropy is related to the rock fabric and the mineral orientation distributions. The seismic anisotropy of metamorphic rocks depended on a variety of factors that includes mineralogical composition, metamorphic grade, the degree of texture development, and the extent of brittle deformation. Much laboratory and theoretical work has already been carried out in recent years towards a better understanding of these problems. Laboratory studies of mantle rock anisotropy have focused on (1) the magnitude and symmetry of velocity anisotropy, (2) the relative orientation between seismic properties and the structural framework, and (3) the *in situ*

structural orientation with constraints from experimental petrology and seismic observations (*Long and Christensen*, 2000).

In the present study, emphasis is placed on the intrinsic[1] seismic anisotropy caused by a pronounced fabric of highly anisotropic minerals. Research trends show that both seismic anisotropy and the causative intrinsic petrofabrics are worth trying to quantify in both the laboratory and by numerical methods. Alternatively, the development of magnetic anisotropy is characterized by its various applications. In this thesis, the P- and S-wave anisotropy of a suite of typical ophiolite samples of the same origin and extending over a wide range of degree of serpentinization have been measured in laboratory.

## 1.2 Seismic wave anisotropy

### 1.2.1 Implications of Seismic Anisotropy

The physical properties of rocks are to some extent anisotropic as demonstrated by many seismic studies, borehole logs, and laboratory measurements. In fact, anisotropy is likely a fundamental characteristic of rocks. Despite the recognition of this fact and its implications for the interpretation of geophysical observations, our understanding of the anisotropic properties of many rocks is still limited. It is important to understand the intrinsic properties of the rocks through which the seismic waves pass, because consideration of anisotropy in seismic analysis and processing will improve the interpretative power of such studies. The rocks studied here are serpentinized dunites sampled from an ophiolite, consequently in this section seismic anisotropy in the context of the oceanic crust and mantle is overviewed, the classic model of ophiolites is presented, and the role of serpentine is introduced in a general way.

It is worthwhile to briefly first mention what is meant by seismic anisotropy as it is physical phenomena that is rich with complexity. First, as already noted the velocities at which both shear and compressional waves propagate through an anisotropic material varies with direction. For example, in most rocks the compressional wave velocity will be

---

[1] The anisotropy caused by the structure of the medium (*Helbig*, 1994). That is, the anisotropy of the nonporous mineral aggregate in which the anisotropy is due primarily to the elastic properties, cement, and degree of preferential orientation of the constituent minerial grain. This is also often referred to as " lattice preferred orientation" or LPO.

---

5

larger in the plane of foliation than normal to it with the velocity changing in a continuous fashion between these principal fabric directions. Second, one further complication is that in any given direction there will be two different shear waves with differing polarizations and velocities. These differing velocities of the two shear waves is highly analogous to the birefringent effects employed in optical mineralogy. This phenomena is commonly referred to in the seismology literature as shear wave splitting (SWS) because these two waves will arrive at slightly different times. Shear wave splitting observations have been used by many workers over the last 15 years to infer the existence of anisotropy, and hence rock texture, within the earth's upper mantle (*Silver*, 1996; *Savage*, 1999).

The rocks studied in this thesis are taken from the Hellenic ophiolites and as such are interpreted as being representative of some of the rock types in the uppermost oceanic mantle. While this preliminary physical property study was not intended to focus on these rocks in this context, it is still important to note that the magnetic and elastic characteristics of such rocks are of great interest in the development of seismological models of the oceanic crust and uppermost mantle.

### 1.2.2 Some basic characteristics of seismic anisotropy

Those trained in optical mineralogy will be familiar with some of the terms of elastic anisotropy but while there are many similarities between optical and elastic anisotropy, there are also many differences. For example, cubic minerals are optically isotropic, but all minerals are elastically anisotropic. Halite (NaCl) show no optical birefringence although in most directions away from the principal crystallographic axes it will have elastic shear wave splitting and the P and S wave velocities will vary with direction too. This is because the transmission of light through the material depends primarily on the polarizability of the electron cloud surrounding the atoms while the elastic wave propagation requires physical motion of the atoms. For those who approach such problems from the mathematical perspective, optical properties may be described by a $3^{rd}$ rank tensor with up to 6 independent constants, the more complex elastic properties require a $4^{th}$ rank tensor with as many 21 independent constants.

In the context of low or vanishing porosity, an assemblage of these minerals will also be anisotropic to a degree that depends on the relative alignment, or LPO, of all its com-

posite crystals. For such crystallites, the maximum anisotropy that can be obtained is that of the single crystal itself while the lower isotropic bound would be found in a crystallite with a completely uniform orientation of all the crystallographic axes. However, a key motivation of seismic observations is to obtain knowledge of the in situ seismic velocity. The seismic P and S wave velocities and their anisotropy are related to a variety of factors including tectonic stress, pore fluid pressure, modal composition, porosity and its morphology, temperature, and crystallographic orientation statistics. Hence, knowledge of *in situ* velocities can help constrain geological structures and processes. Consequently, it is important to further understand the relationship between the rock texture and the velocity anisotropy as one factor that influences observations.

There are a large number of modeling and laboratory studies that focus on the links between elastic wave anisotropy and rock fabric but only a few key papers are mentioned here. *Birch* (1960, 1961) made a large series of measurements of compressional velocities to 1 GPa (10 kbars) demonstrating that the non-linear increase in velocity at low confining pressure could be attributed to the closure of pores, cracks and micro-fractures (*Gangi and Carlson*, 1996). Accurate interpretation of seismic velocity images of the lithosphere requires a thorough knowledge of the seismic properties of different rock types. Much laboratory[*Birch* (1960, 1961), *Nur and Simmons* (1969), *Jones and Nur* (1982, 1984), *Barruol and Kern* (1996), *Horen et al.* (1996), *Kern* (1993); *Kern et al.* (1997)] and theoretical work [*Baker and Carter* (1972), *Siegesmud et al.* (1989), *Mainprice and Silver* (1993), *Ji and Salisbury* (1993a); *Ji et al.* (1993b, 1994)] has been devoted to the nature of P- and S-wave anisotropy in a variety lithologies in both the crust and the upper mantle.

One of Birch's observations that is pertinent to this study is that of the anisotropy of compressional waves in the rocks, and in one of his dunites he made a connection between a strong orientation of the 'a' axis of olivine with the fast direction in the rock. These were followed by a series of more detailed follow-up studies by *Christensen* (1965, 1966a,b) that extended the measurements to shear waves and reinforce the observations that this anisotropy was related to the mineralogical fabric. Later, *Christensen and Ramanana* (1971) carried out more complete measurements of shear wave velocities and demonstrated the birefringent effects of the split shear waves in a given direction. *Peselnick et al.* (1974) conducted experiments on one lherzolite from the Ivrea Zone, Italy and

7

found good correlation between the observed velocities and the principal anisotropy axes calculated from orientation distributions of olivine. They also noted that olivine was the predominant source of anisotropy in these rocks; but the olivine 'a' axis differed by 15 to 10 degrees from the field lineation and foliation elements suggesting that that fastest velocities are not perfectly aligned with the field elements in these rocks. *Kern* (1993) studied the anisotropy of an Ivrea peridotite and serpentine (antigorite) bearing rock, these samples indicated that the peridotite olivine texture controlled its anisotropy. Most recently, *Pros et al.* (2003) carried out detailed compressional wave measurements of Ivrea dunites, pyroxenites, and lherzolites to 400 MPa of confinining pressure using a unique technique that relies on a spherical sample, at high pressures they found these samples to mostly retain an orthorhombic anisotropy (i.e. one with three distinct axes of symmetry). *Wendt et al.* (2003) have recently attempted to model the instrinsic properties of a harzburgite taken from the Oman ophiolite on the basis of velocity measurements made at room pressure. These are then corrected for the effects of microcrack distributions and olivine orientations but it is debatable whether or not the microcrack statistics can be ascertained with sufficient accuracy to make this approach worthwhile.

The interpretation that the intrinsic anisotropy is due to the LPO is supported by modeling that accounts for the rock's statistical mineralogic orientation distributions (*Nicholas and Christensen*, 1987; *Christensen and Crosson*, 1968; *Crosson and Lin*, 1971; *Wendt et al.*, 2003; *Mainprice and Humbert*, 1994; *Tommasi et al.*, 1999; *Kern*, 2003); *Ben-Ismail and Mainprice* (1998) and *Wenk and Van Houtte* (2004) have developed a database of olivine fabrics in rocks from a variety of locations and on this basis calculate the expected seismic anisotropy. *Wenk* (2002) has recently provided an extensive overview of this topic. *Leiss et al.* (2000) have given an overview of much of work currently underway in the field of texture.

For purposes of illustration of the role of crystallographic texture it is useful to compare the bounding cases of a single crystal (i.e. perfectly aligned) to a randomly oriented aggregate of the same mineral. A single olivine crystal has compressional wave velocities of 9.89 km/s, 7.73 km/s, and 8.43 km/s in the directions of the a, b, and c axes, respectively giving an upper bounding case of Vp anisotropy of 21.9 % (*Weiss et al.*, 1999; *Abramson et al.*, 1997). For purposes of comparison, the Hill average velocity for ran-

---

8

domly oriented aggregate of this same olivine crystal will be 8.53 km/s (*Cholach*, 2005) and recent measurements on pure fosterite of 8.534 km/s on carefully prepared pure polycrystalline fosterite samples by (*Ji and Wang*, 1999).

The effects of cracks are not crucial to this study. Nevertheless, it is important to note that the seismic anisotropy rises or decreases with confining pressure at the low-pressure range (less than 300 MPa). This is important for both the understanding of seismic observations as deviatoric stresses can induce anisotropy (*Nur and Simmons*, 1969) and because these small cracks can strongly influence the observed velocities. The closure of microcracks can either reinforce or attenuate the anisotropy due to lattice-preferred orientation of rock forming minerals (*Ji and Salisbury*, 1993a; *Ji et al.*, 1993b). If the cracks are also preferentially aligned, some forms of anisotropy symmetry are produced. Oriented cracks are also important in crustal seismic studies, and it has been suggested these are an indicator of the prevailing stress orientations in the shallow crust. The cracks are aligned in a vertical plane striking parallel to the maximum horizontal stress orientation (*Crampin*, 1978). *Crampin* (1978) showed that if the seismic wavelength is large relative to the typical crack spacing, the cracked medium is transversely isotropic with a horizontal axis of symmetry perpendicular to the plane of the cracks. As a result, it has been suggested that variability of the stress field near active faults can be monitored by changes in anisotropy. One other point with regards cracks is that their existence will bias measurements of compressional and shear wave velocities. Those workers attempting to determine the intrinsic, pore-free, properties of the rock apply high pressure to close the crack porosity as much as possible. This is the reason that high pressures are applied to the samples in the experiments to be described in Chapter 3.

### 1.2.3 Structure of the oceanic lithosphere, anisotropy, and the ophiolite model

Seismic anisotropy is observed in two different ways in the oceanic lithosphere, and this anisotropy appears to support standard models of ocean lithosphere formation. First, the upper most oceanic crust is anisotropic with a slow and fast compressional waves more or less perpendicular and parallel to the ridges, respectively. Second, the uppermost mantle also displays anisotropy but with the major difference that the fast direction for P-waves is perpendicular to the spreading ridge axes. This latter anisotropy is most im-

portant to the current study. In this section, the differing characteristics are presented, the ophiolite model of the oceanic crust is described both from the perspective of geological and seismological observations, and the current interpretations are provided.

The ridge-parallel jointing and fracturing of the uppermost sections of the oceanic crust is likely the source of anisotropy in those regions (e.g. *Dunn and Toomey*, 2001). Recent seismic measurements in the vicinity of the spreading centre of the East Pacific Rise (*Tong et al.*, 2004) show highly anisotropic behavior in the uppermost extrusive portion of the oceanic crust that becomes more muted with depth, possibly as a result of hydrothermal annealing of cracks. These crustal studies, in contrast to those that attempt to examine the uppermost mantle below, typically display the highest velocities parallel to the oceanic ridge axis consistent with the expectation of ridge-parallel fracturing and jointing.

With regards to the uppermost mantle, even the earliest refraction studies of the seismic structure of the oceans, discussed by *Hess* (1964), displayed high upper mantle velocities in directions parallel to the fractures zones (i.e. perpendicular to the ridge in contrast with the shallower crustal layers). Early seismic observations in the oceans produced refraction profiles that were suggestive of a simple 'pseudo-stratigraphic' layered structure, and given the sophistication of the tools available in the 1950's and 1960's were interpreted as such with major layers 1 through 4 determined on the basis of the observed seismic traveltimes. Anisotropy has since been confirmed by many authors. *Gaherty et al.* (2004) detected an a compressional wave anisotropy of only 3.4 ± 0.3 % near the slow-spreading Mid-Atlantic Ridge which is less than the 5.5 % observed by *Shearer and Orcutt* (1986) in more rapidly created Pacific lithosphere and earlier but less certain measurements of anisotropy ranging as high as 8 % in older Pacific uppermost mantle. These results suggest there is some correlation between plate spreading rate and seismic anisotropy.

On the basis of some of dunite laboratory measurements (*Birch*, 1960, 1961), Hess (1964) suggested that the observed anisotropy was due to preferential alignment of olivine in sub-Moho rocks. As scientific drilling had not, and has still not, penetrated the oceanic crust to depths sufficient to actually sample the oceanic upper mantle, workers focused material property studies on samples taken from ophiolites. Ophiolites are thought to

10

be remnants of oceanic lithosphere obducted onto continental material. Ophiolites provide what is believed to be the best 'exposure' of oceanic lithosphere available to us and their study has been used to develop structural models and as further evidence of plate tectonics.

It is worth briefly reviewing some of the essentials of the ophiolite models recognizing that many features of these are somewhat simplified and that since the development of these models the detailed literature on ophiolites has expanded dramatically. Essentially, the classic oceanic crustal model was developed from the '1972 Penrose' ophiolite (*Dilek*, 2003) which consists of a layered structure beginning at the top and continuing downward with (see overview in monograph by *Coleman* (1977) and the review paper by *Christensen and Salisbury* (1975)).

1. a veneer of weakly consolidated marine sediments. This sedimentary or seismic Layer 1 has a low seismic Vp varying from 1.5 km/s to 3.4 km/s and is on average 0.3 km thick although this can vary widely depending on a variety of factors the most important of which is the age of the seafloor.

2. an igneous extrusive sequence characterized by the existence of basaltic submarine pillow lavas and sheet flows. The magnetic remnance of this layer produces the age dependent magnetic striping of the sea floor. This extrusive is often associated with seismic Layer 2 with an average velocity of $5.04 \pm 0.69$ km/s and thickness of $1.39 \pm 0.5$ km. It is worth noting that some workers (see *Christensen and Salisbury* (1975) will further delineate this into Layers 2A and 2B. The velocity of layer 2A generally increases with age to about 10 Ma and this increase is likely evidence for hydrothermal alteration (*Carlson*, 1998; *Grevemeyer and Weigel*, 1997). An alternative view is that Layer 2 is instead characterized by a high gradient in the velocity as observed in ODP Hole 504B which has drilled more than 2.1 km beneath the sea floor (e.g. *Detrick et al.*, 1994) which is likely due to progressively increasing degrees of hydrothermal alteration with depth (*Salisbury et al.*, 1996).

3. a series of mafic intrusives often linked to seismic Layer 3. This layer is distinguished by a much more gradual increase of velocity with depth and by remarkably uniform velocities in all the observations with a range of $6.73 \pm 0.19$ km/s

and 3.75 ± 0.03 km/s for the compressional and shear wave refraction velocities, respectively. The average thickness of this layer is 4.97 ± 1.25 km. Classic interpretations correlate the top of this intrusive with diabase sheeted-dyke sequence and the bottom with massive gabbro presumed to have formed from a upper parts of a cooling magma chamber at the mid-ocean ridge. *Christensen and Salisbury* (1975) point out the transition from the sheeted dikes to the massive gabbro is not sharp as this oversimplified layered model might suggest. A layered sequence of ultramafic cumulates possibly indicative of settling of the heavy minerals from a cooling magma chamber occurs at the bottom of this sequence. Velocities in the cumulate layer of 7.0 - 7.2 km/s have been observed in the horizontal direction and as high as 7.4 km/s vertically in the laboratory.

4. the upper and seismologically anisotropic mantle consisting chiefly of ultramafic dunites, harzburgites, and lherzolites. These peridotitic rocks overlie metamorphosed country rocks across a fault contact. In an ophiolite, the mean seismic velocity in Layer 4 increases rapidly from Layer 3 to 8.13 ± 0.24 km/s. Shear wave velocity measurements are more difficult to obtain but *Shearer and Orcutt* (1986) obtained values of 4.65 ± 0.1 km/s in both directions suggestive of a low S-wave anisotropy; *Au and Clowes* (1982) found similarly low S-wave anisotropy. It is from this section of the ophiolite that the rocks studied here were sampled. Rocks from this zone provide some of the most important observations that link texture to uppermost mantle seismic anisotropy, discussion of these earlier studies is delayed to the next section.

This model is not perfect or complete and there are a variety of structural styles seen that do not fit. For example, one large discrepancy is the observation that the geochemical signatures of many ophiolites differ from modern mid-ocean ridge basalts; this information has even been used by *Moores et al.* (2000) as partial evidence for age dependent variations in the regions of the mantle serving as the source of material for the mid-ocean ridges.

Further, there are certainly problems with trying to too strictly tie seismic refraction observations suggestive of a layered structure to structural and petrological changes. In-

12

deed, it is important to point out that the Layer 2/3 boundary may not be simply associated with the transition between the extrusives and intrusives but could instead be related to differences in porosity with depth as suggested by *Detrick et al.* (1994) on the basis of observations in the deepest oceanic scientific wellbore or variations in metamorphic grade as suggested by *Christensen and Smewing* (1981). Further, in this classic ophiolite model the seismological Moho would more likely coincide with the top of the ultramafic cumulate layers that are composed of fast materials while the petrological Moho would more properly be placed at the base of this cumulate layer produced in a magma chamber in contrast to the underlying mantle peridotites.

There have been a number of detailed laboratory studies of velocities from ophiolites because despite the fact they have experienced substantial deformation during obduction onto the continental material they are still the only candidate rocks that can be placed in the pseudo-stratigraphy of a classic ocean lithosphere concept.

The Bay of Islands, Newfoundland, opiolite complex was studied in two complementary papers. *Salisbury and Christensen* (1978) measured P and S wave velocities on an extensive series of rock samples as a function of the original estimated depth through the crustal section. Due to the serpentinization of the ultramafic samples and under the assumption that this alteration occurred during obduction of the ophiolite, to obtain values for 'fresh' unaltered material they would expect on the basis of the ultramafic mineral modes instead calculated the velocities. The calculations were carried out under the assumption of isotropy and no information on anisotropy was obtained. This was remedied in *Christensen and Salisbury* (1979) where they noted from petrographic analysis with that the olivine a axis in the ultramafics was preferentially aligned roughly normal to the sheeted dikes with the b and c axes in the plane of the dikes. Olivine composed more than 85 % of these rocks and on this basis they assumed the anisotropy was predominantly controlled by this alignment yielding anisotropies of 5-6 % for the P-waves. Many of these observations were confirmed in a similar study of the Oman ophiolite by *Christensen and Smewing* (1981). Again, the pervasive serpentinization of the ultramafic rocks necessitated that the velocities be calculated from observed petrographic orientation of the unaltered ultramafic minerals; it is important to look at this in more detail.

13

### 1.2.4 Serpentinization and seismic velocity

First, however, it is important to introduce the process of serpentinization as its presence, or lack of presence depending on the model assumed, will substantially influence the interpretation of seismic data. Serpentinization refers to the hydrothermal alteration of the olivine and pyroxene in peridotite to brucite, talc, magnetite, tremolite, and the serpentine minerals (lizardite, clinochrysotile). Some of the basic reactions are (*Allen and Seyfried*, 2003):

$$2Mg_2SiO_4 + 3H_2O = Mg_3Si_2O_5(OH)_4 + Mg(OH)_2 \qquad (1.1)$$

$$Forsterite \qquad = serpentine \qquad + brucite$$

$$3Fe_2SiO_4 + 2H_2O = 2Fe_3O_4 + 3SiO_2(aq) + 2H_2(aq) \qquad (1.2)$$

$$Fayalite \qquad = Magnetite$$

$$6MgSiO_3 + 3H_2O = Mg_3Si_2O_5(OH)_4 + Mg_3Si_4O_{10}(OH)_2 \qquad (1.3)$$

$$Enstatite \qquad = serpentine \qquad + Talc$$

$$2CaMgSi_2O_6 + 6MgSiO_3 + 3H_2O = CaMg_5Si_8O_{22}(OH)_2 + Mg_3Si_2O_5(OH)_4 \qquad (1.4)$$

$$Diopside \qquad + Enstatite \qquad = Tremolite \qquad + serpentine$$

$$3FeSiO_3 + H_2O = Fe_3O_4 + H_2(aq) + 3SiO_2(aq) \qquad (1.5)$$

$$Ferrosilite \qquad = Magnetite$$

14
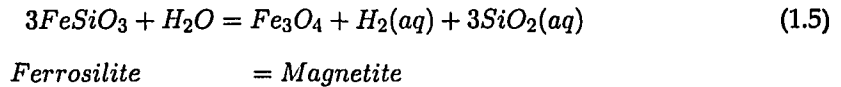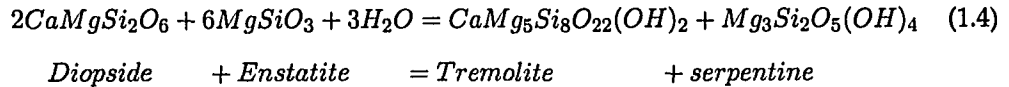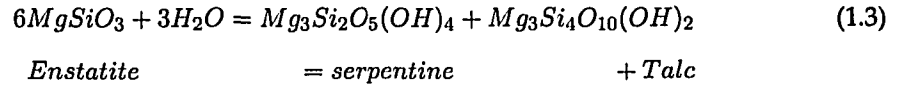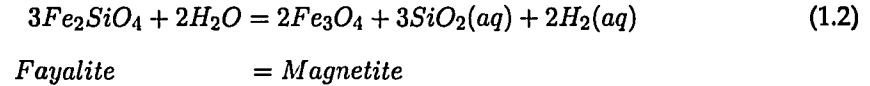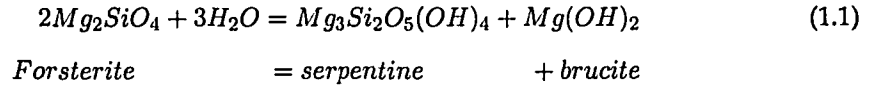
Table 1.1: Density, symmetry, and chemical formula of minerals present in the samples

|  | Mineral | Symmetry | Formula | Density $(Mg/m^3)$ |
|---|---|---|---|---|
| Olivine | Forsterite | Ortho. | $Mg_2SiO_4$ | 3.221 |
| Olivine | Fayalite | Ortho. | $Mg_2SiO_4$ | 4.38 |
| Pyroxene | Enstatite | Ortho. | $(Mg, Fe)SiO_3$ | 3.198 |
| Pyroxene | Ferrosilite | Ortho. | $FesiO_3$ | 4.002 |
| Pyroxene | Augite | Mono. | $(Ca, Mg, Fe)_2(Si, Al)_2O_6$ | 3.32 |
| Pyroxene | Diopside | Mono. | $CaMgSi_2O_6$ | 3.31 |
| Amphibole | Hornblende | Mono. | $Ca_2(Mg, Fe, Al)_5(Si, Al)_8O_{22}(OH)_2$ | 3.12 |
| Amphibole | Tremolite | Mono. | $Na_{0.5}Ca_2Mg_5Si_8O_{22}(OH)_2$ | 3.01 |
| Hydroxides | Brucite | Rhombo. | $Mg(OH)_2$ | 2.38 |
| Chlorite | Clinochlore | Tri. | $(Mg, Al)_6(Si, Al)_4O_{10}(OH)_8$ | 2.7 |
| Talc and Pyrophylite | Talc | Tri. | $Mg_3Si_4O_{10}(OH)_2$ | 2.776 |
| Serpentine | Lizardite | Hexa. | $Mg_3Si_2O_5(OH)_4$ | 2.5 |
| Serpentine | Clinochrysotile | Mono. | $Mg_3Si_2O_5(OH)_4$ | 2.55 |
| Spinel Oxides | Magnetite | Cubic | $Fe_3O_4$ | 5.206 |

Note that these are end-member formulas and in reality the olivine and pyroxenes will contain about 90 % Mg and 10 % Fe. Recognizing that the serpentine reactions are complex, authors prefer to just simply state that olivine + water = serpentine ± brucite ± magnetite to give the general sense of what is produced.These reactions typically occur over the temperature range of $100^oC$ to $500^oC$. Further details of the serpentinization process may be found in *O'Hanley* (1996), but it is worth pointing out that this remains a very active area of research in many areas of the earth sciences because the serpentine minerals are one way to introduce water into the earth's crust at subduction zones and because the release of $H_2$ has important biological implications. The 'Lost City' hydrothermal vents that were accidently discovered are one place where biological activity may depend on the hydrogen released during serpentinization.

Some of the characteristics of these various minerals are given in Table 1.1 (*Bass*, 1995; *Nickel and Nichols*, 1991). The chemistry of the various serpentine minerals is the same but there are substantial differences in the morphology of the 'crystals' from the slab-like lizardite to the complex and possibly technologically useful tube structures of clinochrysotile (e.g. *Dodony and Buseck*, 2004; *Falini et al.*, 2004). The crystal shape and symmetry of major minerals in serpentinized peridotite are shown in Figure 1.1.

It is important to note that in addition to converting the ultramafic materials to the lower density and more compressible serpentine minerals (lizardite, antigorite, chrysotile),
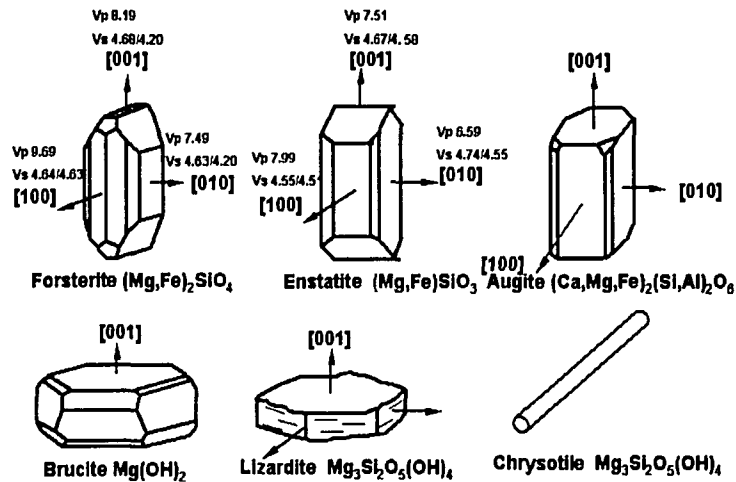
Figure 1.1: Crystal shape and symmetry of representative minerals modified from *Deer* (1992); velocity data from *Weiss et al.* (1999).

these alteration reactions also result in the production of magnetite, the mineral that is most responsible for the magnetic properties of the rock samples as will be shown in Chapter 2.

The issue of serpentine is important because while it is pervasive in the ophiolite samples studied, there remains some discussion as to what overall degree it is present in the oceanic crust itself. This bears on the validity of the simple ophiolite model described above. Opinions range from the early ideas of Hess of complete serpentinization soon after formation at mid-ocean ridges to smaller amounts due to difficulties of delivering sea-water to the depths of the peridotites (*Christensen*, 2004). Here the distinction is made between those processes in the vicinity of subducting slabs where differing processes may be at play that can result in the production of denser and faster antigorite (e.g. *Bostock et al.*, 2002; *Ranero and Sallares*, 2004; *O'Reilly et al.*, 1996) and the lower temperature hydrothermal activities that result in lizardite and clinochrysotile (e.g. *Evans*, 2004). Dredging of the seafloor along transform faults and drilling in the midocean ridge valleys yields pervasively serpentinized periodotite (e.g. *Juteau et al.*, 1990). A further

complication is that the seismic velocities of peridotites containing from about 10 % to 40 % serpentine fall within the same range of seismic velocities from 6.1 to 7.5 km/s as expected for gabbroic and doleritic lithologies; this makes discrimination between these rock types difficult on the basis of seismic observations alone (*Horen et al.*, 1996), even his measurements confirmed that P and S wave velocities linearly decrease as sepentine content increases. This contradicted Christensen's (*Christensen*, 1972) contention that the compressional and shear velocities and their ratio did not indicate pervasive serpentinization when compared to observed seismic values; on this basis Horen suggested that the serpeninization seen in ophiolites is produced during the obduction of the oceanic plate, and seismic velocities are compatible with the existence of partially serpentinized peridotites in slow-spreading ridge in accordance with geological observations. *Carlson and Miller* (1997) recognized that serpentine does exist but indicated by their analyses of Christensen's and Horen's data that the amount of serpentine is likely not large as the compressional versus shear wave trends of the serpentinized peridotites diverged from that of a gabbro-diabase trend that is in good agreement with the seismic refraction observations. A more likely scenario is that both views will hold in differing areas depending on a number of factors with spreading rate being an important one. Slow spreading ridges are more highly fractured and are thought to have thinner extrusive and gabbroic layers that would admit more water and allow greater degrees of serpentinization. The earlier laboratory seismic measurements on ultramafic rocks are listed in Table 1.2.

One additional point with regards to serpentinization and how it is presented in the literature needs to be mentioned. Modal analysis of serpentinized rocks can be difficult using conventional microscopic techniques; these techniques can further be in error due to the 2D nature of thin sections. A further disadvantage is that such modal analysis can be time consuming. Consequently, many authors have resorted to using the density of the rock $\rho$ as a proxy measure for the modal percentages of serpentine (*Christensen*, 1978; *Miller and Christensen*, 1997; *Oufi et al.*, 2002). These authors justify use of this measure because the density of the pure olivine and pyroxenes (near 3337 $kg/m^3$ for $Fo_{90}$ and 3285 $kg/m^3$ for $En_{90}$) are relatively close to one another and substantially exceed that for serpentine ($\sim$ 2550$kg/m^3$). *Miller and Christensen* (1997) defined an empirical formula for the degree of serpentinization S (i.e. the volume fraction of serpentine) to be Eq. 1.6:

---

17

Table 1.2: Earlier laboratory seismic measurements in ultramafic and mafic rocks

| Rock | P wave $V_{max}$ [Km/s] | P wave $V_{min}$ [Km/s] | P wave Anisotropy (%) | S wave $V_{max}$ [Km/s] | S wave $V_{min}$ [Km/s] | S wave Anisotropy (%) | P/T ($MPa/°C$) | density ($g/cm^3$) | reference |
|---|---|---|---|---|---|---|---|---|---|
| Harzbugite (Bushveld) | 7.91 | 7.7 | 2.7 | | | | 200/room | 3.37 | Birch, 1960 |
| Dunite (Webster N.C.) | 7.68 | 7.49 | 2.9 | | | | 200/room | 3.24 | Birch, 1960 |
| Dunite (Wash.) | 8.85 | 7.92 | 11.1 | | | | 200/room | 3.31 | Birch, 1960 |
| Serpentinite (Theford) | 5.88 | 5.65 | 4 | | | | 200/room | 2.6 | Birch, 1960 |
| Serpentinite (Cal.) | 6.12 | 6.05 | 1.1 | | | | 200/room | 2.71 | Birch, 1960 |
| Serpentinite (Cal.) | 5.03 | 4.56 | 9.9 | 2.35 | 2.21 | 6.1 | 200/room | 2.52 | Christensen, 1966a,b |
| Peridotite 1 (Cal.) | 6.24 | 5.77 | 7.8 | 3.04 | 2.86 | 6 | 200/room | 2.75 | Christensen, 1966a,b |
| Peridotite 6 (Cal.) | 7.25 | 7.12 | 1.8 | 4.04 | 3.92 | 3 | 200/room | 3.14 | Christensen, 1966a,b |
| Peridotite 1 (Hawaii) | 7.85 | 7.45 | 5.2 | 4.31 | 3.91 | 9.6 | 200/room | 3.29 | Christensen, 1966a,b |
| Dunite (Wash.) | 8.96 | 8.22 | 8.7 | 4.83 | 4.38 | 9.7 | 200/room | 3.33 | Christensen, 1966a,b |
| Peridotite 475 (Italy) | 8.67 | 8.12 | 6.3 | 4.75 | 4.68 | 1.3 | 600/20 | 3.32 | Kern, 1993 |
| (Italy) | 8.37 | 7.84 | 6.3 | 4.55 | 4.51 | 1.8 | 600/600 | 3.27 | Kern, 1993 |
| Serpentinite 987 | 7.92 | 6.11 | 26.4 | 3.86 | 3.19 | 18.5 | 600/20 | 2.74 | Kern, 1993 |
| (unknown) | 7.92 | 5.84 | 29.3 | 3.71 | 3.03 | 19.6 | 600/500 | 2.72 | Kern, 1993 |
| PS4 | 5.86 (ave.) | | 1 | 3.08 (ave.) | | 2 | atm./room | 2.71 | Horen et al., 1996 |
| PS1 | 6.79 (ave.) | | 2 | 3.58 (ave.) | | 4 | atm./room | 3.06 | Horen et al., 1996 |
| PF2 | 7.35 (ave.) | | 2 | 4.17 (ave.) | | 6 | atm./room | 3.2 | Horen et al., 1996 |
| PF1 | 7.76 (ave.) | | 6 | 4.35 (ave.) | | 5 | atm./room | 3.26 | Horen et al., 1996 |
| Ophiolite(Tibet) Cube $\pi$ | 6.6 | 6.3 | 4.7 | 3.5 | 3.3 | 5.9 | 600/room | 3.29 | Dewandel et al., 2003 |
| Cube $\sigma$ | 6.6 | 6.2 | 6.2 | 3.5 | 3.1 | 12 | 600/room | 3.29 | Dewandel et al., 2003 |
| (Oman ophiolite) 90VS53b | 7.08 (ave.) | | 2.7 | 4 (ave.) | | 3.25 | 200/room | 3.24 | Barruol, 1993 |
| (Ivrea gabbro) Serpentine 1 | 6.082 | 5.614 | 8.0 | 3.471 | 2.959 | 15.9 | 70/room | 2.72 | Song et al., 2004 |
| Serpentine 2 | 6.094 | 5.572 | 8.9 | 3.420 | 3.156 | 8.0 | 70/room | 2.645 | Song et al., 2004 |
| Serpentine 3 (Korean peninsula) | 6.176 | 5.639 | 9.1 | 3.424 | 3.249 | 5.2 | 70/room | 2.73 | Song et al., 2004 |

$$S = (3.30 - \rho)/0.785 \qquad (1.6)$$

where $\rho$ is given in units of $g/cm^3$ similar to what would be predicted for a harzburgite with 80 % $Fo_{90}$ and 20 % $En_{90}$. Some minor errors can be introduced by dense accessory minerals such as spinel due to their sparseness. However, dense magnetite ($\sim$ 5200 $kg/m^3$) may need to be corrected for in some cases (e.g. Oufi et al., 2002). As such, one needs to keep in mind the conditions under which this formula applies carefully and recognize that it should not be a complete replacement for a proper modal analysis.

18

### 1.2.5 Serpentinization and seismic anisotropy

Aside from the studies by Christensen and co-workers described above, there has been surprisingly little detailed work on ophiolite velocities since that time aside from the limited measurements mentioned above, but there are four studies (*Kern and Tubia*, 1993; *Horen et al.*, 1996; *Dewandel et al.*, 2003; *Song et al.*, 2004) that need to be mentioned as these look more specifically at the effects of serpentinization and anisotropy in ultramafic rocks.

First, it is important to reiterate that *Christensen* (1966b, 2004) noted that the greater the alteration of peridotite to serpentine, the lower the velocity from about 8.3 km/s to 5.0 km/s from unaltered to nearly completely altered, respectively. However, aside from looking at the laboratory anisotropy in his samples, he mostly tried to eliminate the effects of serpentine on anisotropy by calculating anisotropy from crystallographic orientation statistics.

*Kern and Tubia* (1993) measured P and S-wave anisotropy on cubes of serpentinized ultramafic rocks from the Sierra Alpujata massive, Spain. The measurements in three-cubes, the sides of which were oriented with respect to the rock lineation and foliation, and carried out to confining pressures of 600 MPa and $600^oC$. Although they worked with only a limited numbers of samples, they detected Christensen's inverse relationship between density and velocity. However, they further noted that the lower the density (i.e. the greater the serpentinization) the lower the anisotropy from 6-8 % in the less altered lherzolite to only < 2% in the more altered rocks.

*Horen et al.* (1996) measured P- and S-wave anisotropy on a suite of serpentinized peridotites with harzburgitic composition from the Xigaze ophiolite, Tibet. Measurements were made on rectangular prisms oriented with respect to the field lineation and foliation elements. The serpentine content in these samples fell in the range from 6 % to 70 % as estimated from the density. They found both velocity and anisotropy to decline in proportion to the degree of serpentinization. One criticism of this study, however, is that they carried out their measurements at room pressure where microcrack porosity is expected to be influential. They justified this by noting that few cracks were seen in microscopic examinations.

*Dewandel et al.* (2003) made petrographic and high pressure velocity measurements on 2 samples from the Oman ophiolite mentioned earlier. These authors observed a penetrative network of serpentine (lizardite) filled cracks oriented subparallel to the harzburgite foliation. These authors suggested, however, on the basis of petrographic examination that locations of the serpentine within the penetrative network of the rock increased the anisotropy of the rock in contrast to both observations' (*Kern and Tubia*, 1993; *Horen et al.*, 1996).

More recently, *Song et al.* (2004) carried out anisotropy measurements on three serpentinites in directions along and perpendicular to the foliation planes. Their study focussed more on determining the elastic properties of the material for engineering purposes and they did not look at issues related to density and anisotropy in the geological context. They did not provide any indication of the provenance of the material, however, aside from the fact that it was taken from an asbestos mining area. As such, comparison of these observations to this and other work that has focussed on ophilitic material is problematic. However, their results have been included for purposes of comparison in Table 1.2 and in later synoptic plots of density verse physical properties.

As will be seen, the results of this study will support the observations of the inverse relationship between serpentinization and both velocity and anisotropy.

## 1.3 Causes of magnetic anisotropy

### 1.3.1 Basics of rock magnetism

As a brief review, it is worthwhile to discuss some basic information on magnetism and on the magnetic properties of minerals. This is a large topic and for more details a good starting point is *Lowrie* (1997). Essentially, however, any moving charge generates a magnetic field. Consequently, at the atomic level both electron orbital and spin produce a magnetic effect and all materials must have magnetic properties of one kind or another above absolute zero. When a magnetic field is applied to materials, the spin of the electron produces a magnetization in a direction opposite to the applied field. In general, all materials are magnetic, however some materials are more magnetic than others. The main reason for the difference is the strength of the interaction of atomic magnetic mo-

20

ments of the material. The overall magnetic properties depend on how all these 'magnetic moments' superpose with one another, this is termed magnetization. These effects at the macroscopic scale primarily are manifested at how the material will behave when it is placed in an external magnetic field H and three major divisions can be made:

- Paramagnetic materials in which the magnetic field is slightly increased (usually only a small fraction of a percent) by their presence. The outermost electron shells of such materials are usually not filled and as such when placed in the external magnetic field the electron spins precess with a magnetic moment aligned with the field to supplant it. Most rock forming minerals fall in this category including olivine, pyroxene, and clays.

- Diamagnetic compounds in which the magnetic field is slightly decreased, again by only a small fraction of a percentage. In these materials the outermost electron shells are completed and as such will precess such that their magnetic moment is aligned against the applied field and as such decreases it. Some common rock forming minerals such as quartz, calcite, and halite are all diamagnetic.

- Ferromagnetic materials are those which we commonly think of as being 'magnetic'. In these materials the electron spins all align spontaneously without an external magnetic field. When they are in a magnetic field the strength can be increased by more than 100 %. In true ferromagnetic materials, unpaired spins in the 3d shells are linked and this behaviour is superimposed on the weak paramagnetism of the material. If the ability to link the spins is impaired by, for example, heating above a characteristic temperature then the material becomes paramagnetic again. Iron, cobalt, and nickel are true ferromagnetics. A weaker but similar coupling exists in ferrimagnetic materials including magnetite and ilmenite. In many respects these are the most important for geological study because they have a strong magnetization relative to the other rock forming minerals and even a small percentage of them will dominate the rock's magnetism.

Figure 1.2 schematically shows the atomic scale models of these different types of magnetism. The small arrows inside the frames represent the magnetic moment in the
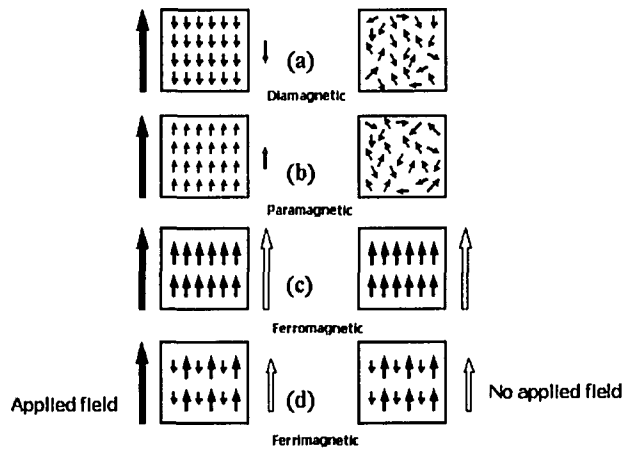
Figure 1.2: Different forms of magnetization (Modified from Tarling and Hrouda, 1993). Solid arrow: Applied magnetic field; Hollow arrow: Magnetization

material. The solid arrows outside the frame represent for the applied field; the hollow arrows for the magnetization.

It is important to put these thoughts into a quantitative form. The strength of magnetization is usually given in terms of the dimensionless magnetic susceptibility K in which the induced magnetic field B is given by (1.7):

$$B = \mu_0(1 + K)H \tag{1.7}$$

where $\mu_0$ is the permeability of free space. For rock forming minerals, the susceptibility K is typically less than $10^{-4}$ for paramagnetic, greater than $10^{-5}$ for diamagnetic, and from 0.5 to 20 for ferrites. *Hrouda* (1982) give a good overview of the issues related to defining the susceptibility. As both M and H are expressed in amperes per meter, the volumetric magnetic susceptibility, K, is dimensionless (SI). Susceptibility varies in the general case according to the strength of the field 'H' and temperature, and may also vary with the measurement direction resulting in a non-parallelism between H and magnetization $M = K \times H$ vectors.

22

There are some 'rules of thumb' with expectations of the relationship between mineralogy and how it influences the overall susceptibility of the material (*Tarling and Hrouda*, 1993):

- Case1: If K greater than $5 \times 10^{-3}$ (SI) and if the modes of paramagnetic minerals of at least 10 %, then the ferrimagnetic minerals are the prime carrier of magnetism.

- Case2: If K less than $5 \times 10^{-4}$ (SI)and has at least 10 % paramagnetic minerals, then this portion controls the magnetism.

- Case3: If K in the range of $5 \times 10^{-4}$ to $5 \times 10^{-3}$ (SI), then both ferrimagnetic and paramagnetic minerals will influence the magnetism.

The magnetic material is actually composed of small regions called magnetic domains. The existence of domains is suggested by the observation that some magnetic properties, in particular, coercivity and remanence vary greatly with grain size. Domains are small ($\sim 10^{-6}- \sim 10^{-4}m$), but are much larger than atomic distances ($\sim 10^{-10}m$). Each domain is separated from its neighbor by a block wall. In each domain the local magnetization may be saturated but not necessarily parallel to others. Without an external applied field, the domains arrange themselves to minimize the magnetostatic energy associated with their surface poles. The magnetic behavior of a single domain-sized particle is significantly different from that of one containing multidomain-sized particles, even if the composition and total quantity of the ferromagnetic materials are the same.

The magnetic behavior can be subdivided on the basis of grain size into four ranges: superparamagnetic (SPM), single domain (SD), pseudo-single domain (PSD), and multidomain (MD) (*Dunlop and Özdemir*, 1997).

If the grain is small, the magnetization within it is uniform in direction and is aligned with specific crystallographic axes. In large grains with many domains, magnetization may be aligned along an 'easy' axes (*Tarling and Hrouda*, 1993).

### 1.3.2 Magnetic anisotropy

In reality, the simple equation above is incomplete because it turns out that the value of the susceptibility measured will depend on the direction at which it is measured.
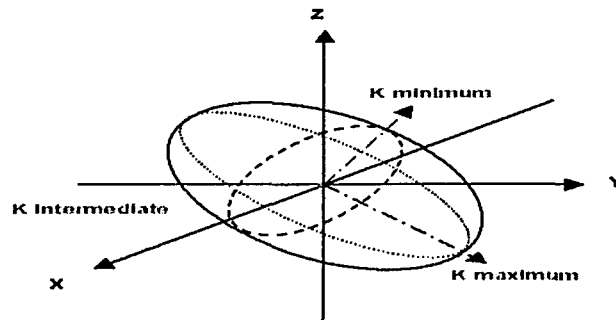
Figure 1.3: Schematic showing the magnetic susceptibility ellipsoid of rocks. (K min, K int, and K max correspond to the minimum, intermediate, and maximum principal axes of the ellipsoid)

The directional variability in magnetization is termed magnetic anisotropy. The magnetic anisotropy of rocks was first revealed by *Ising* (1942). Magnetic anisotropy can also be expressed in terms of the directional variability in the energy of magnetization to saturation (*Stacey*, 1960). As such, describing the magnetic anisotropy is more involved and while the mathematics of this is delayed till Chapter 4, it is worthwhile noting that 6 independent values are required to describe the susceptibility completely. One way to look at this is that three of these are required to describe the magnitudes of the susceptibility while those remaining are necessary to describe its directions. As such, one may use tensor notation identical to that employed in describing stress and strain. In the study of rock fabrics, low field magnetic susceptibility anisotropy may be described using an oriented ellipsoid ($K_{max}$, $K_{int}$, and $K_{min}$ or $K_1$, $K_2$, and $K_3$) (Figure 1.3). Workers commonly use a number of approaches to condense the tensor information, *Tarling and Hrouda* (1993) give an extensive overview of all of the methods used. Currently, workers mostly employ the attributes of anisotropy degree, foliation, lineation, and magnetic shape parameter, the details of these measures are delayed to Chapter 4.

24

The intrinsic susceptibility anisotropy of individual minerals will be an important consideration and measurements are even reported as early as 1907 on calcite by Voigt and Kinoshita (*Nye*, 1957). However, there still remain only a limited number of measurements of such properties. *Borradaile et al.* (1987) made measurements on small mineral separates taken from metamorophic rocks and found the magnetic anisotropy degree ($K_{max}/K_{min}$) less than 1.2. More recently, *Martin-Hernandez and Hirt* (2003) measured the magnetic anisotropy of muscovite, chlorite, and biotite, they found anisotropy degrees of about 1.3 for biotite and near 1.15 for both muscovite and chlorite. Although these measurements are useful, there still remains much work to be done (*Tarling and Hrouda*, 1993).

### 1.3.3 Magnetic anisotropy and rock texture

As noted above, a textured rock will be anisotropic partly because of the preferential alignment of the anisotropic minerals of which the rock is composed. Similarly, the magnetic anisotropy of the mineral grains of the same rock will also contribute to an overall magnetic anisotropy to the rock. Conversely, knowledge of the rock's magnetic anisotropy and its direction provides petrofabric information. This information can supplant or complement that obtained by other techniques used to obtain this information such as x-ray goniometry or universal stage petrography. The advantage of the magnetic techniques is that they are often far less time consuming and costly. The technique has mostly been applied by structural geologists who want to obtain additional information on the strain that a rock has experienced. Newer methods can even separate the effects of the ferromagnetic and the paramagnetic minerals, each of which tells a different story about the rock's history (*Kelso et al.*, 2002).

The magnetic anisotropy has been successfully used in this field of study over last few decades (*Girdler*, 1961; *Jelinek*, 1978; *Hrouda*, 1982; *Rochette et al.*, 1992; *Borradaile and Henry*, 1997; *Borradaile*, 1991, 2001). The study of magnetic anisotropy is one of the more promising subjects in rock magnetism research because it is linked to the rock's intrinsic petrofabric. In general, magnetic fabrics are sensitive indicators of rock texture and strain. Magnetic fabric techniques use this characteristic to measure the petrofabric of rocks in order to provide additional information on the rock's origin and structural evolution.

Many authors have reviewed the principles and applications related to anisotropy

of low field magnetic susceptibility (*Hrouda*, 1982; *Borradaile*, 1988; *Jackson*, 1991; *Tarling and Hrouda*, 1993; *Borradaile and Henry*, 1997). The idea that the anisotropy of magnetic susceptibility (AMS) can be used as a gauge of petrofabric is similar to that for elastic anisotropy, in that rocks will have a magnetic fabric due to the preferential orientation of anisotropic magnetic minerals. The preferred orientation of their crystallographic axes and the grain shape determine the magnitude and direction of the AMS. The bulk magnetic susceptibility and its anisotropy represent a summation of the susceptibility of all the mineral species present in a sample. This is similar to the relationships between the elastic properties and texture mentioned above, but progress in relating magnetic properties to texture is not at as advanced a stage.

### 1.3.4 Serpentinization and magnetic anisotropy

Much of the work has focused on metamorphic terranes, but there are a number of studies that focus on the magnetic anisotropy of peridotites and this has accelerated in the last few years. *Toft et al.* (1990) carried out on numerous magnetic susceptibility measurements on a suite of serpentinized harburgites from the Josephine peridotite (Oregon). In the 39 samples studied densities ranged from 2400 $kg/m^3$ to 3250 $kg/m^3$ and susceptibility varied from 0.0009 to 0.0665 (SI unit). *Oufi et al.* (2002) measured a variety of magnetic properties, including susceptibility, on nearly 300 samples of serpentinized peridotites taken from various oceanic scientific drilling programs. Both groups did not measure magnetic anisotropy, but they did demonstrate an inverse logarithmic correlation between magnetic susceptibility and density. This relationship is crudely expected because, as noted above, magnetite is a product of the retrograde serpentinization reactions. Indeed, one would expect small values of susceptibility in a completely fresh and unaltered peridotite that would not be expected to host ferromagnetic minerals.

*Hrouda et al.* (1988) showed that the paramagnetic and ferromagnetic AMS are coaxial in different types of rocks including metamorphic and that AMS is determined first of all by tectonometamorphic control factor (for both paramagnetic and ferromagnetic minerals). The magnetic patterns are very similar in metamorphic, granitoid and sedimentary rock from the Čierna hora and Branisko Mountain (West Carpathians). The reason is that the deformation of these rocks took place at the same time. *MacDonald*

*and Ellwood* (1988) contributed the AMS fabric to both mylonitic foliation and the abundant secondary magnetite from serpentinization. They considered that the later stage serpentization produced more magnetite and therefore the AMS demonstrates the influence of the serpentization that was developed along the fractures. *Bina and Henry* (1990) analyzed 16 samples of from ODP Hole 670A. They concluded that magnetic anisotropy should be likely to be mimetic of high-temperature deformation before serpentization; when serpentinization is high, the magnetic fabric correspond to some superimposition of 'olivine mimetic' and 'magnetite veins' fabrics. *Borradaile and Lagroix* (2001) used magnetic fabrics to constrain upper mantle flows in the Troodos ophiolite complex, Cyprus. They were able to show that the silicate mineral alignments are consistent with flows away from a spreading center. The magnetic component, however, shows the magnetite to have a different alignment that was likely superimposed by nearby magma chambers. In a follow up study, *Borradaile and Gauthier* (2003) looked at magnetic anisotropy in the dike sections of this ophiolite. *Lawrence et al.* (2002) used the magnetic anisotropy of serpentinized peridotites from ocean drilling cores from the slowly spreading mid-Atlantic ridge to place constraints on the tectonics of a median valley fault zone on the ridge, in which the magnetic foliation defined by $K_{min}$ is similar to the composite foliation. *Ferré et al.* (2004) actually showed that ferromagnetic and paramagnetic anisotropy (measured in the low and high field) are generally coaxial (if with statistical errors) that coincides with conclusion of *Hrouda et al.* (1988), but they made exactly opposite conclusion in the paper . Most recently, *Ferré et al.* (2005) studied unweathered peridotites from the Twin Sisters massif, Washington state. Despite contamination of the samples with ferrimagnetic minerals along cracks, they were able to isolate the paramagnetic response (i.e. that of aligned olivine) and compare this with lattice preferred orientations determined using electron backscattering to show that the magnetic anisotropy could be used as a proxy for the LPO.

## 1.4 Objective of the work

Determination of the lithological, magnetic and seismic properties of crustal and mantle rocks is essential for proper interpretation of the nature of observed seismic reflectors or

of velocity studies, and of magnetic phenomena. Various authors have investigated and focused their research on the relationship between mineralogical and magnetic fabrics, or mineralogy and seismic anisotropy. Despite the ubiquitous characteristics of magnetic and seismic anisotropy of rocks, few studies have examined the relationship, if any, between seismic and magnetic anisotropy despite numerous observations that magnetic petrofabric is closely related to both micro-crack and lattice-preferred orientation (LPO). Thus, the primary and exploratory focus of this work is to determine if there is a relationship between magnetic anisotropy and seismic anisotropy in the Pindos and the Vourinos ophiolites. Some of the observations may be of general interest to those who study the seismological and magnetic aspects of serpentinized peridotites.

This will be accomplished by laboratory analysis of velocity anisotropy and AMS in both the Rock Physics and Magnetic laboratories and comparing the results. It is reasonable to suggest that the LPO and assembly of minerals may influence the magnetic fabrics and the AMS in a manner similar to seismic anisotropy. Hence, the second motivation for this study is to assess the extent to which elastic and magnetic anisotropies correspond in the Pindos and the Vourinos ophiolites, such that a well established correlation of the degree and direction of anisotropy would allow the simple AMS measurement to be used as a proxy for rock fabrics in seismic anisotropy studies. In later work, we aim to determine other systematic magnetic fabric changes in various anisotropic media and construct a database of experimental data for numerical modeling. Metamorphic rocks with complex texture and composition usually exhibit a particularly seismic and magnetic anisotropy. With a suite of rocks of the same origin, and extending over a wide range of degree of serpentinization, our investigation may yield interesting comparisons. The approach used in this study to derive anisotropic rock properties comprises of two complementary methods applied to the same samples: (1) ultrasonic velocity laboratory measurements and, (2) anisotropy of magnetic susceptibility laboratory measurements. Both procedures and results will be described, compared and discussed for a group of serpertinized dunite and harzburgite samples from the Pindos and the Vourinos ophiolite in Greece.

28

# Chapter 2

# Geology and Characteristics of the Samples

This chapter contains a brief review of the geologic concepts regarding the Tethyan Hellenic ophiolites and the Pindos and Vourinos ophiolites in particular. This sets the stage for the description of the samples. A number of tools were employed in order to better characterize the samples including petrographic analysis, x-ray diffraction, x-ray fluorescence, grain density, porosity, scanning electron microscopy, magnetization as a function of temperature in the thermomagnetic analysis, and isothermal remanent magnetization (IRM) experiment. The results of these studies are presented in this chapter.

## 2.1  Tethyan ophiolites

As noted in Chapter 1, ophiolites are considered to be masses of oceanic crust and upper mantle rocks, where there is a distinctive sequence of magmatic, sedimentary, and metamorphic rocks formed in an oceanic environment (*Best*, 2003). Much of the standard ophiolite model described in the previous chapter was developed in the early days of plate tectonics and assumed, for the most part, that all the ophiolites were formed at mid-ocean ridges (mid-ocean ridge basalt or MORB). This has been shown more recently to not describe all ophiolites; and the geochemical signature of many is more akin to that of island arc tholeiite (IAT). This oceanic crust is not formed at the mid-ocean ridges but at back-arc basin extensional regimes. The 'oceanic crust' need not have been produced only at mid-ocean ridges but evidence in the last 20 years has tended to show that many,

29

if not most, of the crust that would form ophiolites came from upwelling and magmatism associated with lithosphetic extension in the upper plate that formed arc related oceanic crust (e.g. see reviews by *Dilek* (2003)and *Robertson* (2004) which are referred to as 'supra-subduction zone (SSZ) environments by those workers specializing in ophiolite studies. The crust making many ophiolites then formed in the last stages of the Wilson cycle as an oceanic basin closes. As such, the term ophiolite should not be taken to indicate the specific tectonic setting in which the crust was formed as it could refer to structures formed either at mid-ocean or within back arc basins.

The ophiolite rocks studied here were taken from two of the Dinardic-Hellenic ophiolites, which themselves are part of the larger family of Tethyan ophiolites related to the closure of various Tethyan basins and that stretch from Indonesia to Spain. The story behind these differing ophiolites and their tectonic significance is highly complex and still incomplete and even controversial (*Flower and Dilek*, 2003). For example, even within the Balkan Pennisula two differing generations of Jurassic ophiolite belts may be found: the western Pindos and the eastern Vardar zones that are likely respectively related to closure of the 'Paleo-Tethys' and the 'Neo-Tethys' ocean basins (*Stampfi and Borel*, 2004). However, it must be reiterated that the focus of this thesis is not on the tectonic significance of these particular rocks but on the development of techniques for determining their physical properties. As such, the interested reader is directed to the papers just mentioned and that of *Dilek et al.* (2005) for good overviews of current thought on this topic.

In this study, a suite of samples with varying degrees of serpentinization from the Pindos and the Vourinos ophiolites (Greece) were provided to the University of Alberta in order to assist with material characterization for deformation measurements. The Pindos and Vourinos ophiolites are part of the Dinaric-Hellenic ophiolite belt out-cropping along the Northeastern Mediterranean (Figure 2.1(a)). They are relatively close to one another (40 km) and fall within the Pindos belt mentioned above (*Dilek et al.*, 2005). These ophiolites formed during the Middle Jurassic (*Smith*, 1993) and were emplaced shortly after their formation (*Rassios*, 2000). The Vourinos ophiolites are composed primarily of harzburgite and associated dunite, which are locally deformed. The Vourinos ophiolite shows the most complete stratigraphy (12 km in thickness, with 5 km of crust), including peridotite, gabbro, and a well-developed dykes section . The Pindos ophiolite is less

30

compete and more tectonized, with a basal layer of harzburgite mylonites (200 m), and less deformed harzburgite and dunite bodies above it, and small outcrops of dyke and basalt (*Rassios et al.*, 1983). Figure 2.1(a) shows the locations of the selected ophiolites from the Hellenic Arc in Greece and Albania (green areas). Figure 2.1(b) is the map of the Pindos and Vourinos ophiolites (*Rassios*, 2000). The Vourinos ophiolite shows a continuous stratigraphy, while tectonism is more prominent in the Pindos ophiolite, where contacts are mostly tectonics (thrust faults). The Meso-Hellenic Trough developed in the Cenozoic has separated these ophiolites. *Ross et al.* (1980) and *Ross and Zimmerman* (1996) carried out comparative conventional structural analysis combined with paleopiezometry and paleothermometry on the Pindos and the Vourinos ophiolites that indicate while they are primarily similar, it appears there were some differences in their emplacement history.

As the brief overview above indicates, the geologic study of these ophiolites is both interesting and complex, and as such remains incomplete even as admitted by the authors above. However, it must be remembered that the purposes of this study were not to add new information to the understanding of these ophiolites, per se, but to look at the development of complementary techniques for physical property determination. As such, the rock samples were selected not on the basis of their geological significance in the context of these ophiolites but because they all were serpentinized olivine rich peridotites. The rock blocks used in this study were selected from samples obtained during a fieldwork season in 2000 by Escartín and Mével. Dr. Escartín will use the samples in later deformation experiments. As such, he hoped to keep the material studied as simple as possible in order to be able to minimize the number of interactions between various minerals that could occur during his high pressure and temperature deformation studies; olivine rich serpentinized periodites were thus chosen. Location of sampling sites are indicated by black dots and corresponding labels.
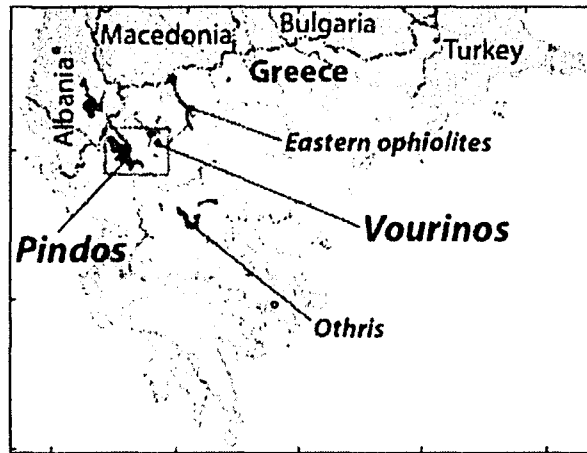
(a)
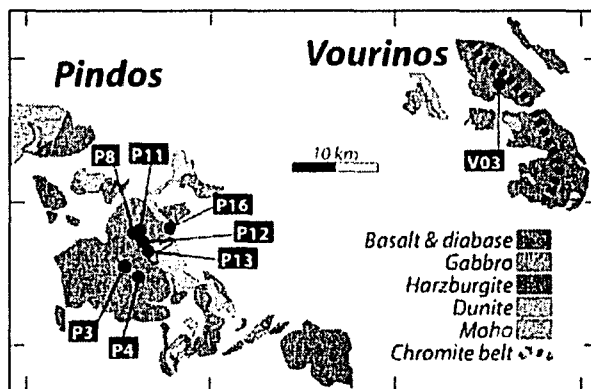


(b)

Figure 2.1: Top: Sample location map in Greece. Bottom: Lithological distribution map of Pindos and Vourinos ophiolites (after Rassios et al., 2000; by courtesy of J.Escartin).

32

Table 2.1: The minerals identified in X-ray diffraction analysis

| Sample | Density $(g/cm^3)$ | Major minerals identified by X-ray diffraction |
|---|---|---|
| P03-1 | 3.19 | Forsterite, Enstatite, Clinochrysotile |
| P04-2 | 2.87 | Forsterite, Enstatite, Clinochrysotile |
| P08-3 | 3.06 | Forsterite, Enstatite, Clinochrysotile |
| P11-1 | 3.28 | Forsterite, Enstatite, Clinochrysotile |
| P12-1 | 3.25 | Forsterite, Enstatite, lizardite |
| P13-1 | 2.6 | Clinochrysotile, Forsterite, Brucite, Lizardite |
| P13-2 | 2.6 | Clinochrysotile, Forsterite, Brucite, Lizardite |
| P16-3 | 2.82 | Clinochrysotile, Forsterite, Lizardite, Augite |
| P 08-4 | 3.08 | Forsterite, Enstatite, Clinochrysotile |
| V 03-7 | 2.95 | Forsterite, Brucite, Clinochrysotile |
| V 03-11 | 2.99 | Forsterite, Brucite, Lizardite |

## 2.2 Physical characteristics

### 2.2.1 X-ray diffraction

Due to complications of serpentinized ophiolite, X-ray diffraction (XRD) is used to analyze the mineralogic composition. The mineralogic composition both from XRD power and from oriented samples show the similar composition including the presence of the same major minerals: Forsterite, Enstatite, Clinochrysotile, Lizardite, and Brucite. All major compositional minerals are listed in Table 2.1. As noted, no magnetite was detected in the XRD experiments, which means that there must be only small amounts.

### 2.2.2 Optical petrographic studies

Rock fabric may have some different features in their body, e.g. foliation and lineation. Foliation is a planar fabric produced during the deformation or crystal growth. The foliation used for planar fabrics depends on the grain size and the gross appearance. The lineation is a linear orientation of elongate crystals. The long directions of the crystals being parallel to each other generates the alignment. When each uncut specimen dimension allowed, one core was cut perpendicular to the foliation plane and at least one other sample was cut parallel to the foliation plane. In cases where there is a visible lineation direction, two cores parallel and perpendicular to the lineation direction were cut within the foliation plane. If possible, additional cores were cut in the same direction to investi-

33

gate the heterogeneity within a given specimen.

Thin sections identified the macrostructure of the samples. Photomicrography from the thin sections cut perpendicular and parallel to the foliation illustrating the microstructure are shown in Figure A.1 to A.11 in the Appendix A. Comparison of typical textures of high, intermediate, and low serpentinization samples are shown in Figure 2.2, with different serpentine minerals range from 40.2 %, 23.5 %, and 8.3 % (based on whole rock analysis discussed in next section). Different serpentinization degrees will change the rock texture and composition, then greatly influence both seismic and magnetic properties of the rock samples. O'Hanley (1996) discusses details of the complex textures observed in serpentinized peridotites. He notes the difficulties in identifying these minerals and noting that 'microbeam X-ray' techniques may be necessary to study the small serpentine mineral grains. For example, two typical serpentinized peridotite samples P 03-1 and P13-1 are seen in Figure 2.2(c) and 2.2(a); P 13-1 is heavily serpentinized and P 03-1 is lightly serpentinized. Olivine grains have a high birefringence, usually appearing with bright greenish-blue to red in the thin section, and have a lack of cleavage. Elongate crystals display parrel extinction. Serpentine is colorless to pale green. Chrysotile is usually fibrous; lizardite is platy; both have the perfect cleavage. The thin sections display serpentine's straight extinction. Pyroxene grains are pale yellow and display good cleavage, and parallel extinction in the Figure 2.2(b). Comparing P 03-1 and P 13-1 in Table 3.10 and Table 4.2, laboratory data show a large decrease in velocity and anisotropy; meanwhile, a obvious increase in magnetic susceptibility with increasing serpentinization degree. However, in the thin section the textures of these two differ significantly. The highly serpentinized P 13-1 has a chaotic appearance with few remaining clear crystals of olivine. The darker portions of the image are predominantly serpentine that appears in what has been referred to as 'apparent' fabrics by O'Hanley (1996).

The major minerals in the samples include forsterite from the olivine group, serpentine group minerals, enstatite and augite from the pyroxene group, and brucite. A few other minerals including dolomite, clinochlore, talc, and tremolite. Given the difficulty in differentiating the serpentine group minerals from each other on the basis of X-ray analysis, and although the program used to analyze the X-ray results assigned the name clinochrysotile, we prefer to use serpentine group. Modal analysis were from the thin

34

Table 2.2: Whole rock analysis of samples (composition of oxides listed in weight percentage)

| Sample Ident | $SiO_2$ | $Al_2O_3$ | $CaO$ | $MgO$ | $Na_2O$ | $K_2O$ | $Fe_2O_3$ | $MnO$ | $TiO_2$ | $P_2O_5$ | $Cr_2O_3$ | LOI | Sum |
|---|---|---|---|---|---|---|---|---|---|---|---|---|---|
| Weight percentage | % | % | % | % | % | % | % | % | % | % | % | % | % |
| P03-1 | 40.96 | 0.25 | 0.31 | 46.31 | < 0.01 | 0.03 | 9.15 | 0.12 | 0.05 | < 0.01 | 0.53 | 2.5 | 100.1 |
| P04-2 | - | - | - | - | - | - | - | - | - | - | - | - | - |
| P08-3 | 41.83 | 0.53 | 0.47 | 45 | < 0.01 | 0.03 | 8.72 | 0.12 | 0.06 | < 0.01 | 0.43 | 3.1 | 100.2 |
| P08-4 | 41.73 | 0.3 | 0.5 | 45.7 | < 0.01 | 0.03 | 8.45 | 0.12 | 0.02 | < 0.01 | 0.43 | 3.05 | 100.2 |
| P11-1 | 42.96 | 0.34 | 0.5 | 46.46 | < 0.01 | 0.04 | 8.81 | 0.12 | 0.04 | < 0.01 | 0.47 | 0.5 | 100.2 |
| P12-1 | 42.73 | 0.07 | 0.21 | 47.41 | < 0.01 | 0.02 | 8.54 | 0.12 | 0.02 | < 0.01 | 0.5 | 0.65 | 100.2 |
| P13-1 | 34 | 0.01 | 0.16 | 44.33 | < 0.01 | 0.03 | 7.38 | 0.1 | 0.03 | < 0.01 | 0.32 | 13.85 | 100.1 |
| P13-2 | 33.93 | 0.05 | 0.14 | 44.41 | < 0.01 | 0.03 | 7.29 | 0.1 | 0.02 | < 0.01 | 0.47 | 13.95 | 100.3 |
| P16-3 | 40.76 | 2.8 | 1.92 | 36.41 | < 0.01 | 0.04 | 9.41 | 0.14 | 0.1 | < 0.01 | 0.36 | 8.6 | 100.6 |
| V03-7 | 37.57 | 0.21 | 0.25 | 47.55 | < 0.01 | 0.03 | 8.2 | 0.11 | 0.01 | < 0.01 | 0.5 | 5.95 | 100.3 |
| V03-11 | 37.9 | 0.05 | 0.17 | 49.11 | < 0.01 | 0.03 | 7.53 | 0.1 | < 0.01 | < 0.01 | 0.43 | 5.1 | 100.3 |

section were attempted. However, there were a number of difficulties with adequately distinguishing minerals from one another given the complex serpentine textures, and this attempt was dropped. More involved analysis using microprobe measurements may be needed to adequately carry out modal analysis.

### 2.2.3 Whole Oxide and Chemical-modal analysis

X-ray fluoresecence (XRF) is a quantitative elemental analysis technique for the determination of the chemical composition of many types of materials, based on their characteristic X-ray emission behavior. The XRF results from SGS Geochemical Services in Toronto are listed in Table 2.2. There is no XRF analysis for the sample P 04-2.

The analysis can be separated by three steps. At first, the major minerals present in the samples can be determined based on the powder X-ray diffraction (XRD). Then, convert the results from the whole rock analysis to molar concentrations from oxide weight concentrations. Finally, according to the molar concentrations of the minerals, we invert these to find the approximate estimation of the relative molar concentrations of the minerals and then convert to weight percentage. The results shows that olivine is major component in all samples in Table 2.3.

### 2.2.4 Physical characteristics

Mass densities were obtained by the Archimedean displacement method and by using He porosimetry on these dried samples. The porosities of the samples were obtained by

(a)
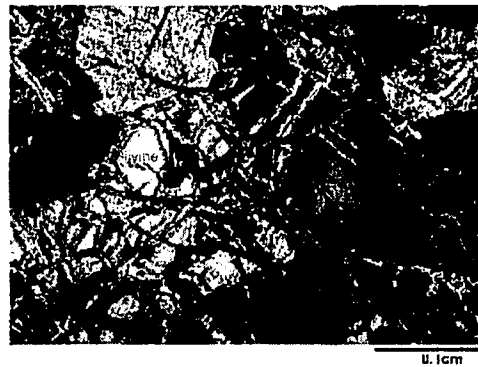


(b)
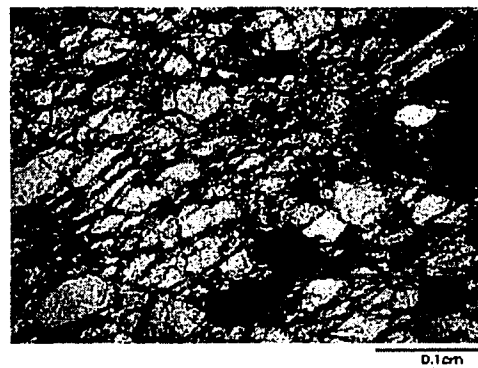


(c)

Figure 2.2: Representative samples of textures including: a. large serpentinization degree (P13-1) b. intermediate serpentinization degree (P16-3) c. small serpentinization degree (P03-1). Thin section were taken under crossed polars.

36

Table 2.3: The relative concentration of the minerals as determined using whole rock analysis

| Minerals Weight percentage | Forsterite % | Enstatite % | Clinochrysotile % | Brucite % | Lizardite % | Augite % |
|---|---|---|---|---|---|---|
| P03-1 | 85.1 | 6.6 | 8.3 | - | - | - |
| P08-3 | 77.0 | 13.0 | 9.5 | - | - | - |
| P08-4 | 77.1 | 3.8 | 16.3 | - | - | - |
| P11-1 | 82.7 | 0.6 | 7.0 | - | - | - |
| P12-1 | 87.2 | 2.5 | - | - | 10.3 | - |
| P13-1 | 59.7 | - | 8.1 | 10.2 | 22.1 | - |
| P13-2 | 60.5 | - | 9.0 | 10.3 | 20.2 | - |
| P16-3 | 44.0 | 22.7 | - | - | 23.5 | 9.6 |
| V03-7 | 74.4 | - | 11.2 | 0.74 | - | - |
| V03-11 | 74.9 | - | - | 2.8 | 17.5 | - |

Table 2.4: The density and porosity of plugs

| Sample | Density (grain)(MultiPycnometer) $(g/cm^3)$ | Porosity (%) | Density(Archimedean) $(g/cm^3)$ |
|---|---|---|---|
| P03-1 | 3.24 | 1.5 | 3.19 |
| P04-2 | 2.91 | 2 | 2.87 |
| P08-3 | 3.09 | 0.3 | 3.06 |
| P11-1 | 3.33 | 1.2 | 3.28 |
| P12-1 | 3.29 | 1.7 | 3.25 |
| P13-1 | 2.62 | 2.4 | 2.6 |
| P13-2 | 2.63 | 0.6 | 2.6 |
| P16-3 | 2.88 | 0.6 | 2.82 |
| P 08-4 | 3.08 | - | 3.08 |
| V 03-7 | 2.96 | - | 2.95 |
| V 03-11 | 2.97 | - | 2.99 |

calculation from data generated by a He porosimeter (Quantachrome MultiPycnometer No. MPV-60 C) and envelope volume (Micromeritics GeoPyc 1360). All densities and porosity are shown in Table 2.4. The porosity is typically less than 2 % at room temperature and pressure. This contention is supported by the relatively small dependence of the sample velocities to pressure as will soon be shown. Further, no detectable permeability ($< 10^{-21} m^2$) was found in these samples by Escartín.

SEM micrography was used to investigate the microstructure and composition of the rock and minerals. The SEM micrographs here (Figure 2.3(a) and 2.3(b) ) do not reveal much about the rock texture in general, however they are consistent with the other observations of small porosity and vanishing permeability as no pores are seen at this scale.

The relationship between density and serpentine minerals percentage (clinochrysotile + lizardite) has been plotted based on the whole rock analysis in these samples. There

37
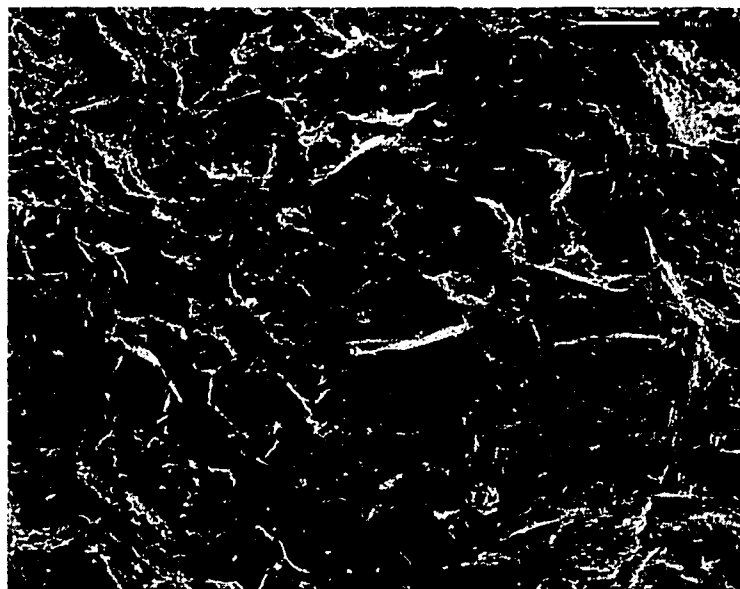
(a)
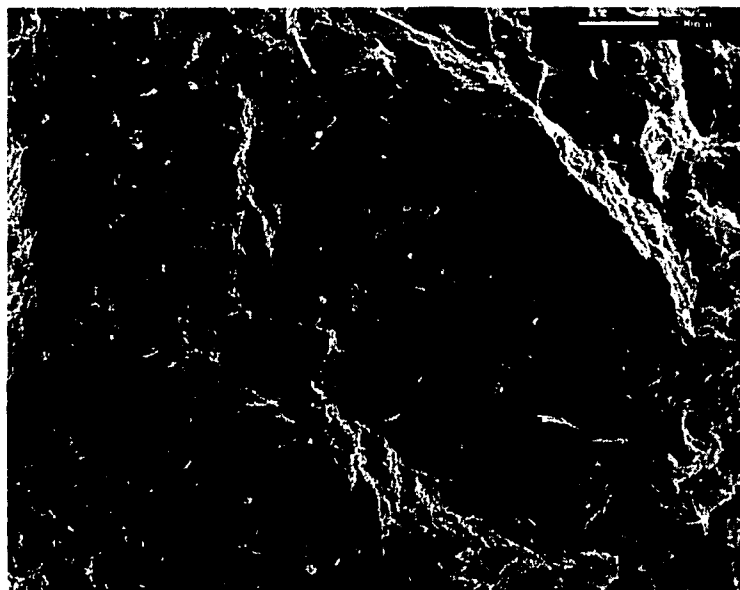


(b)

Figure 2.3: Secondary electron images. Top: SEM photography of sample P 11-1. Bottom: SEM photography of sample P 13-1.

38
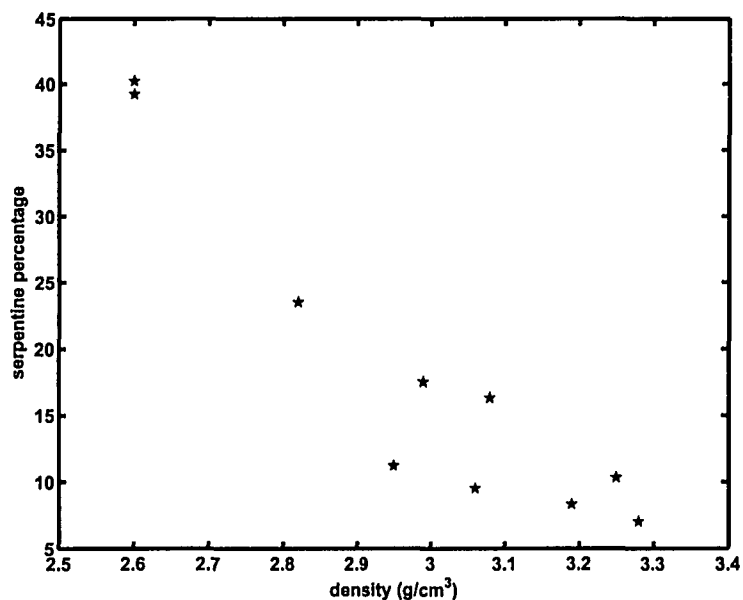
Figure 2.4: Density decrease with the increasing serpentine minerals (based on whole rock analysis).

is a obvious decrease trend with the increasing serpentine percentage in Figure 2.4 . We also plot LOI (Loss on ignition) with density (Figure 2.5). The LOI is related to the loss of volatiles. The decrease trend between these two is very clear. This is likely caused by loss of water from the serpentines and brucite.

### 2.2.5 Existence of magnetite

Magnetite is the most common ferrimagnetic mineral (*Hrouda*, 1982), and exhibits an unique Curie temperatures of 578 $^oC$. Other magnetic behaviors of magnetite, such as spontaneous magnetization, hysteresis, and remanence are similar to ferromagnetic mineral like mental iron. However, iron and magnetite have different magnetic structures. Pure iron has a different Curie temperature close to 800 $^oC$. In order to prove the presence of pure magnetite in this study, the thermomagnetic analysis and isothermal remanent magnetization (IRM) experiments have been completed. The analysis revealed a Curie temperature of 580 $^oC$ indicating the presence of pure magnetite in Figure 2.6. Additional evidence is shown in Figure 2.7, where the magnetic moment of the sample was

39
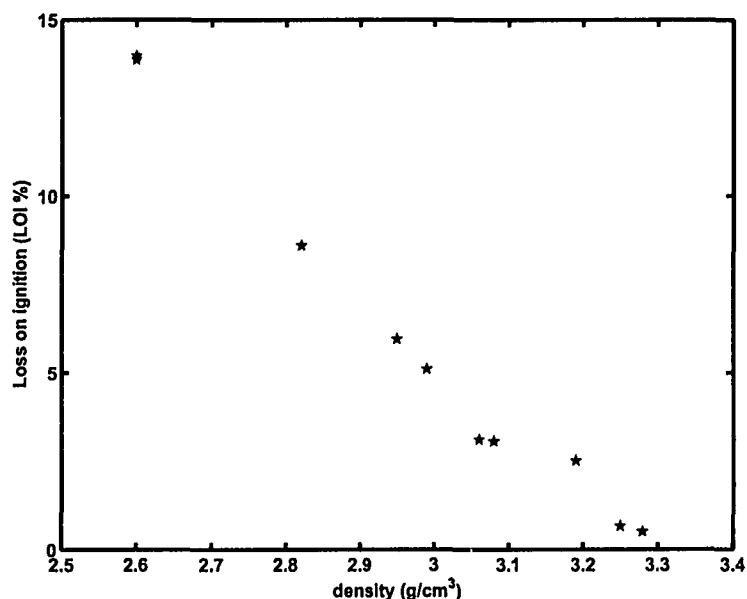
Figure 2.5: Density decrease with the increasing LOI (Loss on ignition) minerals (based on whole rock analysis).

measured during three stages: demagnetization, saturated in a progressive applied field, and finally reduced to zero and re-saturated in the backfield direction. When a very low field was applied to the sample in the opposite direction, a significant reduction in the magnetic moment indicates that ferrimagnetic minerals may exist. The fact that the IRM was saturated twice in an applied field around 300 mT suggest that the ferrimagnetic mineral is magnetite (*Dunlop and Özdemir*, 1997). The remanent acquisition coercive force ($H'_{cr}$) and the remanent coercive force ($H_{cr}$) ratio is used to exactly differentiate magnetite and titanomagnetite (*Dankers*, 1981). For instance, $H'_{cr}/H_{cr} = 1.6 \pm 0.2$ for magnetite and $H'_{cr}/H_{cr} = 1.2 \pm 0.2$ for titanomagnetite by Dankers's report. Our sample yields $H'_{cr} = 38mT$ and $H_{cr} = 23mT$ with ratio $H'_{cr}/H_{cr} = 1.65$, which means that it is magnetite by this additional evidence.

Another thermomagnetic analysis is done for the typical low serpentinization sample P 03-1 in Figure 2.8. The room temperature magnetic susceptibility is much lower (2.5 times less) than for sample P 16-3. That demonstrates that magnetite must be a very minor magnetic mineral in the samples with low serpentinization degree. The increment of

40
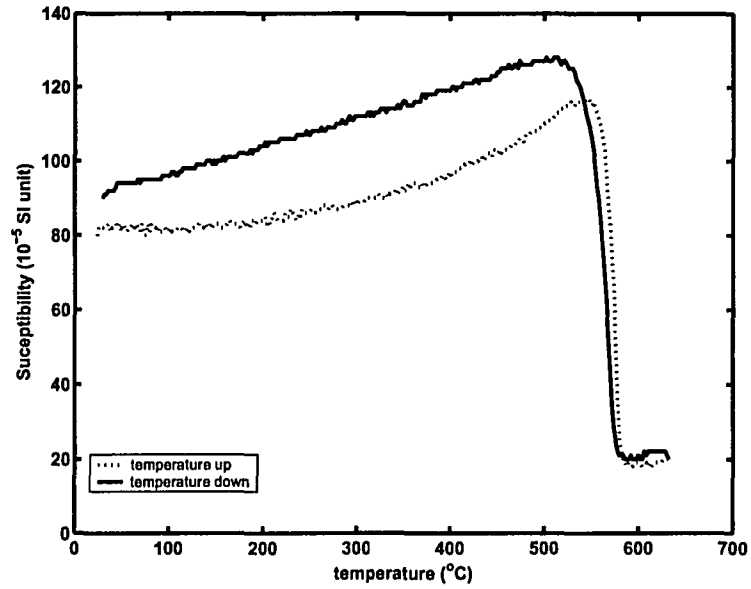
Figure 2.6: Magnetic susceptibility vs temperature for sample P 16-3
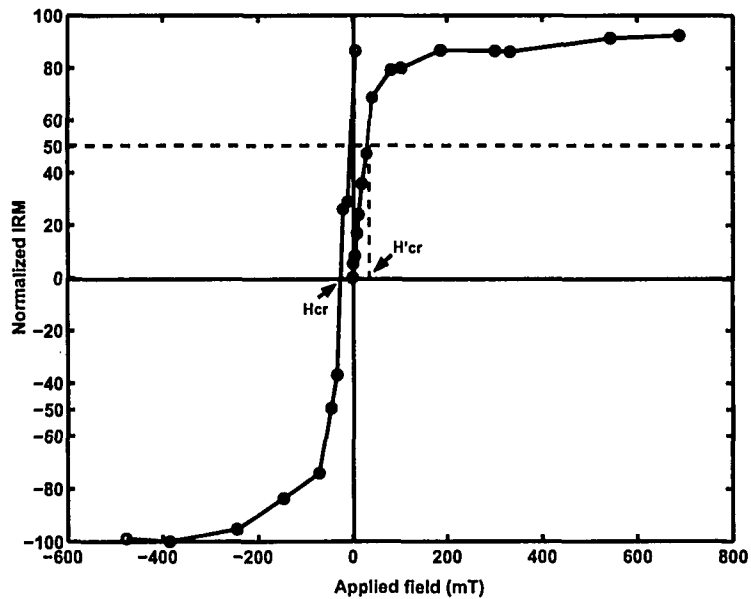


Figure 2.7: Isothermal remanent magnetization for sample P 16-3; the sample P 16-3 was first demagnetized, then, saturated in a progressively strong applied field, finally, gradually reduced to zero in the backfield direction.

41

magnetic susceptibility around 220 $^{o}C$ may indicate so-called 'lambda' transition in the heating curve when thermally activated ordering in hexagonal pyrrhotite crystal occurs. The Curie temperature of phyrrotite is about 265 $^{o}C$ (*Dunlop and Özdemir*, 1997). During heating in the air usually pyrrhotite transforms irreversibly to magnetite (*Bina and Daly*, 1994). The Figure 2.8 demonstrates this possible scenario when magnetite is demagnetized about its Curie temperature at 580 $^{o}C$. After cooling the magnetic susceptibility has higher value because of new magnetite formed in the sample. The pyrrhotite is a common accessory mineral in metamorphic rocks.

Another possible explanation of the thermomagnetic behavior of the low serpentinized samples is the presence of chromites that are common in peridotites (*Dunlop and Prévot*, 1982). Their Curie temperature depends on content of Cr. Decreasing of Cr content leads to increasing of the Curie temperature.

We cannot exclude possibility of some titanomagnetite presence although it is not very typical accessory mineral for dunites and serpentinites. Titanomagnetite inverts during metamorphic heating into a phase assemblage that includes magnetite (*Dunlop and Özdemir*, 1997) and therefore often is not presented in these rocks. During the laboratory heating experiment the titanomagnetite can transform to magnetite irreversibly. The transformation usually occur between 200 and 400 $^{o}C$ and depends on content of Ti.

Mostly, AMS can be a good linkage between magnetic fabric and rock fabric, where bulk magnetic susceptibility is usually determined by the volume of paramagnetic, diamagnetic, and ferrimagnetic minerals, with ferrimagnetic as an accessory phase in the entire rock. Usually in the normal fabric situation, the orientation of an AMS carrier mineral is the representative of major phases of minerals, or accessory ferrimagnetic phase that can mimic the orientation of the main phase in the rocks.

Since ferrimagnetic minerals have positive and large susceptibilities compared to the paramagnetic and diamagnetic minerals, ferrimagnetism plays an important role in determining magnetic fabric, even if they are only accessory phases. In magnetite, for example, the AMS is controlled dominantly by its shape anisotropy.

Most rock-forming minerals are paramagnetic (e.g. olivine, amphibole, biotite, garnet ) or diamagnetic(e.g. quartz, feldspars, calcite ). Diamagnetic minerals are weakly magnetized in the direction opposite to an applied field; and typically characterized by
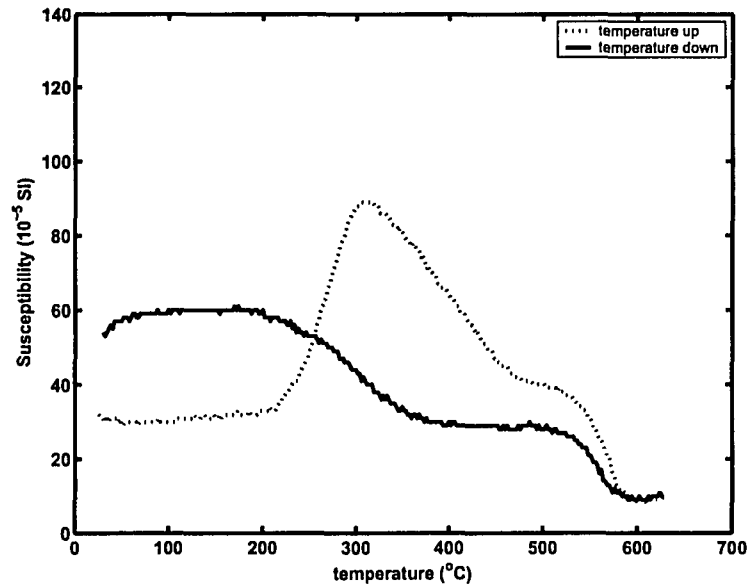
Figure 2.8: Magnetic susceptibility vs temperature for sample P 03-1

a negative and small magnetic susceptibility. Conversely, paramagnetic materials are magnetized in the same direction as the applied field, usually to a greater but still small degree. Both paramagnetism and diamagnetism disappear after removal of the applied field. Magnetic susceptibility in these minerals is also temperature dependent. In paramagnetic and diamagnetic minerals, the AMS is typically magnetocrystalline, being determined by the crystallographic lattice preferred orientation of the mineral grains (Tarling and Hrouda, 1993).

As discussed before, AMS in most rock-forming minerals is mostly due to shape anisotropy (e.g. magnetite), and / or magnetocrystalline anisotropy. Two factors determine the magnitude of the magnetic anisotropy: the anisotropy of the particles themselves and the degree of their alignment. The anisotropy of the individual particles is controlled by crystalline, stress, and shape anisotropy. It must be emphasized here again that no one method of measurement is capable of resolving the contributions of shape anisotropy and magnetocrystalline anisotropy to AMS. Furthermore, the magnitude of shape anisotropy of a ferrimagnetic grain can differ radically depending on whether the contributor is multi-domain or single-domain. Additionally, a potentially significant fac-

tor is the effect of magnetic particle distribution on anisotropy; non-uniform distribution of interacting ferrimagnetic grains may also result in the magnetic anisotropy(*Hargraves et al.*, 1991; *Stephenson*, 1994). All of these factors contribute to the complexity of magnetic fabric interpretation. Thus, extreme care in the analysis of rocks is needed before interpreting magnetic anisotropy, magnetic fabric, and the relating these to rock fabric.

## 2.3 Summary of characteristics

As a summary for characteristics of the samples:

1. olivine is the most major one among all minerals in the samples from Pindos and Vourinos Ophiolite. Fosterite weight percentage of most samples is more than 60 % in most samples.

2. Enstatite is not in component of every sample, and its percentage generally ranges from 0.6 % to 22.7 % . It appears to exist only in 6 samples of the 10 studies.

3. There is a obvious relationship between serpentinization and density. With the increasing serpentine volume percentage, the density of sample decreases.

4. The porosity and its related parameter permeability are surprisingly low in these rocks, typically porosities are less than 2 % and permeability less than $< 10^{-21} m^2$ at room temperature and pressure.

5. The existence of magnetite was proven by thermomagnetic analysis and isothermal remanent magnetization experiments. Magnetite shows much higher magnetic susceptibility than other paramagnetic minerals, even in a small amount. That is, magnetite appears to be one of the component carriers of magnetization in these rock samples.

# Chapter 3

# Elastic-wave velocity and anisotropy

The intrinsic elastic rock properties are important information in seismic interpretation and modeling for providing an indication of the underlying symmetry; and; here texture of the rock. As well, the elastic constants indicate the degree of anisotropy of the rocks which can be on the order of 10 % or more. Velocity anisotropy is essentially related to the elastic properties of materials. Despite this importance of this relationship in Geophysics, there have been remarkably few measurements of rock velocity anisotropy or determinations of the elastic constants carried out on rocks. The important goal here of the laboratory experiments is anisotropy determination and estimation of the rock's complex elastic behavior. In principal the stiffness tensor can be determined directly by applying normal and shear stress to the sample and observing the strains produced. However, it is often simpler to determine those same properties indirectly by measuring the elastic wave velocities and densities of the material. Based on accurate laboratory measurements, it is possible to calculate the elastic constants.

Ideally, a seismic experiment would reveal to us both geologic structure and lithology. The latter can be, in part, provided from knowledge of the *in situ* material properties. In order to obtain these physical properties from the seismic measurements, it is imperative to understand how the elastic properties of rocks can be affected by their mineralogy, content, structure, saturation, stress, and texture. It is equally important to know how seismic responses at $\sim$100 Hz can be correlated with laboratory measurements at $10^6$ Hz, considering the large gap between the two in terms of frequency and scale.

45

## 3.1 Introduction

The use of elastic wave velocity to determine velocity anisotropy and elastic coefficients has been popular in laboratory experiments for the last few decades (*Pros and Babuska*, 1967; *Van Buskirk et al.*, 1986; *Cheadle et al.*, 1991; *Johnston and Christensen*, 1995; *Mah and Schmitt*, 2001, 2003; *Cholach et al.*, 2005). The methods of experimental determination of the elastic coefficients of anisotropic materials were reviewed extensively by *Mah and Schmitt* (2001, 2003). In early studies of anisotropy, many of the materials investigated were of simple structure (e.g. highly symmetric cubic or hexagonal) with a simple elasticity requiring only a few measurements. One of the earlier attempts at determining the anisotropy of a material was by *Markham* (1957) who determined the elastic constants of various metals of cubic and hexagonal crystal symmetry through the use of the pulse transmission method. Simply, in the pulse transmission method the travel time of a disturbance transmitted through a known thickness of the sample is measured in order to provide the velocity. In an early study on rock, *Kaarsberg* (1959) found that velocities both parallel and perpendicular to the bedding increase with increasing density in shale. *Johnston and Christensen* (1995) applied the pulse transmission technique to cores of shale with the pulse being applied at various angles to the axis of symmetry. The phenomenon of shear wave splitting was observed and phase velocities were measured. Through the use of phase velocity measurements, the elastic constants of the rocks were determined. Similarly, *Vernik and Nur* (1992); *Hornby* (1996) measured P-wave and S-wave velocities of cores cut parallel, perpendicular, and at 45 degrees to the bedding surface and determined the elastic constants of rock at pressure.

Many authors have provided theoretical reviews of elastic wave propagation in various mediums; some of the better-known references include *Auld* (1990) and *Musgrave* (1970). Here, we only give a general description that begins and builds from isotropy. In an isotropic medium the P-wave and S-wave particle motions are purely longitudinal and transverse, respectively, to the direction that the wave propagates. In this ideal case, the P- and the S-wave velocities are not dependent on direction. The S-wave polarization (i.e. direction of particle motion) can be in any direction normal to the wave propagation direction; and consequently, no shear splitting is allowed.

46

In reality, the mineral crystals usually have a degree of symmetry. Common crystal symmetry system includes cubic, hexagonal, orthorhombic, monoclinic, and triclinic symmetry, which are all anisotropic media. In optical mineralogy, the rock-forming materials of these systems except for cubic are generally optically anisotropic; that is, the velocity of light is different in different directions in these materials. The different crystal systems can be differentiated in terms of axes, planes, or centers of symmetry. In seismic studies once a material is anisotropic, however, the waves through these materials are referred to as "quasi-P" waves or "quasi-S" waves, because of additional complications with regards to the relationship between directions of the particle polarization and the wave propagation. Two distinct shear waves will, generally, propagate in nearly all directions. The polarizations of these two shear waves will cause differences in their time of arrival. This birefringent phenomenon is commonly known in the geophysical community as shear wave splitting (SWS). The optical birefringence of calcite is perhaps the best analogy to this variation of S wave speeds in a given direction.

For the rocks in the deeper crust and upper mantle, the high-pressure velocity anisotropy and shear-wave splitting are thought to be caused by the LPO of minerals (*Kern*, 1993). At lower pressure, the alignment of microcracks can also contribute to the anisotropy. At greater confining pressure these cracks close (*Birch*, 1960, 1961; *Christensen*, 1965, 1966a; *Ji and Salisbury*, 1993a; *Ji et al.*, 1993b), the bulk of these cracks often close at pressure below 100 MPa.

In this chapter, I will first present a simple review of elasticity theory and its linkages to velocities; and then, a detailed study is presented on the ultrasonic properties of the ophiolite samples. I will show laboratory measurements on samples from the Pindos and the Vourinos ophiolites (Greece) to see how the serpentinization affects seismic velocity and anisotropy.

## 3.2 Brief review of elasticity theory

The fundamental relationships between elasticity and anisotropy have been comprehensively described by *Fedorov* (1968); *Musgrave* (1970); *Auld* (1990) to name a few. The following is only a brief summary. The main purpose of this section is to highlight the differ-

Table 3.1: The cyclical recipe for transformation from full to Voigt notation

| indice | ij, kl | 11 | 22 | 33 | 23 or 32 | 31 or 13 | 12 or 21 |
|--------|--------|----|----|----|----------|----------|----------|
| indice | m, n   | 1  | 2  | 3  | 4        | 5        | 6        |

ence between P- and S-wave velocities and the material's elastic properties. The quantitative measurement of such velocities and density consequently yield the elastic properties directly. The characteristics of elastic wave velocities including anisotropies reveal a large amount of intrinsic information of rocks, which implies that the anisotropies of wave velocities are closely related to rock composition, texture, and lattice-preferred orientation. Knowledge of the elastic properties are perhaps more useful than the velocities in that they directly reveal the material's symmetry and texture.

For an anisotropic medium, the generalized Hooke's law completely describes the stress-strain relationship, where the Einstein summation convention[1] will be used in (Eq.3.1):

$$\sigma_{ij} = c_{ijkl}\varepsilon_{kl} \tag{3.1}$$

Where $\sigma_{ij}$ and $\varepsilon_{kl}$ are the second order stress and strain tensors, respectively (*Musgrave*, 1970); $c_{ijkl}$ is the forth rank elasticity tensor whose components are the elastic stiffnesses which we take here to be constants.

The elasticity tensor $c_{ijkl}$ fully describes the elastic properties of anisotropic crystals or solids. Since the elasticity tensor $c_{ijkl}$ has 4 indices, each of which goes from 1 to 3, the elasticity tensor has $3^4 = 81$ elements. The symmetries in the stress and strain tensors reduces the 81 elements of the components of stiffness $c_{ijkl}$ to only 36 independent elements. Then, consideration of the thermodynamics principles that the internal energy of a material can only increase during a compression further reduces $c_{ijkl}$ from 36 to 21 independent elastic stiffnesses (*Musgrave*, 1970).

The symmetry of the tensor of elasticity allowed Voigt to introduce a simpler matrix notation (*Nye*, 1957) that is commonly used in the geophysical literature where the four indices $ijkl$ maybe replaced by two indices $mn$. The stiffness tensor for the sake of con-

---

[1]Einstein summation convention is a way of dealing with tensors in a compact and consistent way. The idea here is to use indices to describe a generic element and apply tensor algebra. The convention is simply that any repeated subscript (or indice) in an expression is a shorthand for summation over all the possible indices. This is better shown by an example in which $X_i Y_i$ is taken to mean $X_1 Y_1 + X_2 Y_2 + Z_3 Z_3$.

48

venience is written as a second-order symmetric Voigt matrix (*Nye*, 1957; *Musgrave*, 1970; *Thomsen*, 1986; *Winterstein*, 1990) in (Eq.3.2):

$$c_{ijkl} = C_{mn}(i, j, k, l = 1, 2, 3; m, n = 1, ..., 6) \tag{3.2}$$

According to the rule (*Vestrum*, 1994), the stiffness tensor $c_{ijkl}$ can be transformed to $C_{mn}$ in Eq.3.2:

$$m = \begin{cases} i, & \text{if i=j ;} \\ 9 - (i + j), & \text{if i} \neq \text{j .} \end{cases} \tag{3.3}$$

$$n = \begin{cases} k, & \text{if k=l ;} \\ 9 - (k + l), & \text{if k} \neq \text{l .} \end{cases} \tag{3.4}$$

Or, according to the cyclical recipe (Table 3.1):

This allows the generalized Hooke's Law to be simplified from Eq.3.1 to a simple matrix and vector equation:

$$\sigma_m = C_{mn}\varepsilon_n \tag{3.5}$$

Where $\sigma_m$ and $\varepsilon_n$ are 6×1 vectors containing the six independent components of the stress and the strain tensors, respectively. The stiffness tensor $c_{ijkl}$ can be represented as a symmetric 6×6 matrix $C_{mn}$ with 21 independent components.

For example, $C_{1133}$ become $C_{13}$ and $C_{1323}$ or $C_{1332}$ become $C_{54}$. Explicitly, this may be written:

$$\begin{pmatrix} \sigma_1 \\ \sigma_2 \\ \sigma_3 \\ \sigma_4 \\ \sigma_5 \\ \sigma_6 \end{pmatrix} = \begin{pmatrix} C_{11} & C_{12} & C_{13} & C_{14} & C_{15} & C_{16} \\ C_{21} & C_{22} & C_{23} & C_{24} & C_{25} & C_{26} \\ C_{31} & C_{32} & C_{33} & C_{34} & C_{35} & C_{36} \\ C_{41} & C_{42} & C_{43} & C_{44} & C_{45} & C_{46} \\ C_{51} & C_{52} & C_{53} & C_{54} & C_{55} & C_{56} \\ C_{61} & C_{62} & C_{63} & C_{64} & C_{65} & C_{66} \end{pmatrix} \begin{pmatrix} \varepsilon_1 \\ \varepsilon_2 \\ \varepsilon_3 \\ \varepsilon_4 \\ \varepsilon_5 \\ \varepsilon_6 \end{pmatrix} \tag{3.6}$$

Furthermore in this scheme, $\varepsilon_4 = 2\varepsilon_{23}, \varepsilon_5 = 2\varepsilon_{13}$, and $\varepsilon_6 = 2\varepsilon_{12}$. Each $C_{mn}$ is one of the components of a 6×6 symmetric matrix that can only have 21 independent stiffnesses. However, all 21 are required for the most general triclinic case in which there is no symmetry. It is useful to examine briefly how the elastic tensor $C_{mn}$ appears with increasing symmetry.

The components below the diagonal are the same because the matrix in Eq.3.6 is symmetric about the diagonal. The number of independent elastic constants depends on the

49

Table 3.2: Symmetries and the number of elastic constants required

| Elastic stiffness | Isotropic | Cubic | Hexagonal | Orthorhombic | Monoclinic | Triclinic |
|---|---|---|---|---|---|---|
| $C_{11}$ | $\lambda + 2\mu$ | $C_{11}$ | $C_{11}$ | $C_{11}$ | $C_{11}$ | $C_{11}$ |
| $C_{22}$ | $\lambda + 2\mu$ | Same as $C_{11}$ | Same as $C_{11}$ | $C_{22}$ | $C_{22}$ | $C_{22}$ |
| $C_{33}$ | $\lambda + 2\mu$ | Same as $C_{11}$ | $C_{33}$ | $C_{33}$ | $C_{33}$ | $C_{33}$ |
| $C_{44}$ | $\mu$ | $C_{44}$ | $C_{44}$ | $C_{44}$ | $C_{44}$ | $C_{44}$ |
| $C_{55}$ | $\mu$ | Same as $C_{44}$ | Same as $C_{44}$ | $C_{55}$ | $C_{55}$ | $C_{55}$ |
| $C_{66}$ | $\mu$ | Same as $C_{44}$ | $C_{66}$ | $C_{66}$ | $C_{66}$ | $C_{66}$ |
| $C_{12}$ | $\lambda$ | $C_{12}$ | $C_{11} - 2C_{66}$ | $C_{12}$ | $C_{12}$ | $C_{12}$ |
| $C_{13}$ | $\lambda$ | Same as $C_{12}$ | $C_{13}$ | $C_{13}$ | $C_{13}$ | $C_{13}$ |
| $C_{23}$ | $\lambda$ | Same as $C_{12}$ | Same as $C_{13}$ | $C_{23}$ | $C_{23}$ | $C_{23}$ |
| $C_{14}$ | 0 | 0 | 0 | 0 | 0 | $C_{14}$ |
| $C_{15}$ | 0 | 0 | 0 | 0 | $C_{15}$ | $C_{15}$ |
| $C_{16}$ | 0 | 0 | 0 | 0 | 0 | $C_{16}$ |
| $C_{24}$ | 0 | 0 | 0 | 0 | 0 | $C_{24}$ |
| $C_{25}$ | 0 | 0 | 0 | 0 | $C_{25}$ | $C_{25}$ |
| $C_{26}$ | 0 | 0 | 0 | 0 | 0 | $C_{26}$ |
| $C_{34}$ | 0 | 0 | 0 | 0 | 0 | $C_{34}$ |
| $C_{35}$ | 0 | 0 | 0 | 0 | $C_{35}$ | $C_{35}$ |
| $C_{36}$ | 0 | 0 | 0 | 0 | 0 | $C_{36}$ |
| $C_{45}$ | 0 | 0 | 0 | 0 | 0 | $C_{45}$ |
| $C_{46}$ | 0 | 0 | 0 | 0 | $C_{46}$ | $C_{46}$ |
| $C_{56}$ | 0 | 0 | 0 | 0 | 0 | $C_{56}$ |

elastic symmetry of the medium. The number of independent elastic constants required with the different symmetries is given in Table 3.2.

We need two independent constants ($\lambda$ and $\mu$) for isotropic symmetry (Eq.3.7). Explicitly in an isotropic medium the coefficients will be $C_{11} = C_{22} = C_{33} = \lambda + 2\mu$, $C_{44} = C_{55} = C_{66} = \mu$, and $C_{12} = C_{21} = C_{13} = C_{31} = C_{23} = C_{32} = \lambda$:

$$[C] = \begin{pmatrix} \lambda + 2\mu & \lambda & \lambda & 0 & 0 & 0 \\ \lambda & \lambda + 2\mu & \lambda & 0 & 0 & 0 \\ \lambda & \lambda & \lambda + 2\mu & 0 & 0 & 0 \\ 0 & 0 & 0 & \mu & 0 & 0 \\ 0 & 0 & 0 & 0 & \mu & 0 \\ 0 & 0 & 0 & 0 & 0 & \mu \end{pmatrix} \tag{3.7}$$

In a cubic medium the coefficients (Eq.3.8) will be $C_{11} = C_{22} = C_{33}$, $C_{44} = C_{55} = C_{66}$, and $C_{12} = C_{21} = C_{13} = C_{31} = C_{23} = C_{32}$. Although the cubic matrix looks very similar to the isotropic one, materials of cubic symmetry require 3 completely independent constants (Musgrave, 1970). It is worth reiterating that while a cubic solid, such as halite, will be optically isotropic; it is elastically anisotropic and halite crystal will have different

velocities in different directions.

$$
[C] = \begin{pmatrix} a & b & b & 0 & 0 & 0 \\ b & a & b & 0 & 0 & 0 \\ b & b & a & 0 & 0 & 0 \\ 0 & 0 & 0 & c & 0 & 0 \\ 0 & 0 & 0 & 0 & c & 0 \\ 0 & 0 & 0 & 0 & 0 & c \end{pmatrix}
\tag{3.8}
$$

In the hexagonal (TI) medium (Eq.3.9, $x = (a - b)/2$) the independent elastic coefficients will be $C_{11} = C_{22}$, $C_{33}$, $C_{44} = C_{55}$, $C_{66} = (C_{11} - C_{12})/2$, $C_{13} = C_{31} = C_{23} = C_{32}$. For this case, 5 independent constants are required (*Musgrave*, 1970).

$$
[C] = \begin{pmatrix} a & b & c & 0 & 0 & 0 \\ b & a & c & 0 & 0 & 0 \\ c & c & d & 0 & 0 & 0 \\ 0 & 0 & 0 & e & 0 & 0 \\ 0 & 0 & 0 & 0 & e & 0 \\ 0 & 0 & 0 & 0 & 0 & x \end{pmatrix}
\tag{3.9}
$$

In the orthorhombic medium (Eq.3.10) all nine elastic coefficients are independent. The 3 mutually orthogonal planes of symmetry and 9 independent non-zero elastic constants characterize orthorhombic symmetry (*Musgrave*, 1970). This form is general for all the space groups with orthorhombic symmetry.

$$
[C] = \begin{pmatrix} a & b & c & 0 & 0 & 0 \\ b & d & e & 0 & 0 & 0 \\ c & e & f & 0 & 0 & 0 \\ 0 & 0 & 0 & g & 0 & 0 \\ 0 & 0 & 0 & 0 & h & 0 \\ 0 & 0 & 0 & 0 & 0 & i \end{pmatrix}
\tag{3.10}
$$

The number of elastic constants required for some of the other classes of crystal symmetry is also listed in Table 3.2. However, of greatest relevance to studies of seismic anisotropy in rocks is the isotropic, hexagonal (TI) and orthorhombic systems. Isotropy, for example, represents a rock in which all the structural features are randomly oriented. Transverse isotropy is often found in layered sedimentary rocks. Finally, orthorhombic symmetry can be generated by mineralogic orientation in foliated and lineated metamorphic rocks. One can envisage rocks of even lower symmetry by introducing families of oriented microcracks in a rock mass that is intrinsically orthorhombic.

51

Table 3.3: Elastic stiffnesses of minerals at room pressure and temperature

| Mineral | $C_{11}$ | $C_{22}$ | $C_{33}$ | $C_{44}$ | $C_{55}$ | $C_{66}$ | $C_{12}$ | $C_{13}$ | $C_{14}$ | $C_{23}$ | $C_{15}$ | $C_{25}$ | $C_{35}$ | $C_{46}$ |
|---|---|---|---|---|---|---|---|---|---|---|---|---|---|---|
| Forsterite | 328 | 200 | 235 | 66.7 | 81.3 | 80.9 | 69 | 69 | 0 | 73 | 0 | 0 | 0 | 0 |
| Enstatite | 225 | 178 | 214 | 77.6 | 75.9 | 81.6 | 72.4 | 54.1 | 0 | 52.7 | 0 | 0 | 0 | 0 |
| Augite | 182 | 151 | 218 | 69.7 | 51.1 | 55.8 | 73.4 | 72.4 | 0 | 33.9 | 19.9 | 16.6 | 24.6 | 4.3 |
| Hornblende | 116 | 160 | 192 | 57.4 | 31.8 | 36.8 | 44.9 | 61.4 | 0 | 65.5 | 4.3 | -2.5 | 10 | -6.2 |
| Brucite | 157 | 157 | 46.3 | 21.7 | 21.7 | 56.3 | 44.4 | 12 | 0.2 | 12 | - | - | 0 | - |
| Lizardite | - | - | - | - | - | - | - | - | - | - | - | - | - | - |
| Clinochlore | - | - | - | - | - | - | - | - | - | - | - | - | - | - |
| Clinochrysotile | - | - | - | - | - | - | - | - | - | - | - | - | - | - |
| Magnetite | 275 | 275 | 275 | 95.5 | 95.5 | 95.5 | 104 | 104 | 0 | 104 | 0 | 0 | 0 | 0 |

Table 3.4: Density, symmetry, and chemical formula of minerals present in the samples

| Mineral | Symmetry | Formula | Density $(Mg/m^3)$ |
|---|---|---|---|
| Forsterite | Ortho. | $(Mg, Fe)_2SiO_4$ | 3.221 |
| Enstatite | Ortho. | $(Mg, Fe)SiO_3$ | 3.198 |
| Augite | Mono. | $(Ca, Mg, Fe)_2(Si, Al)_2O_6$ | 3.32 |
| Hornblende | Mono. | $Ca_2(Mg, Fe, Al)_5(Si, Al)_8O_{22}(OH)_2$ | 3.12 |
| Brucite | Rhombo. | $Mg(OH)_2$ | 2.38 |
| Lizardite | Hexa. | $Mg_3Si_2O_5(OH)_4$ | 2.5 |
| Clinochlore | Tri. | $(Mg, Al)_6(Si, Al)_4O_{10}(OH)_8$ | 2.7 |
| Clinochrysotile | Mono. | $Mg_3Si_2O_5(OH)_4$ | 2.55 |
| Magnetite | Cubic | $Fe_3O_4$ | 5.206 |

Again, in contrast to the previous cases, if no symmetry is present the material is treated as triclinic (Eq.3.11), which is characterized by 21 independent elastic constants (*Musgrave*, 1970):

$$[C] = \begin{pmatrix} a & b & c & d & e & f \\ b & g & h & i & j & k \\ c & h & l & m & n & o \\ d & i & m & p & q & r \\ e & j & n & q & s & t \\ f & k & o & r & t & u \end{pmatrix} \tag{3.11}$$

The single-crystal elastic stiffness, chemical formula and density of the minerals related to this study are listed in Table 3.3 and 3.4 (*Bass*, 1995; *Nickel and Nichols*, 1991). We can compare our laboratory and calculated results with these published results. Unfortunately, there is no published information available on elastic stiffness of serpentine minerals to our knowledge. This is primarily due to the difficulties in obtaining crystals of sufficient size to carry out meaningful measurements.

## 3.3 Relationship between anisotropic velocities and elastic stiffness

Elastic moduli are not observed directly; they must be indirectly determined either by static stress-strain tests or by measuring velocities in different directions through the material. In this section, an overview of the mathematical basis is observed for connecting observed velocities and densities to elastic moduli. The section ends by outlining the simple relationships between the elastic moduli and velocities measured using the symmetry axes of an orthorhombic material, as one example.

The equations of motion in terms of the components of the displacement $u_i$ using Einstein's indexing notation may be written as (*Helbig*, 1994):

$$\rho \ddot{u}_i = \sigma_{ij,j} = c_{ijkl}\varepsilon_{kl,j} = c_{ijkl}u_{k,lj} \qquad (3.12)$$

Where $\rho$ is the mass density, $u_i$ is the ith component of the displacement, and subscripts after the coma indicate differentiation with respect to the corresponding direction. The wave equation (3.12) establishes a relation between the second temporal derivative of a displacement function $u$ and its second spatial derivatives. With the assumption of the plane wave, the wave equation in anisotropic medium can be written:

$$(c_{ijkl}\beta_l\beta_j - \delta_{ik}\rho\nu^2)\alpha_k = 0 \qquad (3.13)$$

Here $\beta_i$ is a unit vector in the direction of the wave normal, $\nu$ is the phase velocity of an elastic wave propagating in the direction of $\beta_i$, $\delta_{ik}$ is the Kronecker delta. Elastic wave velocities can be calculated from the well-known elastic constants by solving the so-called Christoffel Equation (e.g. *Musgrave*, 1970). Under the plane wave assumption, these phase velocities (i.e. one quasi-P and 2 quasi-S velocities) can be obtained by solving the characteristic equation (3.13) which is:

$$det(c_{ijkl}\beta_l\beta_j - \delta_{ik}\rho\nu^2) = 0 \qquad (3.14)$$

Equation (3.14) is commonly given in the form of Christoffel's characteristic equation:

$$det(\Gamma_{ik} - \delta_{ik}\rho\nu^2) = 0 \qquad (3.15)$$
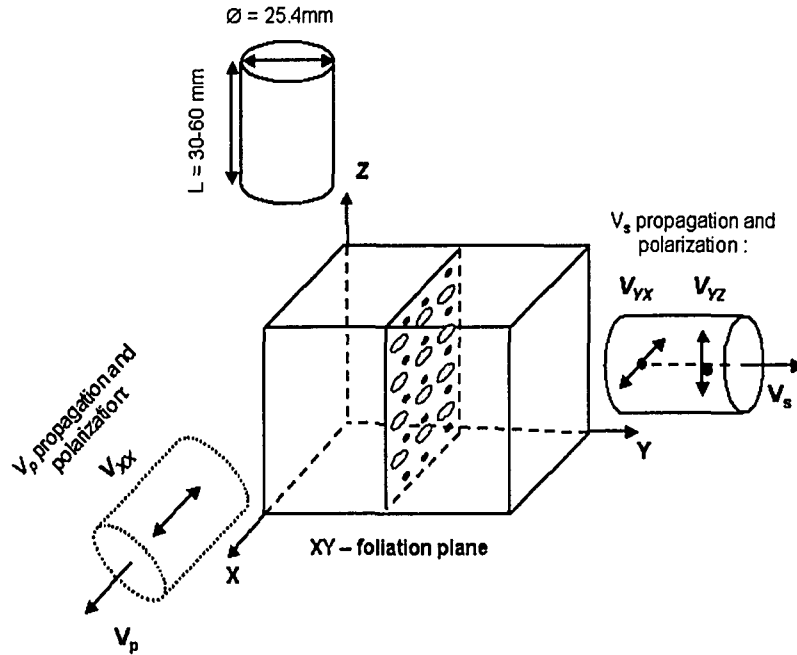
Figure 3.1: The method of mutually orthogonal plugs for measuring velocity and anisotropy (modified after *Cholach et al.* (2005)). The first subscript represents the direction of wave propagation while the second subscript represents the direction of the wave's particle displacement or polarization direction.

The matrix $\Gamma_{ik}$ is called the "Kelvin-Christoffel matrix" .

$$c_{ijkl}\beta_l\beta_j = \Gamma_{ik} \tag{3.16}$$

An eigenvalue solution of equation (3.15) for any slowness direction $n$ yields three positive values of the squared phase velocity $\nu^2$, which correspond to the speeds of the P-wave and two S-waves. The corresponding eigenvalues of this solution are the three polarization directions available. Determination of the elastic stiffness from the ultrasonic phase velocity measurement has been discussed and reviewed by previous authors (*Cheadle et al.*, 1991; *Mah*, 1999; *Mah and Schmitt*, 2003; *Cholach et al.*, 2005).

The phase velocities are associated with the propagation of a hypothetical plane wave. Generating plane waves in the real world is impossible, although at a suitable distance

from a seismic source the plane wave approximation is acceptable. Quite often, velocities are only measured in directions parallel to the symmetry axes of a material. The independent off-diagonal elastic stiffness cannot be determined given that only the values of velocities measured along the symmetry axes are determined. However, within planes of symmetry and along principal axes, the wave behavior and the formula linking velocities to elastic constants are often simple. Some assessment of the sample symmetry can be made by examination of the diagonal stiffness determined in the measurements.

Consequently, the elastic constants can be derived from phase velocity measurements using different formulae depending on the type of symmetry. Here, only the formulae for orthorhombic symmetry are given following *Cholach et al.* (2005). It is useful to refer to Figure 3.1. The P-waves along the X, Y and Z-axes are designated by XX, YY and ZZ by propagation and polarization, respectively. For example, XX signifies X propagation and X polarization direction. The two shear waves propagating in the Y direction have X and Z direction polarizations and are denoted by YX and YZ, respectively. Those propagating in the Z direction will have polarizations of ZX and ZY, see Figure 3.1. As such only six of the nine existing elastic constants may be determined by measurements taken along the symmetry axes of orthorhombic materials (equation 3.17) . Orthorhombic symmetry is expected to be the most complex intrinsic in a rock and the two cases of isotropic and transversely isotropic may be deduced from the relations for measurements along they symmetry axes of an orthorhombic medium are (*Cholach*, 2005):

$$C_{11} = \rho V_{xx}^2, C_{22} = \rho V_{yy}^2, C_{33} = \rho V_{zz}^2, C_{44} = \rho V_{yz}^2, C_{55} = \rho V_{xz}^2, C_{66} = \rho V_{xy}^2, \qquad (3.17)$$

We further note that *Song et al.* (2004) have attempted to obtain all 5 independent elastic constants for a transversely isotropic materials from four measurements. However, this can only be accomplished under a series of restrictive assumptions about the nature of anisotropy in such media.

## 3.4 Laboratory measurement of elastic-wave velocity and anisotropy

This study describes a set of ultrasonic laboratory techniques to measure and calculate the P- and S-wave velocity and anisotropy. The relationship between wave velocities and anisotropy and their directional dependence with confining pressure are given. In this

Table 3.5: The length, mass, and orientation of samples

| | Plugs oriented to foliation | | | |
| Sample | Parallel | Perpendicular | Mass (g) | Length (mm) |
|---|---|---|---|---|
| P03-1 | P03-1, P03-1B' | P03-1B | 49.96/67.17/98.28 | 31.40/42.20/98.28 |
| P04-2 | P04-2 | P04-2B | 62.56/54.17 | 43.84/38.09 |
| P08-3 | P08-3B | P08-3 | 72.19/94.40 | 47.84/62.07 |
| P11-1 | P11-1 | P11-1B | 90.40/82.53 | 55.99/50.64 |
| P12-1 | P12-1 | P12-1B | 46.01/94.29 | 28.62/58.96 |
| P13-1 | P13-1 | P13-1B | 55.25/41.60 | 42.71/32.33 |
| P13-2 | P13-2 | P13-2B | 58.28/74.15 | 45.54/57.04 |
| P16-3 | P16-3B | P16-3 | 91.89/106.20 | 65.40/76.97 |
| P 08-4 | P08-4 | | 88.74 | 58.00 |
| V 03-7 | V03-7 | | 72.36 | 49.31 |
| V 03-11 | V03-11 | | 93.53 | 63.20 |

particular study, the P- and S-wave velocities exhibit a weak anisotropy caused primarily by the lattice preferred orientation (LPO) of the minerals in the sample.

### 3.4.1 Sample preparation

The samples were acquired to be used in high pressure and temperature rheological studies by Dr. J. Escartín of Institute de Physique du Globe, Paris, France. The selected samples are more olivine rich than conventional peridotites so that the rheological studies can be made on a relatively simple rocks (i.e. mostly olivine and serpentine family minerals). The core plugs were extracted at mutually orthogonal directions, as illustrated in Figure 3.1, along one or two of the three axes of symmetry, as allowed by the hand sample dimensions. In this study, the cores were drilled parallel or perpendicular to visible textural features, as the specimen allowed.

The diamond-cut cylindrical cores were 2.54 cm in diameter with lengths ranging from 3.0 to 6.0 cm. Where each specimen allowed, one core was cut perpendicular to the foliation plane and at least one other sample was cut parallel to the foliation plane. In cases where there is a visible lineation direction, two cores parallel and perpendicular to the lineation direction were cut within the foliation plane. Samples are prepared by grinding both faces flat to within 0.01mm and parallel to within 0.1mm. After cutting and flattening, the cores are dried in an oven for about 6 hours at a temperature of $80^{\circ}C$ at room pressure. The mass, length, and orientation of all samples are listed in Table 3.5.

The piezoelectric ceramics (2.54 cm diameter, 1-MHz frequency, P-wave transducers

or 18 × 18 mm size, 1-MHz frequency, S-wave transducers) were placed at both ends of the cores for the P- and S-wave measurements, respectively. To be clear, each sample needed to be prepared three times: once with the P-wave transducer and twice with the two S-wave transducers at orthogonal orientations. An attempt to employ stacked piezoelectric ceramics in order that all the tests could simultaneously be conducted failed.

Five-minute epoxy is used to bond the transducer to the sample. The S-wave ceramics provide a mechanical pulse polarized parallel to the ends of the samples and care need to be taken to ensure that the polarization directions of both transverse mode ceramics were properly aligned to each other and appropriately oriented with respect to the rock's principal textural X, Y, and Z axes. The attached ceramic transducers and rock sample were then hermetically sealed to exclude the pressure vessel fluid from the rock and this assemblage was placed in the pressure vessel. A state of hydrostatic confining stress is achieved by increasing vessel pressure; the pressure medium is hydraulic oil. All experiments were conducted at ambient room temperature ($\sim 25^\circ C$ to $\sim 27^\circ C$).

Because of the small size of the outcrop specimens, only P 03-1 was large enough to allow 3 cores to be cut, two of which were cut parallel in order to check heterogeneity. In most of other rock samples, only a perpendicular pair of core could be drilled, excluding samples P 08-4, V 03-7, and V 03-11 where the outcrop sample size allowed only one core to be cut, and hence no estimate of the anisotropy can be made.

### 3.4.2 Experiment and Measurement

The laboratory velocity measurements were carried out using the ultrasonic pulse transmission technique (e.g. *Birch*, 1961; *Kern*, 1982). In our implementation a high voltage (200 V) rapid rise-time ($\sim 8$ ns) step-pulse from a generator (Model 5800, PANAMETRICS) activates the mechanical vibrations in the source piezoelectric transducer. These mechanical vibrations travel through the rock sample and are received at the end by the receiving piezoelectric transducer that transforms the mechanical vibrations back into electrical signals. A digital oscilloscope used in the experiment receives two signals: the trigger signal from the pulse generator to synchronize the oscilloscope with the initiation of the pulse, and a delayed signal that travels through the rock sample to the receiving transducer.

## 3.4. LABORATORY MEASUREMENT OF ELASTIC-WAVE VELOCITY AND ANISOTROPY

A conventional pulse transmission technique (*Molyneux and Schmitt*, 1999, 2000) was used to obtain P- and S-wave velocities using longitudinally and transversely polarized piezoelectric ceramics, respectively. The Rock Physics Laboratory has developed a Velocity Anisotropy Measurement System that can make high-resolution measurements of many velocity components over a complete volume of rock cores. There are a number of high speed digital oscilloscopes (GaGe, Model No. 400-586-203) that are used primarily in ultrasonic measurements of P-wave and S-wave speeds with material under pressures as great as 300 MPa and at different temperatures. The transmitting piezoelectric ceramic was activated by a fast rise-time high voltage pulse, which generated an appropriate mechanical wave. Transmission through the serpentinite is generally strong and as such no amplification was employed. The signals received by the oscilloscope are recorded in a computer. Then, the Matlab programs are developed to pick the travel time. In practice, we choose the first peak or trough to pick the first arrival. This provides a good estimation of the travel time because the waveform may evolve due to attenuation.

Seismic velocities are usually measured from three mutually perpendicular directions in each sample, although this does not constitute a complete set of data for determination of all the elastic constants, as noted previously. For the rocks in which both a foliation and a lineation are developed, their directions are aligned to all X, Y and Z-axes of the tectonic framework with X - parallel to the stretching lineation, Y - perpendicular to the lineation and parallel to the foliation, and Z - normal to the foliation (Figure 3.1). If the sample is foliated but not obviously lineated, both X and Y directions are arbitrarily aligned in the foliation plane.

In this study, the P- and S-wave velocities of rock samples are measured using the pulse transmission technique (instrument setup shown in Figure 3.2). Transmitting and receiving transducers were mounted at the opposing ends of the cylindrical samples. P-wave and two S-wave measurements were made on all the cores in longitudinal mode. One or two sets of sample could be used for each run. Each sample requires 1 P-wave and at least two orthogonally oriented S-wave runs. In each run, waveforms are acquired over the range of confining pressure from 0 to 300 MPa with an interval of 5 MPa and then back from 300 MPa to 0 MPa at the same pressure interval. Pressure is applied, not so much to mimic *in situ* conditions, but to close as many of the microcracks in the rocks
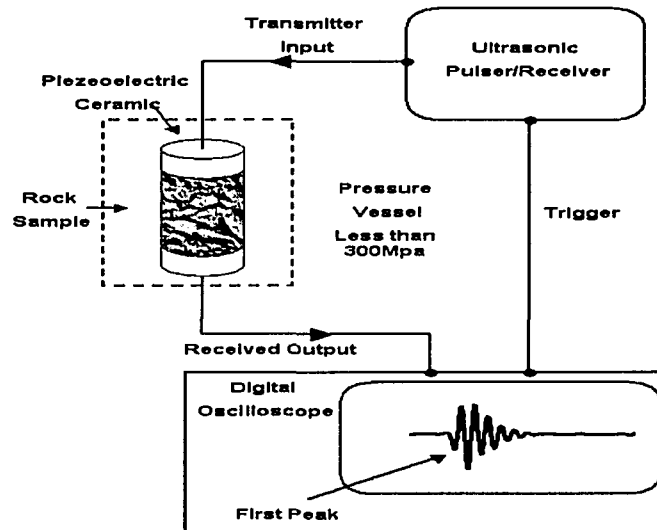
Figure 3.2: Schematic showing acoustic experiment setup, modified after *Molyneux and Schmitt* (1999).

as possible in order that the velocities are representative of the intrinsic mineralogical texture of the sample.

The time difference between the two signals received by the oscilloscope is the time that it takes the signal to travel through the electrical leads as well as through the sample itself. The electrical delay can be eliminated according to laboratory measurement and calculation. The velocity of the sample is calculated from its length and travel time of the signal after correcting for the delay time.

$$V = \frac{L}{t_T - t_D} \tag{3.18}$$

Where: $V$ is P-wave or S-wave velocity; $L$ is the length of the sample; $t_T$ is the travel time of signal; $t_D$ is the delay time.

A good deal of efforts goes into the core sample sealing. Despite our best efforts, occasionally hydraulic oil does penetrate the sample. If this occurs then testing is immediately stopped. Part of our quality control effort is to carefully examine each sample for leakage after testing. If leakage is detected, then the sample is cleaned and the process is

59

repeated again until satisfactory results are achieved and no leakage is detected.

### 3.4.3 Error analysis

Using a method similar to that described by *Yin* (1992), the absolute errors in the measurement may be analyzed by the partial differentiation from the equation (3.18):

$$\Delta V = \frac{\partial V}{\partial L}\Delta L + \frac{\partial V}{\partial t_D}\Delta t_D + \frac{\partial V}{\partial t_T}\Delta t_T \tag{3.19}$$

And the absolute error can be evaluated as

$$\Delta V = \Delta L \left|\frac{1}{t_T - t_D}\right| + L \left|\frac{\Delta t_T}{(t_T - t_D)^2}\right| + L \left|\frac{\Delta t_D}{(t_T - t_D)^2}\right| \tag{3.20}$$

Where $\Delta t_T$ and $\Delta t_D$ are taken to be the oscilloscope's time resolution of 125 million samples per second (i.e., 8 ns per sample), and $\Delta L$ is the absolute error in sample length measurement. To estimate errors we considered a typical sample length of 30 mm measured with a precision 0.01 mm by the electronic digital caliper over the flattened faces; $\Delta L$ can be less than 0.1 mm. Since $t_T - t_D$ is in the range from 4.3 to 11 $\mu s$ and is typically near 7 $\mu s$ for P waves in these experiments, the typical P wave velocity error calculated by the above equation is $\pm$ 24 m/s. This corresponds to a relative error in the velocity estimation of approximately 0.4 % for a P-wave propagating at a velocity near 6000 m/s. Similarly, for the S-waves, $t_T - t_D$ is in the range from 8 to 20 $\mu s$ and typically near 14 $\mu s$, thus, the maximum absolute error $\Delta V$ will be 10 m/s in the case of others are as same as before. This corresponds to a relative error in the velocity estimation of approximately 0.3 % for a S-wave propagating at a velocity near 3500 m/s.

## 3.5 Results and Discussion

In this study, P- and S-wave velocities have been measured 3 times on each of the 20 cores taking from 11 hand samples, requiring over 60 individual runs were made with the pressure vessel. The results from one S-wave run consisting of 79 traces (i.e. the image of amplitude with time at different pressures) highlights the well-known decrease in pulse transit times and the increment in amplitude with increasing confining pressure (Figure 3.3). Figure 3.4 is a graph of a S-wave pulse train taken from one of the waveforms
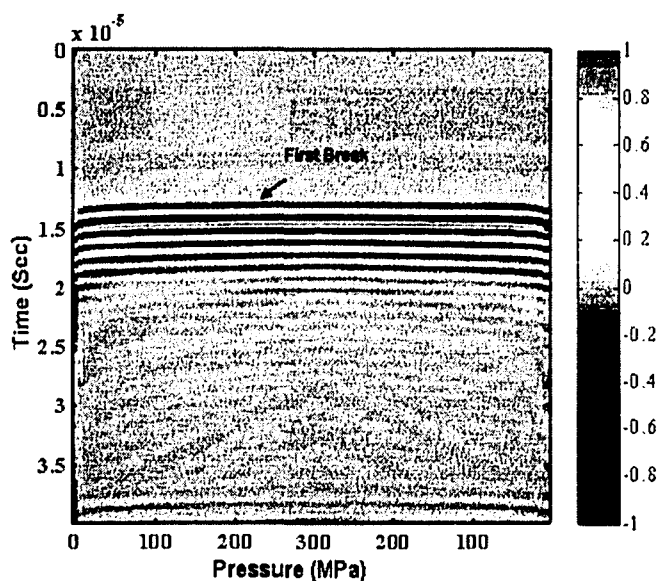
---

60

Figure 3.3: Waveform trace during one pressure cycle. Color bar corresponds to waveform amplitude (P 11-1)

imaged in Figure 3.3. The pulse first extremum (here a negative polarity) was used to determine the transit time and in Figure 3.4 this is the first trough. The S-wave waveforms acquired in a complete pressure cycle are shown in Figure 3.5. An example of the velocities and anisotropy measurements during both pressurization and depressurization is shown in Figure 3.6 for sample P 12-1.

### 3.5.1 Compressional wave results

Compressional wave results for 11 samples from Pindos and Vourinos Ophiolites (Greece) are presented with respect to confining pressures from 0 to 300 MPa. As a first observation, it is noteworthy to mention that the values and slopes of velocities measured as pressure increases and decreases are similar because of the low porosity of the samples (Figure 3.6). Generally speaking, velocities measured as pressure is first increased tend to be lower than those measured during depressurization. This is attributed to the closure of microcracks at high pressure that do not completely reopen during depressurization (*Birch*, 1960). All velocities reported were measured while increasing pressure in Table
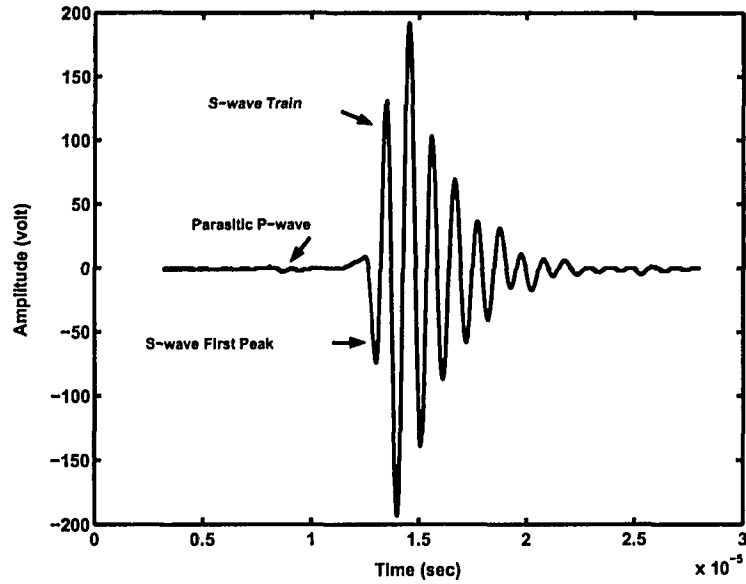
Figure 3.4: An example of typical shear wave trace from Figure 2.4



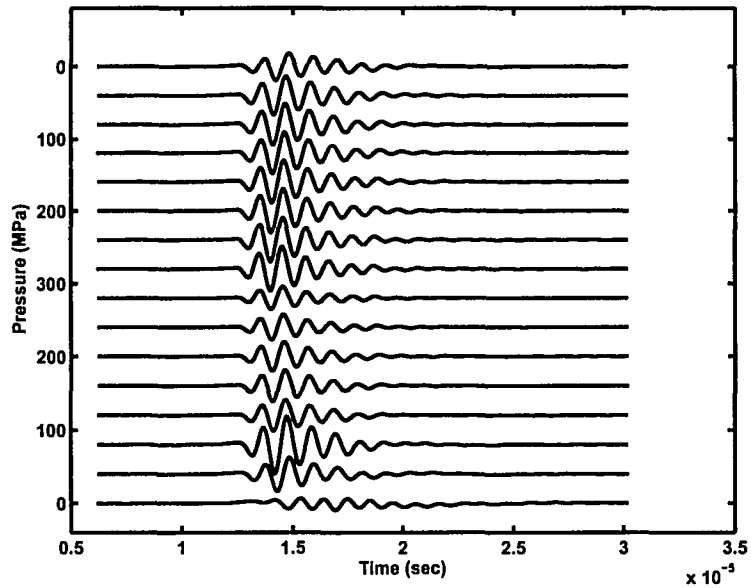Figure 3.5: Acquired S-wave waveforms using pulse transmission method (sample P11-1, ZY plane).
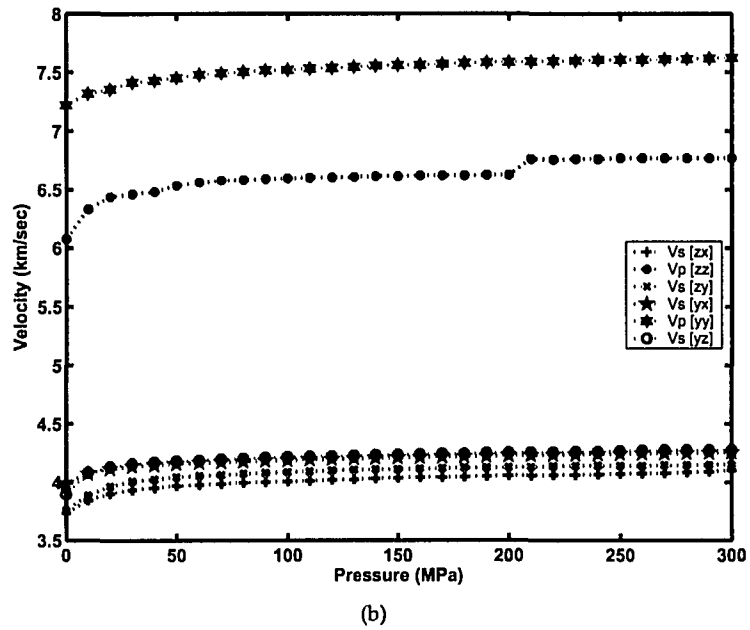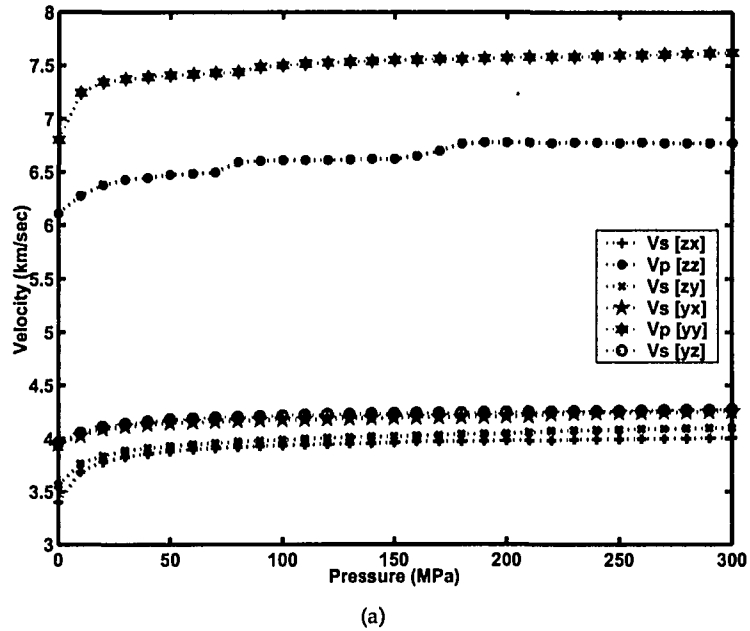
(a)



(b)

Figure 3.6: Measurements of velocities and anisotropy (P 12-1). Top: Velocities as pressure increases. Bottom: Velocities as pressure decreases

63

3.6. The velocity vs. pressure curves for all samples display an initial non-linear increase in velocity at low pressures followed by a more gradual linear increase at high pressures. This characteristic curve has been attributed to closure of microcracks in the samples with increasing pressure to 100 MPa, above which the rocks can be considered as compacted aggregates (*Birch*, 1960; *Christensen*, 1965). In general, however, it must be noted that the rocks currently under study initially display highly linear velocity versus pressure behavior that begins even at pressures below 50 MPa. This is usually not the case for igneous or metamorphic rocks that contain microcracks, and these observations provide further evidence that the microcrack porosity in these samples is small.

Based on the whole rock analysis in Chapter 2, Forsterite is the major part of the samples (Talc existing in P11-1, P08-3, P08-4 without the estimation of weight percentage by this method; Brucite existing in P13-1 and P13-2, weight percentage 10.2 % and 10.3 %, respectively). The degree of serpentinization of the samples has been estimated by mass density measurement, using the linear relationship between density and serpentinization established by *Christensen* (1966b, 1972). Basically, high mass density corresponds to low serpentinization because of low-density feature of serpentine minerals. A comparison between sample P 03-1, which has only a low serpentinization (density 3.19 $g/cm^3$; serpentine ratio 13.6 %), and sample P 13-2 in Figure 3.7, which is highly serpentinized (density 2.6 $g/cm^3$; serpentine ratio 87.9 %), suggests that degree to which velocity increases with pressure is initially related to the rock microstructure and mineralogy. Samples with low serpentinization exhibit more a pronounced rise in velocity, P-wave anisotropy, and $\frac{dV_p}{dP}$ slope than the highly serpentinized samples at pressures less than 50 MPa.

Above 50 MPa the velocity-pressure relationship can be described by the linear equation:

$$V_p = (V_p)_0 + P(dV_p/dP) \qquad (3.21)$$

Where $(V_p)_0$ is the projected zero pressure velocity and $\frac{dV_p}{dP}$ is the high-pressure slope. $(V_p)_0$ and $\frac{dV_p}{dP}$ for each sample are given in Table 3.6, with average $\frac{dV_p}{dP}$ varying from 4 to $9 \times 10^{-4} km/s/MPa$.

The average P-wave velocity, which is equal to $[V_{yy} + V_{zz}]/2$ in this study (for these samples that allowed for multiple measurements), is shown as a function of pressure in Figure 3.8. With increasing pressure, all the P-wave velocities rapidly rise in the low-
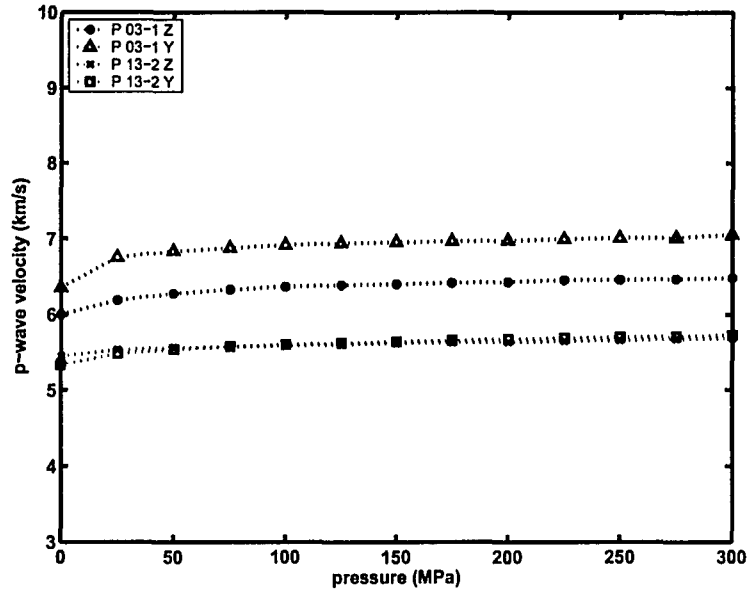
Figure 3.7: P-wave velocities vs. pressures in Z, and Y directions through sample P 13-2 and P 03-1

pressure range (less than 100 MPa) due to closure of most of the microcracks; then, at higher pressures the increment of velocity tends to be slower. In general, $V_p(zz) < V_p(yy)$; the sample P 08-3 and P16-3 show the reverse relationships between first and second sample P-wave velocity measurement by the reason of sampling orientation. A general trend of decreasing velocity with decreasing density is apparent in Figure 3.9.

The densities were determined at room pressure because the effect of pressure on density is small for such low-porosity samples ($< 2\%$). Figure 3.8 also illustrates the variation of the mean P-wave velocity among the samples. Density is the major influence because of the relatively low level of anisotropy and the heterogeneity of the samples. Although the average P-wave velocity generally increases with density, the velocity anisotropy or the heterogeneity of some samples may still gives rise to considerable velocity scatter in the P-wave velocity-density relationship. This may in part be due to differences in composition as outlined in Chapter2.

The coefficient of anisotropy was defined by *Birch* (1961) as:

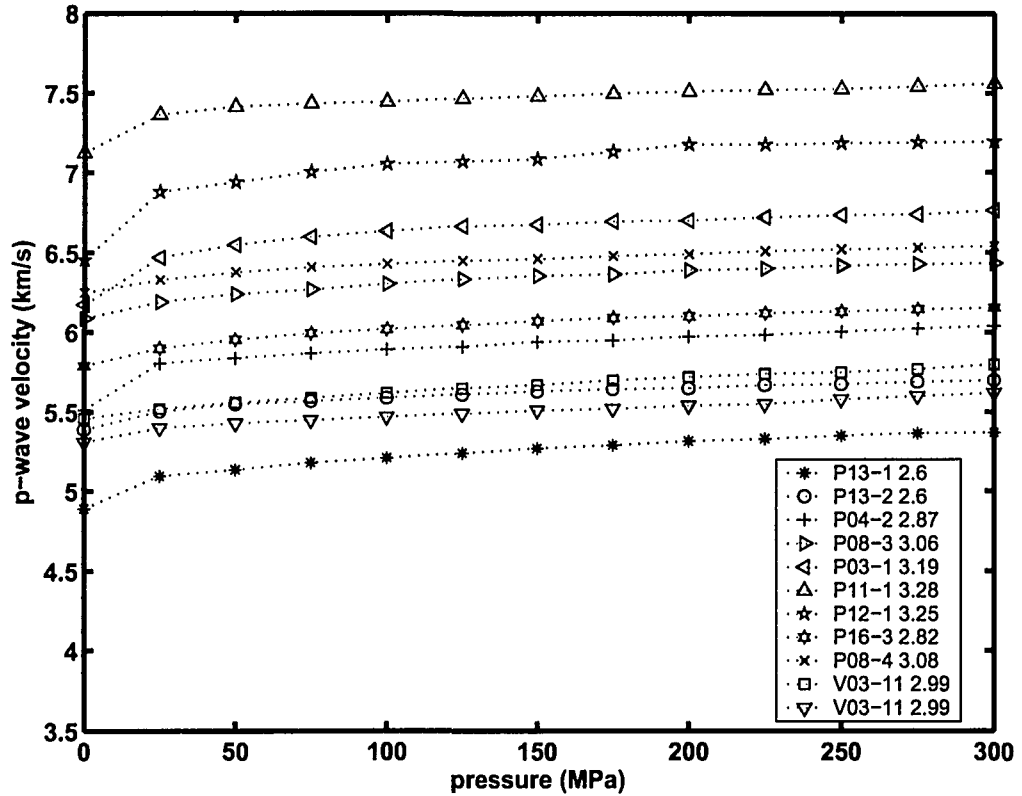$$A = 100\%(V_{max} - V_{min})/V_{mean} \qquad (3.22)$$

Figure 3.8: Mean P-wave velocities as a function of pressure at room temperature; average density following the sample name.

In many samples, $A$ varies with pressure and density. The general relationship between density and P-wave anisotropy can be shown in the Figure 3.10. The P-wave anisotropy increases roughly with increasing density, except for the sample P11-1 due to its randomly aligned grain texture (see its thin section Figure A.5 in Appendix). This suggests that the serpentinization decreases the anisotropy in the material studied here.

In general, two patterns have been observed in the relationships between pressure and P-wave anisotropy (Figure 3.11):

*Pattern*1): the anisotropy for 2 samples (P 12-1 and P03-1, both low serpentinization) increases rapidly with increasing pressure in the low-pressure domain ($<$ 50 MPa), and then decreases in the high-pressure domain (Figure 3.11). This variation can be attributed
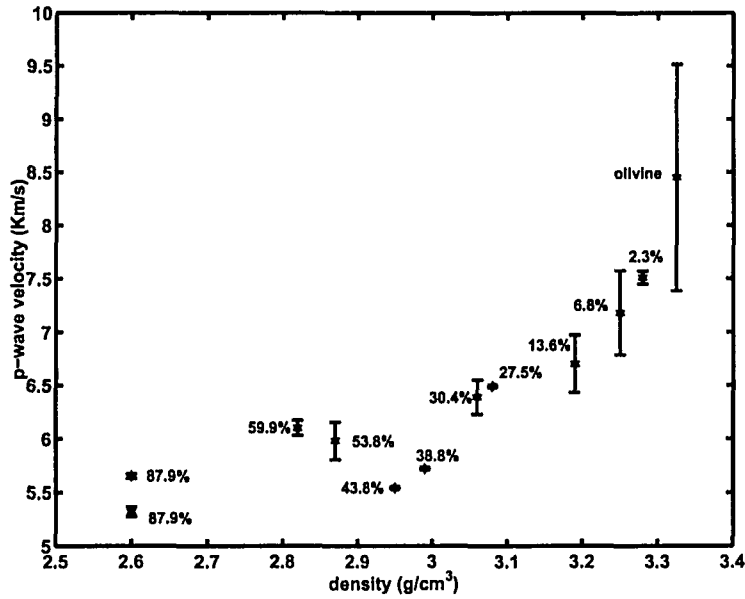
66

Figure 3.9: Mean Vp vs. density at 200 MPa and room temperature (Errorbar range from Vmin to Vmax; percentage is serpentinization degree)
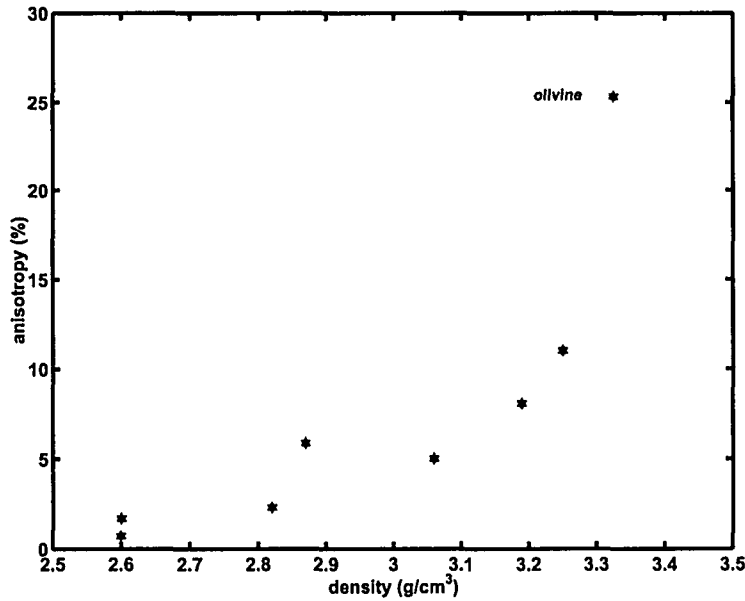


Figure 3.10: P-wave anisotropy vs. density at 200 MPa and room temperature
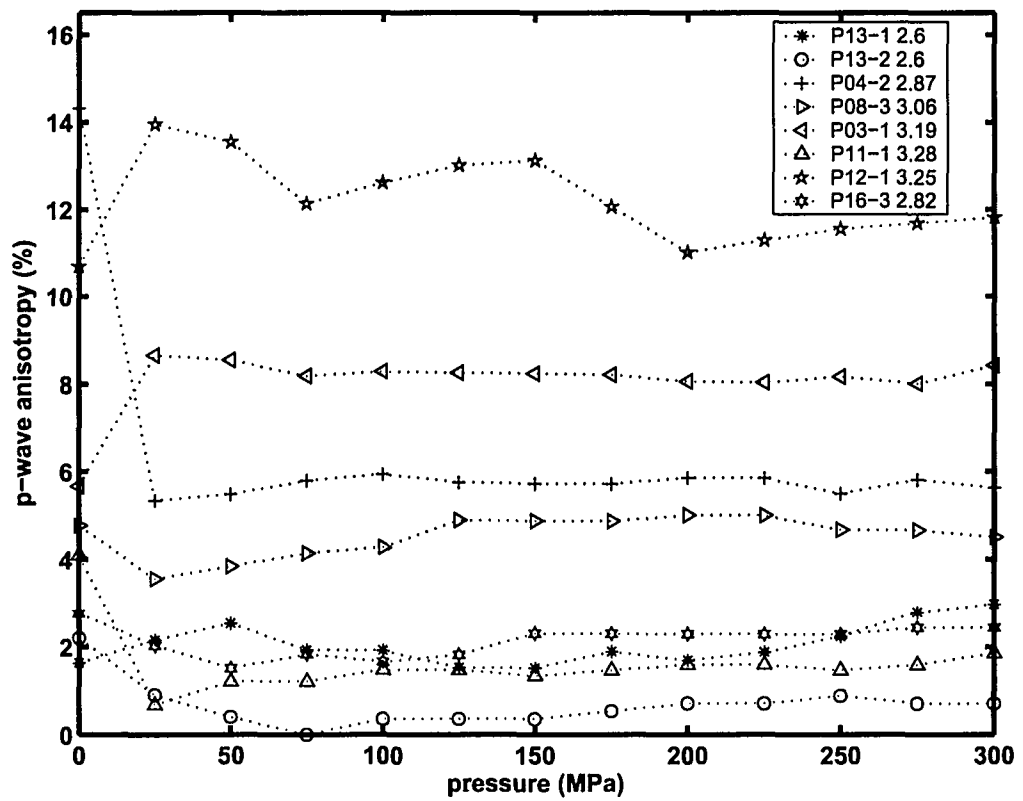
67

Figure 3.11: P-wave anisotropy vs. pressure; average density following the sample name

to the rapid closure of oriented cracks at low pressure that oppose the LPO anisotropy (*Ji and Salisbury*, 1993a; *Ji et al.*, 1993b); and *Pattern2*): the anisotropy for 5 samples (P04-2, P08-3, P13-2, P11-1 and P16-3) decreases with increasing pressure in the low-pressure domain ($< 50$ MPa), and then increases slightly in the high-pressure domain (Figure 3.11). These samples are mostly quasi-isotropic and highly serpentinized. The relationship between Vp anisotropy and confining pressure can be attributed to the closure of the oriented microcracks, which reinforce the anisotropy due to the lattice-preferred orientation (LPO) of rock-forming mineral. The slight increase of Vp anisotropy with increasing pressure probably results from differences in the pressure sensitivity of Vp in the X, Y and Z directions.

### 3.5.2 Shear wave results

Table 3.7 lists the measured shear-wave velocities for 11 samples from Pindos and Vourinos Ophiolites (Greece) as a function of pressure, propagation direction and polarization direction. The velocities were measured during pressurization. In general, velocities measured during pressurization tend to be lower than those observed during depressurization in our pressure range.

As with the P-wave velocities, many of the samples display a rapid, non-linear increase in Vs ($< 50$ MPa) that evolves to a slower linear increase at higher pressure (Figure 3.12). This character has been attributed to closure of microcracks in the samples at low pressures (e.g. *Birch*, 1960). The rocks can be considered as a compact aggregate (*Christensen*, 1965) and the velocity-pressure relationship can be described by the linear equation in the high-pressure range:

$$V_s = (V_s)_0 + P(dV_s/dP) \tag{3.23}$$

Where $(V_s)_0$ is the projected zero-pressure velocity (in $km/s$), and $\frac{dV_s}{dP}$ is the high-pressure slope; $(V_s)_0$ and $\frac{dV_s}{dP}$ for each sample are given in Table 3.7, with average $\frac{dV_s}{dP}$ varying from 2 to $4.25 \times 10^{-4} km/s/MPa$ at pressures above 50 MPa.

The mean shear-wave velocity in this study, defined as: $[Vyx + Vyz + Vzx + Vzy]/4$, is plotted as a function of pressure in Figure 3.12. While the shear wave velocities are sensitive to microcracks and density, as noted above, the higher density samples (P 03-1,
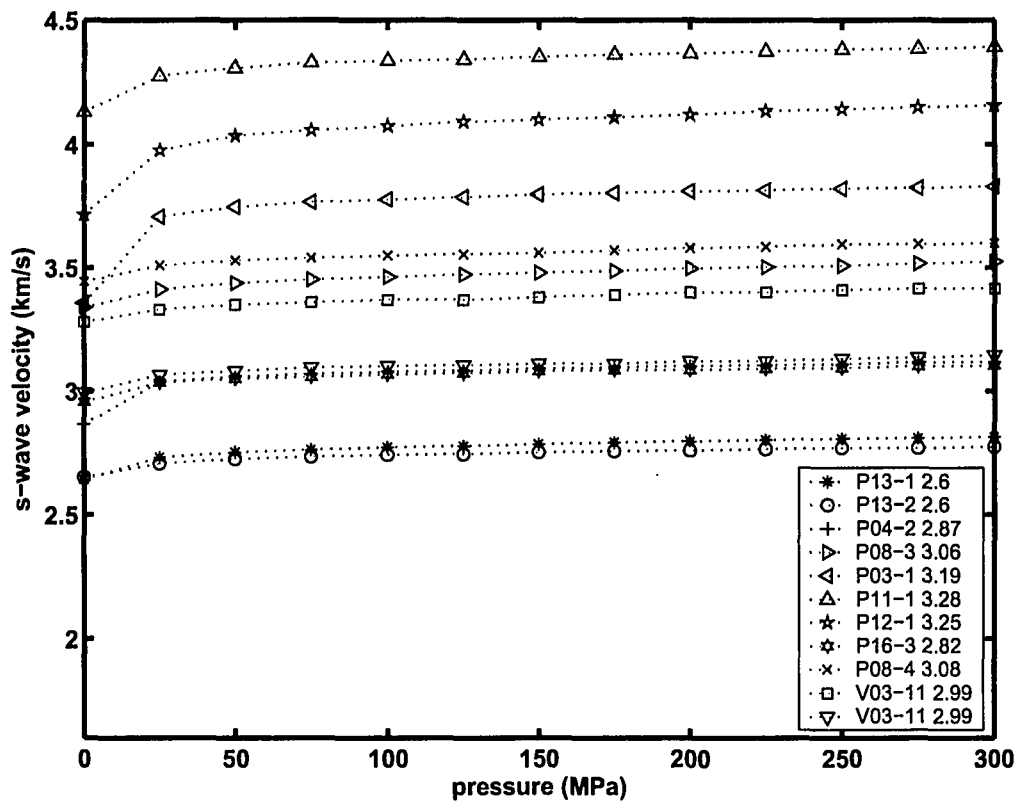
Figure 3.12: Mean S-wave velocity as a function of pressure at room temperature; average density following the sample name
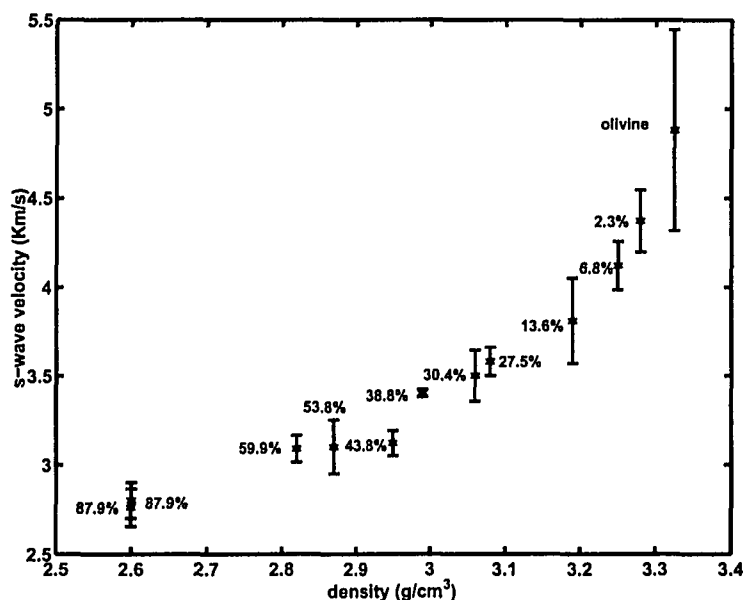
Figure 3.13: Mean S-wave velocity vs. density at 200 MPa and room temperature (Error-bar range from Vmin to Vmax; percentage is serpentinization degree)

P12-1, P11-1) display high average velocities (3.81 - 4.37 km/s, 200MPa). The low density samples with an apparent high degree of serpentinization (P 13-1 and P 13-2) display much lower average velocity (2.76 - 2.8 km/s, 200MPa).

Figure 3.13 illustrates the variation of S-wave velocity with density. The S-wave velocities show a clear and constant increment with density. However, as will be seen, the rate of change of S-wave velocity with density is relatively greater than that for P-wave velocities.

Figure 3.14 illustrates the variation of S-wave anisotropy with density. There is not a clear relationship between S-wave anisotropy and density, which may be caused by the complexity of S wave polarization and simple visual sampling orientation. Alternatively, there may not be any clear relationship between shear wave anisotropy and serpentinization.

As noted in Chapter 1, there has been some discussion as to the degree to which serpentinization influences the structure of the oceanic crust; and one way to separate this is to look at relative differences between Vp and Vs. This is typically done by
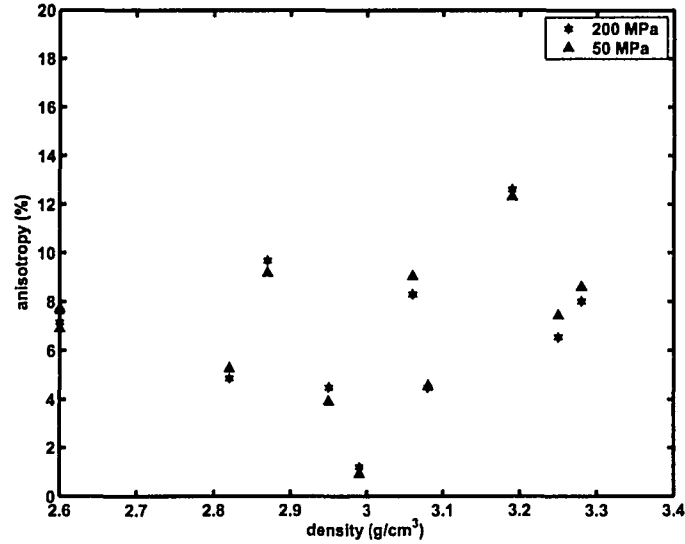
---

71

Figure 3.14: S-wave anisotropy vs. density at 50 / 200 MPa and room temperature

two ways, either by calculating the simple ratio Vp/Vs ratio or Poisson's ratio: $\sigma = \frac{1}{2}\left\{1 - 1/[(\frac{V_p}{V_s})^2 - 1]\right\}$. Figure 3.15 illustrates the variation of the $Vp/Vs$ ratio and Poisson's ratio with density at 200 and 50MPa, respectively. In general, both the Vp/Vs ratio and Poisson's ratio are larger at 200MPa than at 50 MPa; the Vp/Vs ratios and Poisson ratios have similar slopes of -0.5 and -0.15, and an uniform decrease with density at 50 MPa and 200 MPa. That is, there is a continuous increment of Vp/Vs ratio and Poisson's ratio with low density that may correspond with an increase in serpentinization in the Pindos and Vourinos Ophiolites. The Poisson's ratio and Vp/Vs ratio at 200 MPa are shown in Table 3.8.

The shear-wave anisotropy coefficient, $A_s$, is defined as:

$$A_s = 100\%(Vs_{max} - Vs_{min})/Vs_{mean} \tag{3.24}$$

Figure 3.16 illustrates the variation of S-wave anisotropy with pressure(less than 50 MPa). S-wave anisotropy generally increases with increasing pressure at low pressure except P04-2 and P12-1. We attribute the variation in S-wave anisotropy with pressure to the rapid closure of oriented cracks at low pressure that oppose the LPO anisotropy. For P04-2 and P12-1, S-wave anisotropy decreases with increasing pressure at low pres-
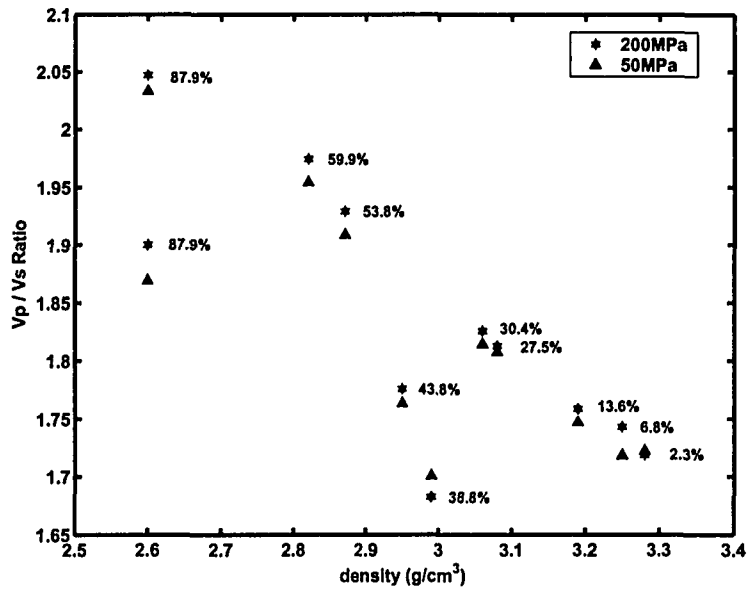
(a)
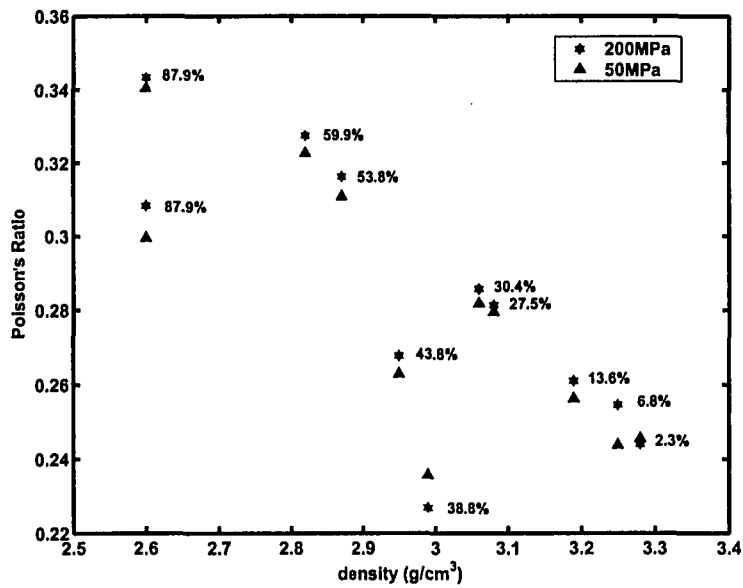


(b)

Figure 3.15: Poisson's Ratio and Vp/Vs ratio vs. density at 200 / 50 MPa and room temperature; percentage is serpentinization; Top: Vp/Vs ratio vs. density Bottom: Poisson's Ratio vs. density; $\sigma = \frac{1}{2}\left\{1 - 1/[(\frac{V_p}{V_s})^2 - 1]\right\}$
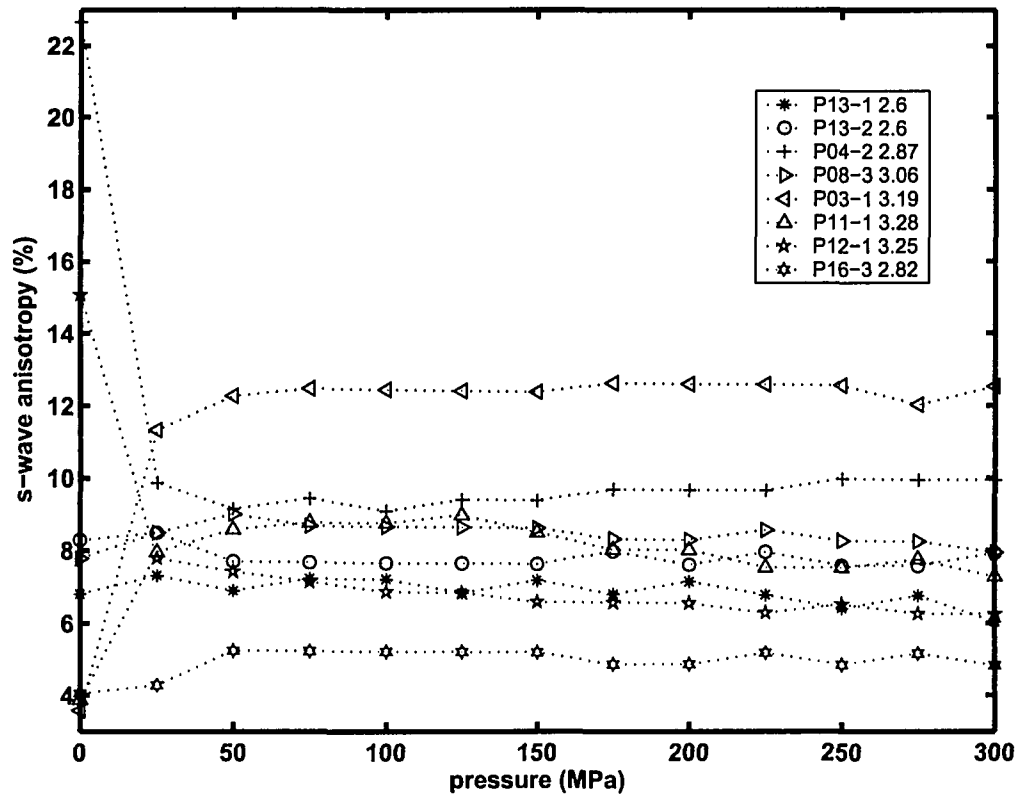
73

Figure 3.16: S-wave anisotropy vs. pressure; average density following the sample name

sure. This relationship can be attributed to the closure of the oriented microcracks that reinforce the anisotropy. As pressure higher than 50 MPa, all variations are small, and gradually reach a constant value.

The shear-wave splitting coefficient $(\Delta V_s)$ is defined as the difference in velocity between two orthogonally polarized shear waves traveling in the same propagation direction. As can be seen in Table 3.7 and Figure 3.17 and 3.18, $\Delta V_s$ is sensitive to a variety of factors, including pressure, mineralogy and propagation direction. The shear-wave splitting of samples increases or decreases at low pressure (less than 50 MPa) depending on amount of microcracks and if their directions reinforce or oppose the anisotropy. In the high-pressure field, $\Delta V_s$ roughly approaches a constant value, indicating that it is controlled by the intrinsic properties (i.e. the mineralogy and LPO) of the rocks. Below

74

the "crack-closing pressure", microcracks make a contribution to shear-wave splitting, as proposed by Crampin (1981). In general, the samples with lowest density have the smallest S-wave splitting in all directions. This again reinforces the observation of decreasing anisotropy with increasing degree of apparent serpentinization. For most samples the S-wave splitting usually ranges from 0.02 to 0.2 km/s. Generally, the largest splitting at elevated pressures is observed for waves propagating parallel to the foliation (parallel to X or Y). The most pronounced shear-wave splitting is observed in samples P 03-1 and P 11-1. As can be seen in Table 3.7 and Figures 3.17 and 3.18, for these two high density samples (with low degree of serpentinization), $\Delta V_s(Y) > \Delta V_s(Z)$ and $\Delta V_s$ typically ranges from 0.35 to 0.48 km/s in the plane of foliation. The least shear-wave splitting value is observed for propagation perpendicular to foliation.

The shear wave splitting (SWS) vs density along the Y and Z directions does not display a clear relationship in Figure 3.19. In general, the samples with low-density, and an apparent high degree of serpentinization have low SWS values and low SWS percentage.

### 3.5.3 Elastic stiffness and symmetry

Elastic stiffnesses $C_{ij}$ are calculated and estimated directly from the observed phase velocities. Table 3.9 lists the calculated elastic stiffnesses for 11 samples from Pindos and Vourinos Ophiolites (Greece).

Determination of elastic stiffnesses from the ultrasonic phase velocity measurements has long been employed (Cheadle et al., 1991; Mah, 1999; Mah and Schmitt, 2003). Within planes of symmetry and along principal axes, the elastic constants can be derived from phase velocity measurements using the formulas dependent on symmetry (Eq. 3.17).

In this study, the samples are characterized on the basis of the observed texture and the assumed symmetry. Samples in which the elastic moduli differ by less than the expected levels of uncertainty are assumed to be quasi-isotropic. In principal, those in which $C_{11} \approx C_{22} \neq C_{33}$ and $C_{44} \approx C_{55} \neq C_{66}$ are considered to be transversely isotropic. And those with $C_{11} \neq C_{22} \neq C_{33}$ and $C_{44} \neq C_{55} \neq C_{66}$ are orthorhombic. Unfortunately, only the velocities in the Y and Z directions were measured meaning that only the elastic constants $C_{22}$ and $C_{33}$ could be determined. The stiffness $C_{11}$ was not determined in
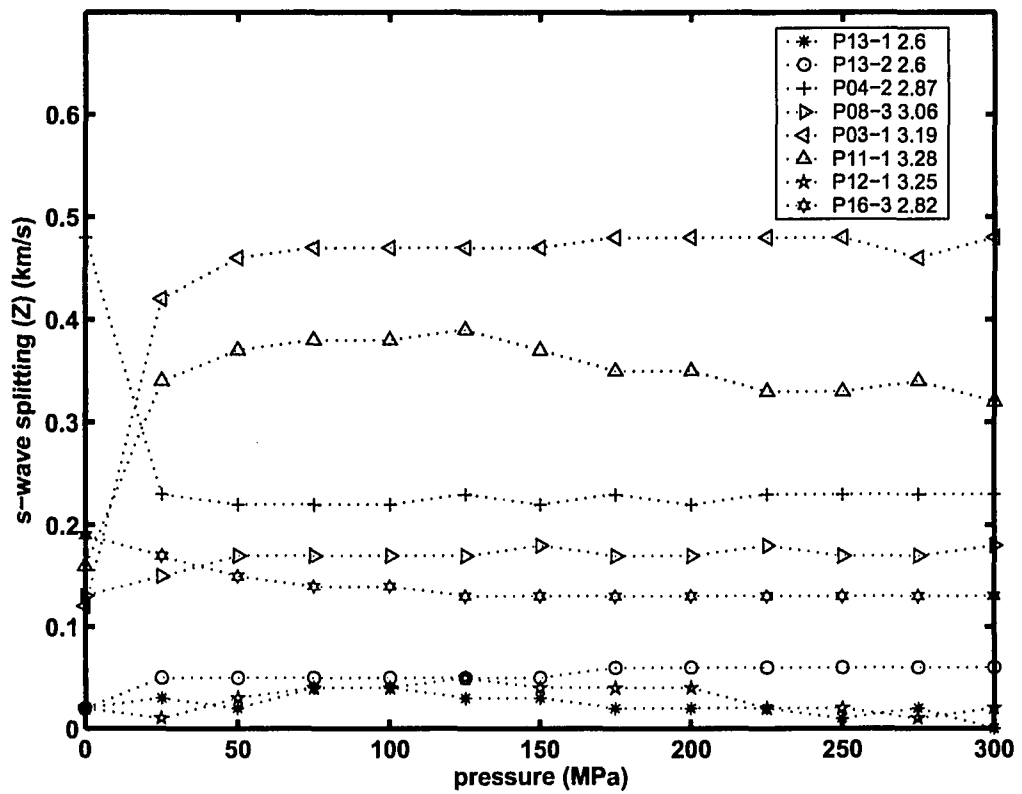
Figure 3.17: S-wave splitting (Y) vs. pressure; average density following the sample name
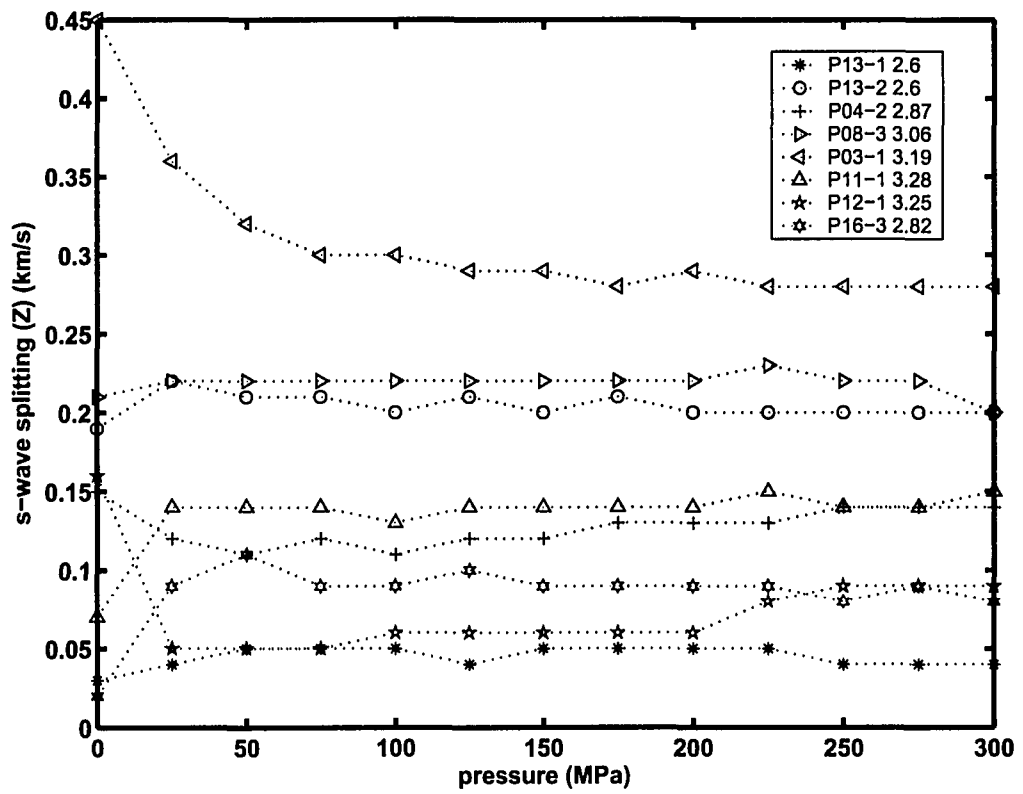
Figure 3.18: S-wave splitting (Z) vs. pressure; average density following the sample name
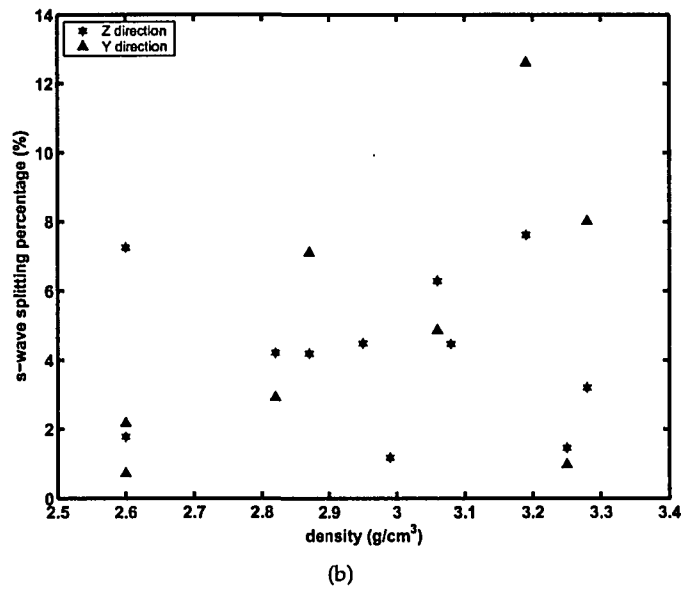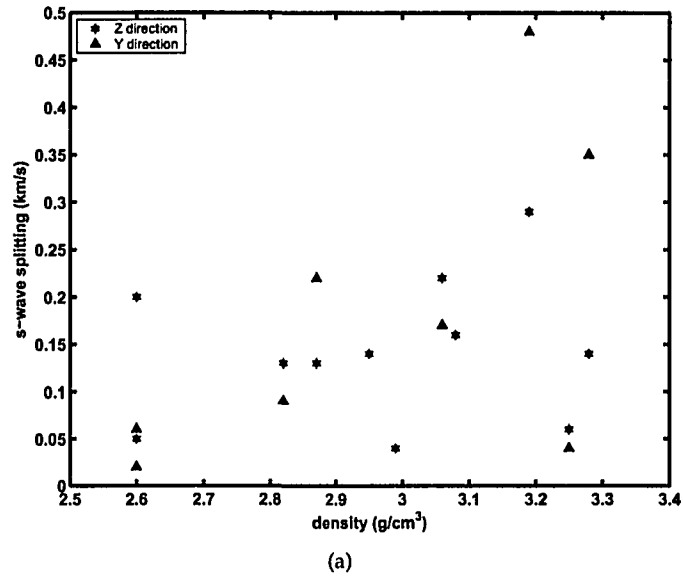
(a)



(b)

Figure 3.19: Shear wave splitting (SWS) vs. density at 200 MPa and room temperature. Top: SWS vs. density Bottom: SWS percentage vs. density

78

these tests. The symmetry of samples can only be estimated and assessed by examination of other stiffnesses determined in the measurements. As density decreases, and perhaps the apparent degree of serpentinization increases, the elastic stiffnesses of all the samples decrease, and perhaps symmetry tend to evolve from orthorhombic to quasi-isotropic. These results are summarized in Table 3.9.

### 3.5.4 Conclusion

In this study, the seismic properties and their directional dependence have been measured in eleven serpertinized dunite rock outcrop samples from Pindos and Vourinos Ophiolites (Greece). The compressional velocities were measured to confining pressures of 300 MPa in mutually orthogonal directions to investigate anisotropic properties with respect to the visible textural properties of the rocks. The shear-wave velocities were measured at two orthogonal polarizations for each direction to determine shear-wave splitting and correlate it with P-wave anisotropy. Once the material is anisotropic there will generally be compressional waves propagating with different velocities in the different directions, and the polarizations of two distinct shear waves propagating will lead to shear wave splitting. For all the samples, $V_p(Z) < V_p(Y)$. Shear wave splitting where $\Delta V_s(Y) > \Delta V_s(Z)$ is evident only in samples P 03-1, P11-1, and P 04-2. Sample symmetries estimated from relative values of the determined elastic constants show two types of symmetry, quasi-isotropic and orthorhombic.

Rock and seismic properties such as the density, serpentine ratio $\beta$, mean velocities, anisotropies, and shear wave splitting (200 MPa) are summarized in Table 3.10. In general, the P- and S-wave velocities, the percentage of P- and S-waves anisotropy, and the shear wave splitting decreases with a decrease in density, and perhaps an increase in the increasing degree of serpentinization.

As found in the work of other authors (*Ji and Salisbury*, 1993a; *Ji et al.*, 1993b; *Barruol and Kern*, 1996; *Kern et al.*, 1996; *Dewandel et al.*, 2003), the P- / S-wave velocity and anisotropy measured here on eleven samples from Pindos and Vourinos ophiolite (Greece) exhibit an intrinsic anisotropy controlled at low pressures by both the microcrack network and by the lattice preferred orientation of olivine and serpentine, at higher pressures perhaps only by the latter. Our results and the laboratory relationship be-
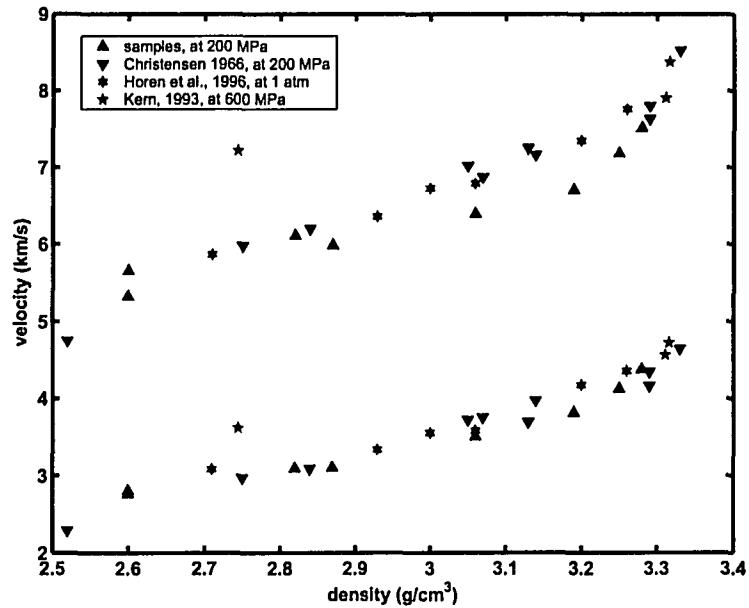
Figure 3.20: Mean velocities (top group: P-wave; bottom group: S-wave) vs. density at room temperature

tween velocity and density by different authors (*Christensen*, 1965, 1966a,b; *Kern*, 1993; *Horen et al.*, 1996) for serpentinite and peridotite are shown in Figure 3.20. Observed Vp anisotropy varied from quasi-isotropic to weakly anisotropic (Ap = 11%). The pressure invariance of the observed P-wave anisotropy and the shear-wave splitting above 100 MPa indicates that the microcracks play only a small role even at lower pressures, and that the lattice preferred orientation (LPO) is mainly responsible for the measured seismic anisotropy in these rocks.

Table 3.6: P-wave velocities at various pressures for the Pindos and Vourinos Ophiolites (Greece)

| Density $(g/cm^3)$ | Direction | \multicolumn{13}{c}{Velocity (km/s) in pressures (MPa)} | $(Vp)_0$ | $\frac{dV_p}{dp}(10^{-4})$ | $R^2$ |
| | | 0 | 25 | 50 | 75 | 100 | 125 | 150 | 175 | 200 | 225 | 250 | 275 | 300 | | | |
|---|---|---|---|---|---|---|---|---|---|---|---|---|---|---|---|---|---|
| P 03-1 | Z | 6 | 6.19 | 6.27 | 6.33 | 6.36 | 6.39 | 6.4 | 6.42 | 6.43 | 6.45 | 6.46 | 6.47 | 6.48 | 6.27 | 7 | 0.93 |
| | Y | | 6.35 | 6.75 | 6.83 | 6.87 | 6.91 | 6.94 | 6.95 | 6.97 | 6.97 | 6.99 | 7.01 | 7.01 | 7.05 | 6.83 | 7 | 0.95 |
| 3.19 | Ave. Vp | 6.18 | 6.47 | 6.55 | 6.6 | 6.64 | 6.67 | 6.68 | 6.7 | 6.7 | 6.72 | 6.74 | 6.74 | 6.77 | 6.55 | 7 | 0.94 |
| | A % | 5.67 | 8.66 | 8.55 | 8.18 | 8.29 | 8.25 | 8.24 | 8.22 | 8.06 | 8.04 | 8.17 | 8.01 | 8.43 | | | |
| P 04-2 | Z | 5.12 | 5.65 | 5.68 | 5.7 | 5.72 | 5.74 | 5.77 | 5.78 | 5.8 | 5.81 | 5.84 | 5.85 | 5.87 | 5.65 | 7 | 0.99 |
| | Y | | 5.91 | 5.96 | 6 | 6.04 | 6.07 | 6.08 | 6.11 | 6.12 | 6.15 | 6.16 | 6.17 | 6.2 | 6.21 | 5.99 | 7 | 0.99 |
| 2.87 | Ave. Vp | 5.52 | 5.81 | 5.84 | 5.87 | 5.9 | 5.91 | 5.94 | 5.95 | 5.98 | 5.99 | 6.01 | 6.03 | 6.04 | 5.82 | 7 | 0.99 |
| | A % | 14.3 | 5.34 | 5.48 | 5.79 | 5.94 | 5.75 | 5.72 | 5.71 | 5.86 | 5.85 | 5.5 | 5.81 | 5.63 | | | |
| P 08-3 | Z | 5.94 | 6.08 | 6.12 | 6.14 | 6.17 | 6.18 | 6.2 | 6.21 | 6.23 | 6.24 | 6.27 | 6.28 | 6.29 | 6.1 | 6 | 0.99 |
| | Y | | 6.23 | 6.3 | 6.36 | 6.4 | 6.44 | 6.49 | 6.51 | 6.52 | 6.55 | 6.56 | 6.57 | 6.58 | 6.58 | 6.38 | 8 | 0.91 |
| 3.06 | Ave. Vp | 6.09 | 6.19 | 6.24 | 6.27 | 6.31 | 6.34 | 6.36 | 6.37 | 6.39 | 6.4 | 6.42 | 6.43 | 6.44 | 6.24 | 7 | 0.95 |
| | A % | 4.77 | 3.55 | 3.85 | 4.15 | 4.28 | 4.89 | 4.88 | 4.87 | 5.01 | 5 | 4.67 | 4.67 | 4.51 | | | |
| P 08-4 (3.08) | Z | 6.25 | 6.33 | 6.38 | 6.41 | 6.43 | 6.45 | 6.46 | 6.48 | 6.49 | 6.51 | 6.52 | 6.53 | 6.54 | 6.37 | 6 | 0.99 |
| P 11-1 | Z | 7.27 | 7.34 | 7.37 | 7.39 | 7.39 | 7.41 | 7.43 | 7.44 | 7.45 | 7.46 | 7.47 | 7.48 | 7.49 | 7.35 | 5 | 0.98 |
| | Y | | 6.98 | 7.39 | 7.46 | 7.48 | 7.5 | 7.52 | 7.53 | 7.55 | 7.57 | 7.58 | 7.58 | 7.6 | 7.63 | 7.44 | 6 | 0.99 |
| 3.28 | Ave. Vp | 7.13 | 7.37 | 7.42 | 7.44 | 7.45 | 7.47 | 7.47 | 7.48 | 7.5 | 7.51 | 7.52 | 7.53 | 7.54 7.56 | 7.4 | 5.5 | 0.99 |
| | A % | 4.1 | 0.68 | 1.21 | 1.21 | 1.48 | 1.47 | 1.34 | 1.47 | 1.6 | 1.6 | 1.46 | 1.59 | 1.85 | | | |
| P 12-1 | Z | 6.11 | 6.4 | 6.47 | 6.58 | 6.61 | 6.61 | 6.62 | 6.7 | 6.78 | 6.77 | 6.77 | 6.77 | 6.77 | 6.51 | 1 | 0.84 |
| | Y | | 6.8 | 7.36 | 7.41 | 7.43 | 7.5 | 7.53 | 7.55 | 7.56 | 7.57 | 7.58 | 7.6 | 7.61 | 7.62 | 7.24 | 7 | 0.89 |
| 3.25 | Ave. Vp | 6.46 | 6.88 | 6.94 | 7.01 | 7.06 | 7.07 | 7.09 | 7.13 | 7.18 | 7.18 | 7.19 | 7.19 | 7.2 | 6.88 | 4 | 0.87 |
| | A % | 10.7 | 14 | 13.5 | 12.1 | 12.6 | 13 | 13.1 | 12.1 | 11 | 11.3 | 11.6 | 11.7 | 11.8 | | | |
| P 13-1 | Z | 4.85 | 5.04 | 5.07 | 5.13 | 5.16 | 5.2 | 5.23 | 5.24 | 5.27 | 5.28 | 5.29 | 5.29 | 5.29 | 5.1 | 7 | 0.91 |
| | Y | | 4.93 | 5.15 | 5.2 | 5.23 | 5.26 | 5.28 | 5.31 | 5.34 | 5.36 | 5.38 | 5.41 | 5.44 | 5.45 | 4.16 | 1 | 0.99 |
| 2.6 | Ave. Vp | 4.89 | 5.1 | 5.14 | 5.18 | 5.21 | 5.24 | 5.27 | 5.29 | 5.32 | 5.33 | 5.35 | 5.37 | 5.37 | 4.63 | 4 | 0.95 |
| | A % | 1.64 | 2.16 | 2.53 | 1.93 | 1.92 | 1.53 | 1.52 | 1.89 | 1.69 | 1.88 | 2.24 | 2.8 | 2.98 | | | |
| P 13-2 | Z | 5.45 | 5.53 | 5.56 | 5.57 | 5.58 | 5.6 | 5.62 | 5.63 | 5.63 | 5.65 | 5.65 | 5.67 | 5.68 | 5.54 | 5 | 0.99 |
| | Y | | 5.33 | 5.48 | 5.54 | 5.57 | 5.6 | 5.62 | 5.64 | 5.66 | 5.67 | 5.69 | 5.7 | 5.71 | 5.72 | 5.54 | 6 | 0.98 |
| 2.6 | Ave. Vp | 5.39 | 5.51 | 5.55 | 5.57 | 5.59 | 5.61 | 5.63 | 5.65 | 5.65 | 5.67 | 5.68 | 5.69 | 5.7 | 5.54 | 5.5 | 0.99 |
| | A % | 2.2 | 0.9 | 0.4 | 0 | 0.36 | 0.36 | 0.36 | 0.53 | 0.71 | 0.71 | 0.88 | 0.7 | 0.7 | | | |
| P 16-3 | Z | 5.71 | 5.84 | 5.91 | 5.94 | 5.97 | 5.99 | 6 | 6.02 | 6.03 | 6.05 | 6.06 | 6.07 | 6.08 | 5.91 | 6 | 0.99 |
| | Y | | 5.87 | 5.96 | 6 | 6.05 | 6.07 | 6.1 | 6.14 | 6.16 | 6.17 | 6.19 | 6.2 | 6.22 | 6.23 | 6 | 8 | 0.96 |
| 2.82 | Ave. Vp | 5.79 | 5.9 | 5.96 | 6 | 6.02 | 6.05 | 6.07 | 6.09 | 6.1 | 6.12 | 6.13 | 6.15 | 6.16 | 5.96 | 7 | 0.98 |
| | A % | 2.76 | 2.03 | 1.51 | 1.83 | 1.66 | 1.82 | 2.31 | 2.3 | 2.3 | 2.29 | 2.28 | 2.44 | 2.44 | | | |
| V 03-11 (2.99) | Z | 5.46 | 5.52 | 5.56 | 5.59 | 5.62 | 5.65 | 5.67 | 5.7 | 5.72 | 5.74 | 5.75 | 5.77 | 5.8 | 5.53 | 9 | 0.99 |
| V 03-7 (2.95) | Z | 5.31 | 5.4 | 5.43 | 5.45 | 5.47 | 5.49 | 5.51 | 5.52 | 5.54 | 5.55 | 5.58 | 5.6 | 5.62 | 5.39 | 7 | 0.99 |

Table 3.7: S-wave velocities at various pressures for the Pindos and Vourinos Ophiolites (Greece)

| Density (g/cm³) | Direction | Velocity (km/s) in pressures (MPa) | | | | | | | | | | | | | Pres. derivative | | |
|---|---|---|---|---|---|---|---|---|---|---|---|---|---|---|---|---|---|
| | | 0 | 25 | 50 | 75 | 100 | 125 | 150 | 175 | 200 | 225 | 250 | 275 | 300 | $(V_s)_0$ | $\frac{dV_s}{dp}(10^{-4})$ | $R^2$ |
| P 03-1 | ZX | 4.1 | 4.18 | 4.2 | 4.21 | 4.22 | 4.22 | 4.23 | 4.23 | 4.24 | 4.24 | 4.24 | 4.25 | 4.25 | 4.19 | 2 | 0.99 |
| | ZY | 3.65 | 3.82 | 3.88 | 3.91 | 3.92 | 3.93 | 3.94 | 3.95 | 3.95 | 3.96 | 3.96 | 3.97 | 3.97 | 3.91 | 3 | 0.94 |
| 3.19 | $\Delta Vs(Z)$ | 0.45 | 0.36 | 0.32 | 0.3 | 0.3 | 0.29 | 0.29 | 0.28 | 0.29 | 0.28 | 0.28 | 0.28 | 0.28 | 0.28 | | |
| | YX | 3.15 | 3.44 | 3.45 | 3.46 | 3.47 | 3.48 | 3.49 | 3.49 | 3.5 | 3.5 | 3.51 | 3.52 | 3.52 | 3.45 | 3 | 0.98 |
| | YZ | 3.27 | 3.86 | 3.91 | 3.93 | 3.94 | 3.95 | 3.96 | 3.97 | 3.98 | 3.98 | 3.99 | 3.98 | 4 | 3.91 | 3 | 0.94 |
| | $\Delta Vs(Y)$ | 0.12 | 0.42 | 0.46 | 0.47 | 0.47 | 0.47 | 0.47 | 0.48 | 0.48 | 0.48 | 0.48 | 0.46 | 0.48 | 0.46 | | |
| | Ave. Vs | 3.36 | 3.71 | 3.75 | 3.77 | 3.78 | 3.79 | 3.8 | 3.8 | 3.81 | 3.81 | 3.82 | 3.82 | 3.83 | 3.76 | 3 | 0.95 |
| | A % | 3.57 | 11.3 | 12.3 | 12.5 | 12.4 | 12.4 | 12.4 | 12.6 | 12.6 | 12.6 | 12.6 | 12 | 12.5 | 12.2 | | |
| P 04-2 | ZX | 3.11 | 3.16 | 3.17 | 3.19 | 3.19 | 3.2 | 3.21 | 3.22 | 3.23 | 3.23 | 3.24 | 3.25 | 3.25 | 3.17 | 3 | 0.99 |
| | ZY | 2.96 | 3.04 | 3.06 | 3.07 | 3.08 | 3.08 | 3.09 | 3.09 | 3.1 | 3.1 | 3.1 | 3.11 | 3.11 | 3.06 | 2 | 0.99 |
| 2.87 | $\Delta Vs(Z)$ | 0.15 | 0.12 | 0.11 | 0.12 | 0.11 | 0.12 | 0.12 | 0.13 | 0.13 | 0.13 | 0.14 | 0.14 | 0.14 | 0.11 | | |
| | YX | 2.94 | 3.09 | 3.11 | 3.12 | 3.13 | 3.14 | 3.14 | 3.15 | 3.15 | 3.16 | 3.16 | 3.17 | 3.17 | 3.1 | 2 | 0.99 |
| | YZ | 2.46 | 2.86 | 2.89 | 2.9 | 2.91 | 2.91 | 2.92 | 2.92 | 2.93 | 2.93 | 2.93 | 2.94 | 2.94 | 2.89 | 2 | 0.98 |
| | $\Delta Vs(Y)$ | 0.48 | 0.23 | 0.22 | 0.22 | 0.22 | 0.23 | 0.22 | 0.23 | 0.22 | 0.23 | 0.23 | 0.23 | 0.23 | 0.21 | | |
| | Ave. Vs | 2.87 | 3.04 | 3.06 | 3.07 | 3.08 | 3.08 | 3.09 | 3.1 | 3.1 | 3.11 | 3.11 | 3.12 | 3.12 | 3.06 | 2.25 | 0.99 |
| | A % | 22.7 | 9.88 | 9.16 | 9.45 | 9.1 | 9.41 | 9.39 | 9.69 | 9.67 | 9.66 | 9.98 | 9.94 | 9.94 | 9.17 | | |
| P 08-3 | ZX | 3.19 | 3.25 | 3.27 | 3.29 | 3.3 | 3.31 | 3.32 | 3.33 | 3.34 | 3.34 | 3.35 | 3.36 | 3.38 | 3.26 | 4 | 0.98 |
| | ZY | 3.4 | 3.47 | 3.49 | 3.51 | 3.52 | 3.53 | 3.54 | 3.55 | 3.56 | 3.57 | 3.57 | 3.58 | 3.58 | 3.5 | 3 | 0.98 |
| 3.06 | $\Delta Vs(Z)$ | 0.21 | 0.22 | 0.22 | 0.22 | 0.22 | 0.22 | 0.22 | 0.22 | 0.22 | 0.23 | 0.22 | 0.22 | 0.2 | 0.24 | | |
| | YX | 3.45 | 3.54 | 3.58 | 3.59 | 3.6 | 3.61 | 3.62 | 3.62 | 3.63 | 3.64 | 3.64 | 3.65 | 3.66 | 3.57 | 3 | 0.99 |
| | YZ | 3.32 | 3.39 | 3.41 | 3.42 | 3.43 | 3.44 | 3.44 | 3.45 | 3.46 | 3.46 | 3.47 | 3.48 | 3.48 | 3.4 | 3 | 0.99 |
| | $\Delta Vs(Y)$ | 0.13 | 0.15 | 0.17 | 0.17 | 0.17 | 0.17 | 0.18 | 0.17 | 0.17 | 0.18 | 0.17 | 0.17 | 0.18 | 0.17 | | |
| | Ave. Vs | 3.34 | 3.41 | 3.44 | 3.45 | 3.46 | 3.47 | 3.48 | 3.49 | 3.5 | 3.5 | 3.51 | 3.52 | 3.53 | 3.43 | 3.25 | 0.99 |
| | A % | 7.78 | 8.5 | 9.02 | 8.69 | 8.66 | 8.64 | 8.62 | 8.32 | 8.29 | 8.57 | 8.27 | 8.24 | 7.94 | 9.03 | | |
| P 08-4 | ZX | 3.51 | 3.59 | 3.61 | 3.62 | 3.63 | 3.64 | 3.64 | 3.65 | 3.66 | 3.67 | 3.68 | 3.68 | 3.69 | 3.6 | 3 | 0.99 |
| | ZY | 3.38 | 3.43 | 3.45 | 3.46 | 3.47 | 3.47 | 3.48 | 3.49 | 3.5 | 3.5 | 3.51 | 3.51 | 3.51 | 3.44 | 2 | 0.99 |
| 3.08 | $\Delta Vs(Z)$ | 0.13 | 0.16 | 0.16 | 0.16 | 0.16 | 0.17 | 0.16 | 0.16 | 0.16 | 0.17 | 0.17 | 0.17 | 0.18 | 0.16 | | |
| | Ave. Vs | 3.45 | 3.51 | 3.53 | 3.54 | 3.55 | 3.56 | 3.56 | 3.57 | 3.58 | 3.59 | 3.6 | 3.6 | 3.6 | 3.52 | 2.5 | 0.99 |
| P 11-1 | ZX | 4.15 | 4.22 | 4.25 | 4.27 | 4.28 | 4.28 | 4.28 | 4.29 | 4.29 | 4.29 | 4.3 | 4.3 | 4.3 | 4.26 | 1 | 4.15 |
| | ZY | 4.22 | 4.36 | 4.39 | 4.41 | 4.41 | 4.42 | 4.42 | 4.43 | 4.43 | 4.44 | 4.44 | 4.44 | 4.45 | 4.39 | 2 | 4.22 |
| 3.28 | $\Delta Vs(Z)$ | 0.07 | 0.14 | 0.14 | 0.14 | 0.13 | 0.14 | 0.14 | 0.14 | 0.14 | 0.15 | 0.14 | 0.14 | 0.15 | 0.13 | | |
| | YX | 4.16 | 4.43 | 4.48 | 4.51 | 4.52 | 4.53 | 4.54 | 4.54 | 4.55 | 4.55 | 4.56 | 4.57 | 4.57 | 4.49 | 3 | 0.99 |
| | YZ | 4 | 4.09 | 4.11 | 4.13 | 4.14 | 4.14 | 4.17 | 4.19 | 4.2 | 4.22 | 4.23 | 4.23 | 4.25 | 4.09 | 6 | 0.98 |
| | $\Delta Vs(Y)$ | 0.16 | 0.34 | 0.37 | 0.38 | 0.38 | 0.39 | 0.37 | 0.35 | 0.35 | 0.33 | 0.33 | 0.34 | 0.32 | 0.4 | | |
| | Ave. Vs | 4.13 | 4.28 | 4.31 | 4.33 | 4.34 | 4.34 | 4.35 | 4.36 | 4.37 | 4.38 | 4.38 | 4.39 | 4.39 | 4.31 | 3 | 0.99 |
| | A % | 3.87 | 7.95 | 8.59 | 8.78 | 8.76 | 8.98 | 8.5 | 8.02 | 8.01 | 7.54 | 7.53 | 7.75 | 7.29 | 9.29 | | |

Cont' Table 3.7

| Density (g/cm³) | Direction | Velocity (km/s) in pressures (MPa) | | | | | | | | | | | | | $(Vs)_0$ | $\frac{dVs}{dp}(10^{-4})$ | $R^2$ |
|---|---|---|---|---|---|---|---|---|---|---|---|---|---|---|---|---|---|
| | | 0 | 25 | 50 | 75 | 100 | 125 | 150 | 175 | 200 | 225 | 250 | 275 | 300 | | | |
| P 12-1 | ZX | 3.4 | 3.81 | 3.88 | 3.91 | 3.93 | 3.95 | 3.96 | 3.97 | 3.98 | 3.99 | 3.99 | 4 | 4.01 | 3.9 | 4 | 0.96 |
| | ZY | 3.56 | 3.86 | 3.93 | 3.96 | 3.99 | 4.01 | 4.02 | 4.03 | 4.04 | 4.07 | 4.08 | 4.09 | 4.1 | 3.92 | 6 | 0.98 |
| 3.25 | $\Delta Vs(Z)$ | 0.16 | 0.05 | 0.05 | 0.05 | 0.06 | 0.06 | 0.06 | 0.06 | 0.06 | 0.08 | 0.09 | 0.09 | 0.09 | 0.02 | | |
| | YX | 3.94 | 4.11 | 4.15 | 4.16 | 4.17 | 4.18 | 4.19 | 4.2 | 4.21 | 4.23 | 4.24 | 4.25 | 4.25 | 4.13 | 4 | 0.98 |
| | YZ | 3.96 | 4.12 | 4.18 | 4.2 | 4.21 | 4.23 | 4.23 | 4.24 | 4.25 | 4.25 | 4.26 | 4.26 | 4.27 | 4.18 | 3 | 0.97 |
| | $\Delta Vs(Y)$ | 0.02 | 0.01 | 0.03 | 0.04 | 0.04 | 0.05 | 0.04 | 0.04 | 0.04 | 0.02 | 0.02 | 0.01 | 0.02 | 0.05 | | |
| | Ave. Vs | 3.72 | 3.98 | 4.04 | 4.06 | 4.08 | 4.09 | 4.1 | 4.11 | 4.12 | 4.14 | 4.14 | 4.15 | 4.16 | 4.03 | 4.25 | 0.97 |
| | A % | 15.1 | 7.8 | 7.43 | 7.15 | 6.87 | 6.84 | 6.59 | 6.57 | 6.55 | 6.29 | 6.52 | 6.27 | 6.25 | 6.94 | | |
| P 13-1 | ZX | 2.54 | 2.63 | 2.65 | 2.66 | 2.67 | 2.68 | 2.68 | 2.69 | 2.69 | 2.7 | 2.71 | 2.71 | 2.72 | 2.65 | 2 | 0.99 |
| | ZY | 2.57 | 2.67 | 2.7 | 2.71 | 2.72 | 2.72 | 2.73 | 2.74 | 2.74 | 2.75 | 2.75 | 2.75 | 2.76 | 2.7 | 2 | 0.98 |
| 2.6 | $\Delta Vs(Z)$ | 0.03 | 0.04 | 0.05 | 0.05 | 0.05 | 0.04 | 0.05 | 0.05 | 0.05 | 0.05 | 0.04 | 0.04 | 0.04 | 0.05 | | |
| | YX | 2.72 | 2.83 | 2.84 | 2.86 | 2.87 | 2.87 | 2.88 | 2.88 | 2.89 | 2.89 | 2.89 | 2.9 | 2.89 | 2.85 | 2 | 0.95 |
| | YZ | 2.74 | 2.8 | 2.82 | 2.82 | 2.83 | 2.84 | 2.85 | 2.86 | 2.87 | 2.87 | 2.88 | 2.88 | 2.89 | 2.81 | 3 | 0.97 |
| | $\Delta Vs(Y)$ | 0.02 | 0.03 | 0.02 | 0.04 | 0.04 | 0.03 | 0.03 | 0.02 | 0.02 | 0.02 | 0.02 | 0.01 | 0.02 | 0 0.04 | | |
| | Ave. Vs | 2.64 | 2.73 | 2.75 | 2.76 | 2.77 | 2.78 | 2.79 | 2.79 | 2.8 | 2.8 | 2.81 | 2.81 | 2.82 | 2.75 | 2 | 0.99 |
| | A % | 6.81 | 7.32 | 6.9 | 7.24 | 7.21 | 6.84 | 7.18 | 6.8 | 7.15 | 6.78 | 6.41 | 6.76 | 6.04 | 7.27 | | |
| P 13-2 | ZX | 2.69 | 2.77 | 2.79 | 2.8 | 2.8 | 2.81 | 2.81 | 2.82 | 2.82 | 2.82 | 2.83 | 2.83 | 2.83 | 2.71 | 2 | 0.99 |
| | ZY | 2.5 | 2.55 | 2.58 | 2.59 | 2.6 | 2.6 | 2.61 | 2.61 | 2.62 | 2.62 | 2.63 | 2.63 | 2.63 | 2.58 | 2 | 0.99 |
| 2.6 | $\Delta Vs(Z)$ | 0.19 | 0.22 | 0.21 | 0.21 | 0.2 | 0.21 | 0.2 | 0.21 | 0.2 | 0.2 | 0.2 | 0.2 | 0.2 | 0.13 | | |
| | YX | 2.72 | 2.78 | 2.79 | 2.8 | 2.81 | 2.81 | 2.82 | 2.83 | 2.83 | 2.84 | 2.84 | 2.84 | 2.85 | 2.71 | 2 | 0.99 |
| | YZ | 2.7 | 2.73 | 2.74 | 2.75 | 2.76 | 2.76 | 2.77 | 2.77 | 2.77 | 2.78 | 2.78 | 2.78 | 2.79 | 2.74 | 2 | 0.99 |
| | $\Delta Vs(Y)$ | 0.02 | 0.05 | 0.05 | 0.05 | 0.05 | 0.05 | 0.05 | 0.06 | 0.06 | 0.06 | 0.06 | 0.06 | 0.06 | 0.03 | | |
| | Ave. Vs | 2.65 | 2.71 | 2.73 | 2.74 | 2.74 | 2.75 | 2.75 | 2.76 | 2.76 | 2.77 | 2.77 | 2.77 | 2.78 | 2.69 | 2 | 0.99 |
| | A % | 8.29 | 8.49 | 7.71 | 7.68 | 7.66 | 7.65 | 7.63 | 7.98 | 7.61 | 7.96 | 7.58 | 7.58 | 7.93 | 4.84 | | |
| P 16-3 | ZX | 3.02 | 3.08 | 3.09 | 3.08 | 3.09 | 3.1 | 3.1 | 3.11 | 3.11 | 3.11 | 3.11 | 3.12 | 3.12 | 3.07 | 2 | 0.96 |
| | ZY | 2.92 | 2.99 | 2.98 | 2.99 | 3 | 3 | 3.01 | 3.02 | 3.02 | 3.02 | 3.03 | 3.03 | 3.04 | 2.99 | 2 | 0.94 |
| 2.82 | $\Delta Vs(Z)$ | 0.02 | 0.09 | 0.11 | 0.09 | 0.09 | 0.1 | 0.09 | 0.09 | 0.09 | 0.09 | 0.08 | 0.09 | 0.08 | 0.08 | | |
| | YX | 2.85 | 2.95 | 2.99 | 3.01 | 3.02 | 3.03 | 3.04 | 3.04 | 3.04 | 3.05 | 3.05 | 3.06 | 3.06 | 2.98 | 2 | 0.99 |
| | YZ | 3.04 | 3.12 | 3.14 | 3.15 | 3.16 | 3.16 | 3.17 | 3.17 | 3.17 | 3.18 | 3.18 | 3.19 | 3.19 | 3.14 | 2 | 0.95 |
| | $\Delta Vs(Y)$ | 0.19 | 0.17 | 0.15 | 0.14 | 0.14 | 0.13 | 0.13 | 0.13 | 0.13 | 0.13 | 0.13 | 0.13 | 0.13 | 0.16 | | |
| | Ave. Vs | 2.96 | 3.04 | 3.05 | 3.06 | 3.07 | 3.07 | 3.08 | 3.09 | 3.09 | 3.09 | 3.09 | 3.1 | 3.1 | 3.05 | 2 | 0.97 |
| | A % | 4.06 | 4.28 | 5.25 | 5.23 | 5.22 | 5.21 | 5.19 | 4.86 | 4.86 | 5.18 | 4.85 | 5.16 | 4.83 | 4.93 | | |
| V 03-11 | ZX | 3.21 | 3.26 | 3.28 | 3.29 | 3.32 | 3.32 | 3.33 | 3.34 | 3.34 | 3.35 | 3.35 | 3.37 | 3.38 | 3.28 | 3 | 0.95 |
| | ZY | 3.18 | 3.23 | 3.25 | 3.26 | 3.27 | 3.27 | 3.28 | 3.29 | 3.3 | 3.3 | 3.31 | 3.32 | 3.32 | 3.24 | 3 | 0.99 |
| 2.99 | $\Delta Vs(Z)$ | 0.03 | 0.03 | 0.03 | 0.03 | 0.05 | 0.05 | 0.05 | 0.05 | 0.04 | 0.05 | 0.04 | 0.05 | 0.06 | 0.04 | | |
| | Ave. Vs | 3.2 | 3.25 | 3.27 | 3.28 | 3.3 | 3.3 | 3.31 | 3.32 | 3.32 | 3.33 | 3.33 | 3.35 | 3.35 | 3.26 | 3 | 0.97 |
| V 03-7 | ZX | 2.91 | 3 | 3.02 | 3.03 | 3.03 | 3.04 | 3.04 | 3.04 | 3.05 | 3.05 | 3.06 | 3.06 | 3.08 | 3 | 2 | 0.93 |
| | ZY | 3.08 | 3.13 | 3.14 | 3.16 | 3.17 | 3.17 | 3.18 | 3.18 | 3.19 | 3.19 | 3.2 | 3.21 | 3.21 | 3.14 | 2 | 0.99 |
| 2.95 | $\Delta Vs(Z)$ | 0.17 | 0.13 | 0.12 | 0.13 | 0.14 | 0.13 | 0.14 | 0.14 | 0.14 | 0.14 | 0.14 | 0.15 | 0.13 | 0.14 | | |
| | Ave. Vs | 3 | 3.07 | 3.08 | 3.1 | 3.1 | 3.11 | 3.11 | 3.11 | 3.12 | 3.12 | 3.13 | 3.14 | 3.15 | 3.07 | 2 | 0.96 |

Table 3.8: Poisson's and Vp / Vs ratio at 200 MPa

| Sample | Density $(g/cm^3)$ | $Vs_{(mean)}$ $(km/s)$ | $Vp_{(mean)}$ $(km/s)$ | Poisson's Ratio | $Vp/Vs$ Ratio | Serpentinization (%) |
|--------|--------|--------|--------|--------|--------|--------|
| P03-1 | 3.19 | 3.81 | 6.7 | 0.26 | 1.76 | 13.6 |
| P04-2 | 2.87 | 3.1 | 5.98 | 0.32 | 1.93 | 53.8 |
| P08-3 | 3.06 | 3.5 | 6.39 | 0.29 | 1.83 | 30.4 |
| P11-1 | 3.28 | 4.37 | 7.51 | 0.24 | 1.72 | 2.3 |
| P12-1 | 3.25 | 4.12 | 7.18 | 0.25 | 1.74 | 6.8 |
| P13-1 | 2.6 | 2.8 | 5.32 | 0.31 | 1.9 | 87.9 |
| P13-2 | 2.6 | 2.76 | 5.65 | 0.34 | 2.05 | 87.9 |
| P16-3 | 2.82 | 3.09 | 6.1 | 0.33 | 1.97 | 59.9 |
| V03-11 | 2.99 | 3.4 | 5.72 | 0.23 | 1.68 | 38.8 |
| V03-7 | 2.95 | 3.12 | 5.54 | 0.27 | 1.78 | 43.8 |
| P08-4 | 3.08 | 3.58 | 6.49 | 0.28 | 1.81 | 27.5 |

Table 3.9: Calculated elastic stiffnesses (GPa) for the Pindos and Vourinos Ophiolites (Greece) at 200 MPa

| Propagation Sample | XX $C_{11}$ | YY $C_{22}$ | ZZ $C_{33}$ | ZY or YZ $C_{44}$ | ZX or XZ $C_{55}$ | XY or YX $C_{66}$ | Ave. density $(g/cm^3)$ |
|--------|--------|--------|--------|--------|--------|--------|--------|
| P 03-1 | - | 155 | 132 | 50 | 57 | 39 | 3.19 |
| P 04-2 | - | 109 | 97 | 26 | 30 | 28 | 2.87 |
| P 08-3 | - | 131 | 119 | 38 | 34 | 40 | 3.06 |
| P 11-1 | - | 188 | 182 | 61 | 60 | 67 | 3.28 |
| P 12-1 | - | 186 | 149 | 56 | 51 | 58 | 3.25 |
| P 13-1 | - | 75 | 72 | 21 | 19 | 22 | 2.6 |
| P 13-2 | - | 84 | 82 | 19 | 21 | 21 | 2.6 |
| P 16-3 | - | 107 | 103 | 27 | 27 | 26 | 2.82 |
| P 08-4 | - | - | 130 | 38 | 41 | - | 3.08 |
| V 03-7 | - | - | 91 | 30 | 27 | - | 2.95 |
| V 03-11 | - | - | 98 | 33 | 33 | - | 2.99 |
| Forsterite | 328 | 200 | 235 | 66.7 | 81.3 | 80.9 | 3.22 |

Note: $C_{44}$, $C_{55}$, and $C_{66}$ calculated by average velocities

Table 3.10: Parameters of velocity anisotropy at 200 MPa

| Sample | $\beta$(%) | Density $(g/cm^3)$ | Vp (Km/s) | Ap (%) | Vs (Km/s) | As (%) | $\Delta$ Vs (km/s) |
|--------|--------|--------|--------|--------|--------|--------|--------|
| P03-1 | 13.6 | 3.19 | 6.7 | 8.06 | 3.81 | 12.6 | 0.39 |
| P04-2 | 53.8 | 2.87 | 5.98 | 5.86 | 3.1 | 9.67 | 0.18 |
| P08-3 | 30.4 | 3.06 | 6.39 | 5.01 | 3.5 | 8.29 | 0.2 |
| P11-1 | 2.3 | 3.28 | 7.51 | 1.6 | 4.37 | 8.01 | 0.25 |
| P12-1 | 6.8 | 3.25 | 7.18 | 11 | 4.12 | 6.55 | 0.05 |
| P13-1 | 87.9 | 2.6 | 5.32 | 1.69 | 2.8 | 7.15 | 0.04 |
| P13-2 | 87.8 | 2.6 | 5.65 | 0.71 | 2.76 | 7.61 | 0.13 |
| P16-3 | 59.9 | 2.82 | 6.11 | 2.3 | 3.09 | 4.86 | 0.11 |
| P 08-4 | 27.5 | 3.08 | 6.49 | | 3.58 | | 0.16 |
| V 03-7 | 43.8 | 2.95 | 5.54 | | 3.12 | | 0.14 |
| V 03-11 | 38.8 | 2.99 | 5.72 | | 3.32 | | 0.04 |

Density, Serpentine ratio $\beta$, Average Ultrasonic Velocities (Vp/Vs), Anisotropies (Ap/As), S-wave splitting

84

# Chapter 4

# Magnetic Susceptibility and AMS

## 4.1 Introduction

The variation of susceptibility with orientation is called Anisotropy of Magnetic Susceptibility (*Tarling and Hrouda*, 1993) or usually just AMS. Magnetic fabrics defined by anisotropy of magnetic susceptibility (AMS) are sensitive indicators of rock texture and strain. Magnetic fabric techniques use this characteristic to infer the petrofabric of rocks so that their origin and structural evolution can be determined. Consequently, AMS (usually, measured at low magnetic field, $\leq 1$ mT, and room temperature (*Rochette et al.*, 1992)) is a useful tool for its intrinsic petrofabric meanings. The AMS measurement procedure principally includes: 1). the collection of oriented rock samples; 2). determination of the strength of the magnetization at a number of different orientations; 3). analysis and illustration. AMS can be interpreted in terms of the net shape of the grains and the degree of their crystalline alignments, which, in turn, can be interpreted and compared to other petrofabric techniques such as Electron Back Scatter Diffraction (EBSD). Thus, it is theoretically reasonable to compare petrofabrics by magnetic anisotropy with those of other rock physical techniques such as elastic anisotropy as discussed in the previous chapter.

Making AMS measurements is rather straightforward, however, the interpretation of the measurements is not so simple. It is essential to establish the composition, the size of magnetic grains, and the physical relationships of mineral grains before attempting a geological interpretation of magnetic fabrics. Obviously, analysis of AMS plays a particular role in the studies of many branches of the earth science. For example, research of AMS in paleomagnetism revealed in the last few decades some interesting features

85

related with strain (*Borradaile*, 1988; *Rochette et al.*, 1992), and relationships between the grain shape, structural axes and magnetic axes help to understand and reconstruct the rock's framework.

A material's magnetic susceptibility $K$ is defined with $M = K \times H$, where $M$ is the induced magnetization of the material and $H$ is the inducing magnetic field. The principles and applications related to anisotropy of low field magnetic susceptibility has been reviewed by many authors (*Hrouda*, 1982; *Borradaile*, 1988; *Jackson*, 1991; *Borradaile and Henry*, 1997). The statistical process and treatment of AMS data from a set of specimens to define the mean AMS tensor is done by the tensorial mean method (*Jelinek*, 1978).

## 4.2 Theory and method of determining AMS

The study that AMS can be used for petrofabric and other branches of the earth science, on consequently comes from the contention that AMS is caused by intrinsic magnetic properties. Then, AMS arises from the magnetic fabric caused by the preferred orientation of minerals. In general, the preferred orientation of crystallographic axes controls the grain shape and determines the magnitude and direction of AMS for most minerals and rocks. The bulk susceptibility and its anisotropy represent a summation of the susceptibility of all the mineral species that are present in a sample. What follows is a brief theoretical review related with magnetic anisotropy.

### 4.2.1 Anisotropy of magnetic susceptibility

The dependence of magnetic properties on a preferred direction is called magnetic anisotropy. There are several different types of magnetic anisotropy:

- Magnetocrystalline anisotropy

- Stress anisotropy

- Shape anisotropy

Magnetocrystalline anisotropy is an intrinsic property of a material or rock that arises from the action of lattice forces on the electron-spin configuration along a specific direction termed the easy plane or the easy axis. Stress anisotropy is another effect related

---

86

to spin-orbit coupling called magnetostriction. Magnetostriction arises from the strain dependence on anisotropy constants. Shape anisotropy is due to the shape of a mineral grain. The surface charge distribution of a magnetic mineral is another source of a magnetic field. As noted earlier, this variation of susceptibility with orientation is called anisotropy of magnetic susceptibility. In reality, only a few rocks have the induced magnetization of the same strength from a symmetrically shaped specimen irrespective of the direction in which a weak field is applied. Such rock samples are magnetically isotropic. In most rock samples, the strength of the magnetization induced by a weak field of constant strength, depends on the orientation of the sample within the field. Such rocks are magnetically anisotropic. The variation of susceptibility with orientation can be described mathematically in terms of a second-rank tensor and can be visualized as a susceptibility ellipsoid (Figure 1.3). The anisotropy of magnetic susceptibility used in most published articles is usually determined from measurements of susceptibility in a weak field ($\leq 1$ mT) unless specifically stated.

The magnitude of the anisotropy depends on two factors: the anisotropy of the individual particles and the degree of their alignment. It must be emphasized that no one method of measurement is capable of resolving the contributions of these two factors. Furthermore, the shape anisotropy of a ferrimagnetic grain can differ radically depending on whether it is multi-domain or single-domain because of the markedly different hysteresis loops of such domains. Thus, extreme care is needed when attempting to interpret any magnetic anisotropy in terms of some physical process.

### 4.2.2 Mathematical Description of AMS

The aim of a mathematical description of AMS is to give a physical concept of the values measured for magnetic susceptibility, and to derive the fundamental possibilities of exterminating the anisotropy and evaluate their accuracy (*Janák*, 1965). The theory of calculation of AMS has been discussed in the past, and various authors described methods of calculating the susceptibility tensor using least squares techniques (*Granar*, 1958; *Girdler*, 1961; *Janák*, 1965; *Jelinek*, 1977; *Hanna*, 1977). Here, a general summary of past work is provided.Those readers who have been exposed to the concepts of stress and strain will see many analogies with the full description of the susceptibility. For exam-
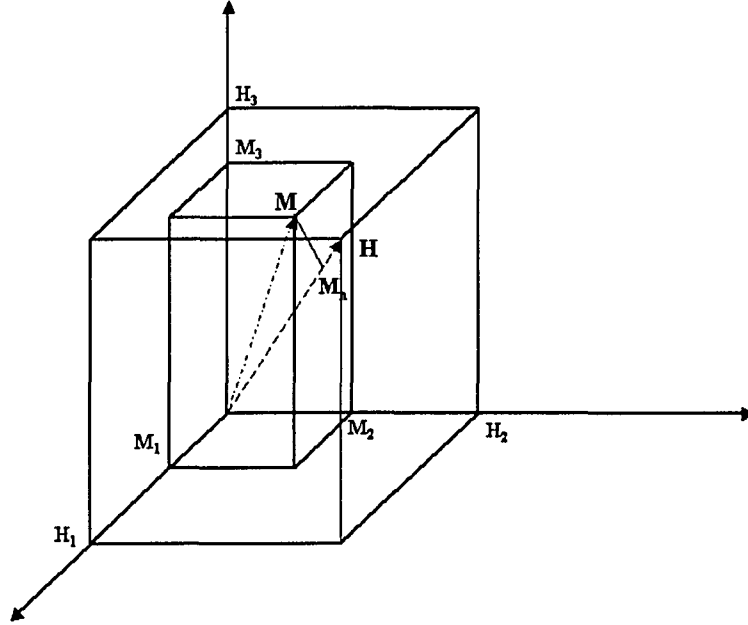
Figure 4.1: Magnetic field $H$ and Magnetization $M$

ple, as will be shown, one can use an elliptical body to represent the anisotropy of the magnetic susceptibility. Many workers have used various measures to more succinctly describe some characteristics of these elliptical bodies.

When a low field ($\leq$ 1mT) is applied to a magnetically anisotropic specimen, the magnetization, $M = M_1e_1 + M_2e_2 + M_3e_3$, is not parallel to the applied field, $H = H_1e_1 + H_2e_2 + H_3e_3$(Figure 4.1), and its three orthogonal components can be defined as:

$$M_1 = K_{11}H_1 + K_{12}H_2 + K_{13}H_3$$

$$M_2 = K_{21}H_1 + K_{22}H_2 + K_{23}H_3$$

$$M_3 = K_{31}H_1 + K_{32}H_2 + K_{33}H_3$$

(4.1)

This is equivalent to:

$$M_i = K_{ij}H_j(i, j = 1, 2, 3)$$

(4.2)

Where the $K_{ij}$ are the components of the second-order tensor which can also be expressed as a symmetric matrix:

$$K_{ij} = \begin{pmatrix} K_{11} & K_{12} & K_{13} \\ K_{12} & K_{22} & K_{23} \\ K_{31} & K_{32} & K_{33} \end{pmatrix} \tag{4.3}$$

Of these parameters, $K_{12} = K_{21}$, $K_{23} = K_{32}$, and $K_{31} = K_{13}$, so six independent components must be determined to completely define the susceptibility ellipsoid. With all such matrix tensor representations, it must be remembered that that the component values of the 'tensor' matrix of Eq. 4.3 depend on the co-ordinate frame from which the observer makes the measurements. As with stress and strain, one can also find the co-ordinate axis in which the off-diagonal components vanish leaving only those along the central diagonal. These three remaining diagonal values are called the principal values of the susceptibility $K_1$, $K_2$, and $K_3$. If the material is magnetically isotropic, the off diagonal components are equal to zero. The remaining three numbers are necessary to describe the orientation of the principal axes with respect to the original co-ordinate frame axes. The value of the susceptibility in any direction can be described by a 3-D elliptical object. The goal of making the magnetic anisotropy measurements is to obtain the 6 independent values of the susceptibility matrix of Eq.4.3, or, equivalently and more meaningfully, the three principal values and their directions with respect to the original co-ordinate frame often referenced from the textural elements of the rock.

In making a measurement, one places the sample at a variety of orientations in a uniform magnetic field H. This sample will have an induced magnetization M, but as noted M is not generally aligned with H and it is only the projection of M in the direction of the external field that is measured by the record equipment. The problem thus becomes one of making sufficiently numerous measurements of these projected magnitudes in a variety of different directions to give a series of corresponding directional susceptibilities $\kappa$ ; and then back-calculating from these observations to obtain the full susceptibility tensor of Eq. 4.3. Of concern when choosing the directions, is to keep the calculation of the susceptibility simple, the chosen direction easily realizable, and the measurements accurate. In this study, a suitable system (Bartington MS2B sensor) makes measurements in 18 different orientations shown in Figure 4.2(9 arrows and their opposite directions).
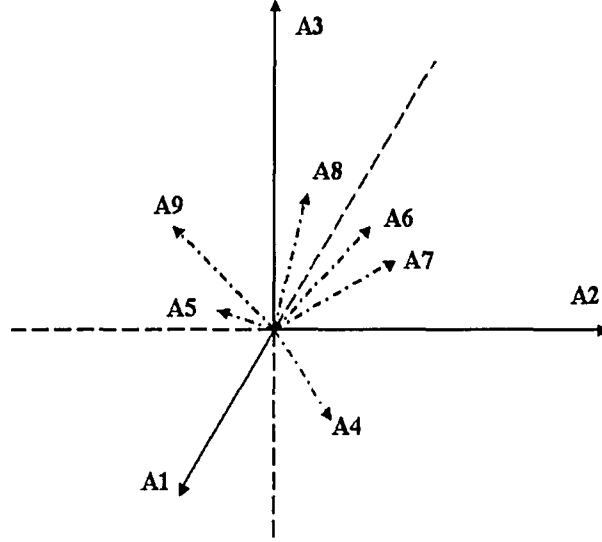
Figure 4.2: Directions $A_1...A_9$ of AMS measurements(Modified from Girdler, 1961; Janák, 1965).

The anisotropy tensor contains 6 unknown coefficients and therefore a system of six independent measurements is enough for a determination. After we determine the values of the directional susceptibilities $\kappa_1...\kappa_9$, $K_{ij}$ can be measured and calculated from the directional susceptibilities $\kappa_1...\kappa_9$. For instance, the value $\kappa_4, \kappa_5, \kappa_6$ for $K_{ij}(i \neq j)$:

$$
\begin{pmatrix} K_{23} \\ K_{13} \\ K_{12} \end{pmatrix} = \begin{pmatrix} 0 & -1/2 & -1/2 & -1 & 0 & 0 \\ -1/2 & 0 & -1/2 & 0 & 1 & 0 \\ -1/2 & -1/2 & 0 & 0 & 0 & 1 \end{pmatrix} \begin{pmatrix} \kappa_1 \\ \kappa_2 \\ \kappa_3 \\ \kappa_4 \\ \kappa_5 \\ \kappa_6 \end{pmatrix} \tag{4.4}
$$

Similarly. use the values of $\kappa_7, \kappa_8, \kappa_9$ for $K_{ij}(i \neq j)$:

$$
\begin{pmatrix} K_{23} \\ K_{13} \\ K_{12} \end{pmatrix} = \begin{pmatrix} 0 & 1/2 & 1/2 & -1 & 0 & 0 \\ 1/2 & 0 & 1/2 & 0 & -1 & 0 \\ 1/2 & 1/2 & 0 & 0 & 0 & -1 \end{pmatrix} \begin{pmatrix} \kappa_1 \\ \kappa_2 \\ \kappa_3 \\ \kappa_7 \\ \kappa_8 \\ \kappa_9 \end{pmatrix} \tag{4.5}
$$

By using a least square solution, it is possible to obtain an estimate of the best fit of the susceptibility-ellipsoid and hence for the magnitude and direction of the principal axes. The reader is referred to *Girdler* (1961); *Janák* (1965) for the complete set of details. The final equation giving the six coefficients $K_{ij}$ is:

$$
\begin{pmatrix} K_{11} \\ K_{22} \\ K_{33} \\ K_{23} \\ K_{31} \\ K_{12} \end{pmatrix} = \frac{1}{18} \begin{pmatrix} 10 & -2 & -2 & 4 & 4 & -2 & 4 & 4 & 2 \\ -2 & 10 & -2 & 4 & -2 & 4 & 4 & -2 & 4 \\ -2 & -2 & 10 & -2 & 4 & 4 & -2 & 4 & 4 \\ 0 & 0 & 0 & 0 & 0 & 9 & 0 & 0 & -9 \\ 0 & 0 & 0 & 0 & 9 & 0 & 0 & -9 & 0 \\ 0 & 0 & 0 & 9 & 0 & 0 & -9 & 0 & 0 \end{pmatrix} \begin{pmatrix} \kappa_1 \\ \kappa_2 \\ \kappa_3 \\ \kappa_4 \\ \kappa_5 \\ \kappa_6 \\ \kappa_7 \\ \kappa_8 \\ \kappa_9 \end{pmatrix} \qquad (4.6)
$$

The directions of principal axes can be calculated by:

$$
\tan \theta = \frac{n_2}{n_1} \qquad (4.7)
$$

$$
\sin \phi = n_3 \qquad (4.8)
$$

Where $n_i$ are the directional cosines of the principal axis, the directional cosines are then converted to the $(\theta, \phi)$ notation where $\theta$ is the angle of declination in degrees measured clockwise from $OA_1$ and $\phi$ is the angle of inclination with reference to the $A_1 - A_2$ plane. According to *Janák* (1965), the average deviation of such coefficients is less than 1 %.

### 4.2.3 AMS calculation and illustration

A wide range of parameters have been used in the literature describing the applications of AMS to both magnetic properties and petrofabrics. This short summary is intended to provide explanations for the parameters used in this study.

The anisotropy of low-field magnetic susceptibility ($AMS$) is usually determined after measuring the susceptibility of a rock specimen along different directions. This enables one to calculate the AMS tensor, which can be represented by an ellipsoid with minimum ($K_3$), intermediate ($K_2$) and maximum ($K_1$) susceptibility axes: $K_1 \geq K_2 \geq K_3$. The mean susceptibility is represented by: K = (K1 + K2 + K3)/3.

The ratios of the pairs of the principal susceptibilities are commonly used to characterize the magnetic fabric. Numerous parameters have been defined both for the quantification of the magnitude of anisotropy and for defining the shape of the ellipsoid. The parameters can usually be divided into two main groups: 1). those dealing with the magnitude and shape of the susceptibility ellipsoid; 2). those concerned with the spatial orientation of the principal axes of the ellipsoid.

The anisotropy degree parameter for the magnitude of anisotropy is particularly sensitive to variation in the total susceptibility, which is defined as the ratio of the maximum and minimum susceptibilities (*Nagata*, 1961):

$$P = K_1/K_3$$

*Owens* (1974) proposed another parameter for magnitude of anisotropy - the normalized anisotropy degree:

$$S = (K_1 - K_3)/K_{mean}$$

Currently, the rock-magnetic literature strongly recommends that a corrected anisotropy degree should be adopted; proposed by *Jelinek* (1981):

$$P_J = exp\sqrt{\{2[(\eta_1 - \eta_m)^2 + (\eta_2 - \eta_m)^2 + (\eta_3 - \eta_m)^2]\}}$$

Where $\eta_1 = lnK_1; \eta_2 = lnK_2; \eta_3 = lnK_3; \eta_m = (\eta_1 + \eta_2 + \eta_3)/3$. The parameter $P_J$ incorporates both the intermediate and mean susceptibility rather than only the maximum and minimum values, thus, it is a more informative parameter than $P$ alone. Also, it is better to expresses magnetic properties by using logarithmic values of susceptibility.

The shape of the anisotropy ellipsoid can be expressed in terms of the ratios or differences of the axial values. Most early parameters were based on ratios.

For example, lineation (*Balsey and Buddington*, 1960):

$$P_1 = L = K_1/K_2$$

and foliation (*Stacey*, 1960):

$$P_3 = F = K_2/K_3$$

In our study, we use the parameter $T$ for the shape ellipsoid. $T$ combines lineation and foliation parameters, and includes all three principal susceptibilities in its calculation. The magnetic literatures recommended that this shape parameter should be adopted (Jelinek, 1981; Hrouda, 1982). $T$ can be expressed as:

$$T = \left[\frac{2ln(K_2/K_3)}{ln(K_1/K_3)}\right] - 1$$

$0 < T \leq 1$ corresponds to oblate (disk) shapes ; $-1 \leq T < 0$ corresponds to prolate (rod) shapes; $T = 0$ corresponds to the shape of neutral (plane-strain) ellipsoid ($P_J = P$).

## 4.3 Magnetic susceptibility measurement

There are different methods that can to be used measure magnetic anisotropy with each method providing information that enables the anisotropy of magnetic susceptibility to be described in terms of a triaxial ellipsoid. Borradaile and Stupavsky (1995) generally summarized and reviewed measurement schemes. Jelinek (1977) used the 15-position scheme. In our lab, AMS measurements are made using a 18-position system, Bartington MS2B sensor, with AMSWIN-BAR software.

The sampling method for AMS is the same as used to collect oriented rock for paleomagnetic analysis (Cox and Doell, 1960; Collison, 1983; Tarling, 1983; Tarling and Hrouda, 1993). All such methods compromise between (i) the need for speed and accuracy during orientation and collection under field conditions and (ii) the size and shape of specimens required for the different instruments. Most of the instruments used to measure anisotropy are designed for specimens of specific sizes and shapes, these are usually identical to those required for the measurement of paleomagnetic properties (Collison, 1983; Tarling, 1983). Cylinders and cubes are normally used. The two most common standard shapes are cylinders with a diameter of 2.5 cm and a height of 2.1 cm and cubes of 2.0 cm per side (Figure 4.3). In this study, we use 2.54 cm (1-inch) length × 2.54 cm diameter core required by the operation manual from Bartington. After the velocity anisotropy measurements, the same cores were shortened and flattened as 2.54 cm diameter × 2.54 cm length cylinder core for AMS measurement.

The frequency dependence of susceptibility should be considered when making AMS measurements. Changing frequency means changing the time of reaction of grains in an
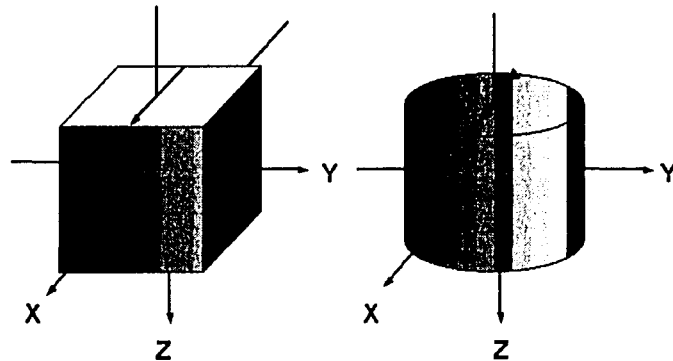
Figure 4.3: Standard specimens for AMS measurement

applied field. That is, the domain sizes will shift to larger or bigger volumes based on the variance of frequency. Experimental results show that more grains become blocked when the frequency of measurement increases (*Dunlop and Özdemir*, 1997). In this study, AMS was measured at a fixed frequency of 0.465 kHz (LF), with an applied field of 250 $\mu T$. The three principal axes defining the AMS ellipsoid are determined from the 18-position orientation scheme.

## 4.4 Results and discussion

As noted, AMS is measured in 18 different directions in our procedure, and all differences are illustrated and analyzed. AMS can be fundamentally interpreted in terms of the net shape of the grains of major phase and the degree of their crystalline alignment, which, in turn, can be compared and interpreted in the same way as in all other petrofabric techniques. AMS results for the 8 samples from the Pindos and Vourinos Ophiolites are presented in Table 4.1. All values of magnetic susceptibility were measured at low field and room temperature.

94

Table 4.1: The AMS measurement of the Pindos and Vourinos Ophiolites (Greece)

| Sample | | Declination (degree) | Inclination (degree) | Eigenvalue (degree) | Susceptibility (mean, $10^{-5}SI$) | Anisotropy (%) | Serpentinization $\beta$ (%) |
|---|---|---|---|---|---|---|---|
| P 12-1 | $K_{min}$ | 346.9 | 72.4 | 46.7 | 50.9 | 13.7 | 6.8 |
| | $K_{int}$ | 139.4 | 15.7 | 52.4 | | | |
| | $K_{max}$ | 231.5 | 7.8 | 53.7 | | | |
| P 03-1 | $K_{min}$ | 3.4 | 83.2 | 90.2 | 101.9 | 18.9 | 13.6 |
| | $K_{int}$ | 222.1 | 5.3 | 106.1 | | | |
| | $K_{max}$ | 131.7 | 4.2 | 109.5 | | | |
| P 08-3 | $K_{min}$ | 307 | 50.9 | 291.3 | 302.3 | 7 | 30.4 |
| | $K_{int}$ | 115.3 | 38.5 | 303 | | | |
| | $K_{max}$ | 209.9 | 5.8 | 312.6 | | | |
| P 13-1 | $K_{min}$ | 4.3 | 64.3 | 291.1 | 317.8 | 15.1 | 87.9 |
| | $K_{int}$ | 223 | 20.6 | 323.2 | | | |
| | $K_{max}$ | 127.4 | 14.7 | 339.1 | | | |
| P 13-2 | $K_{min}$ | 51.4 | 69 | 307.5 | 330.7 | 14.8 | 87.9 |
| | $K_{int}$ | 215.3 | 20.3 | 328.1 | | | |
| | $K_{max}$ | 307.3 | 5.4 | 356.5 | | | |
| P 11-1 | $K_{min}$ | 6.1 | 81.1 | 117.2 | 126.1 | 13.9 | 2.3 |
| | $K_{int}$ | 96.2 | 0 | 126.3 | | | |
| | $K_{max}$ | 186 | 8.9 | 134.7 | | | |
| P 04-2 | $K_{min}$ | 126.6 | 86.1 | 92.4 | 99 | 10.9 | 53.8 |
| | $K_{int}$ | 16.5 | 1.3 | 101.5 | | | |
| | $K_{max}$ | 286.5 | 3.7 | 103.2 | | | |
| P 16-3 | $K_{min}$ | 212.4 | 58.8 | 29.8 | 444.8 | 219.2 | 59.9 |
| | $K_{int}$ | 82.2 | 21.3 | 299.8 | | | |
| | $K_{max}$ | 343.3 | 21.6 | 1004.7 | | | |

The mean magnetic susceptibility, $K_m = (K_1 + K_2 + K_3)/3$, of the Pindos and Vourinos Ophiolites, varies from 50.9 $\times 10^{-5}$ to 444.8 $\times 10^{-5}$ SI with an overall average magnetic susceptibility of $221.7 \times 10^{-5}$ SI. The highest value is obtained from sample P 16-3, the serpentinized dunite, due to the presence of abundant magnetite presumably generated during serpentinization process. Therefore, the magnetic fabrics in this sample are mainly produced by magnetite grains as was indicated in the magnetic characterizations of Chapter 2. The lowest value comes from sample P 12-1, dunite, and is primarily due to the presence of paramagnetic mineral olivine. The values observed here are consistent with the wide range of susceptibilities from 3.1 $\times 10^{-3}$ to 18 $\times 10^{-3}$ SI (*Blum*, 1997) for serpentinized peridotite, and do not significantly depart from the value of *Toft et al.* (1990). Hence, in the samples from the Pindos and Vourinos Ophiolite, contribution from both the paramagnetic and ferrimagnetic minerals has to be taken into account when

magnetite is present from the process of serpentinization.

Magnetic anisotropy will be greatly influenced by a samples' composition as indicated by our results. The smallest value of AMS ($(K_1 - K_3)/K_{mean}$) among all samples is 7% for sample P 08-3. The largest AMS value comes from sample P16-3 at 219.2% with an average magnetic susceptibility of 444.8 $\times 10^{-5}$ SI, which definitely implies the existence of ferrimagnetic minerals.

The magnitude and direction of all the sample's principal axes are shown in Figure 4.4. The maximum and intermediate axes have no particular declination trend; this is not unexpected as there is no information on the orientation of their original geographic position. The inclination, however, is almost entirely near the edge of the polar plot. This suggests that the orientation of the sampling was closely perpendicular to foliation. The minimum $K$ axis shows a non-random distribution with its axis clustering in a direction perpendicular to the textural planes (that is, the direction of the Z-axis in seismic anisotropy, which is perpendicular to the cutting plane with 90 degree inclination, as seen in Figure 4.4). Samples P 08-3 and P 16-3 deviate from this trend; due to the fact that the textures were not easily discernable in these two rocks. Their sampling orientation was neither parallel nor perpendicular to the foliation.

Three typical ellipsoids are shown in Figure 4.5. The AMS degree of P 03-1 is largest among these three samples. Describing the specific relationship between the magnetic axes of rock-forming minerals and their shape and crystallographic axes, the usual relationship between AMS and petrofabric, leads to the expression 'normal magnetic fabric'. A normal magnetic fabric corresponds to the situation where $K_1$ is parallel to the structural lineation (due to stretching, flow or current origin) and where $K_3$ is perpendicular to the structural foliation (flattening, flow or bedding plane). Magnetic fabric and rock texture are quite similar; that is, the symmetry of the AMS ellipsoid mimics the petrofabric symmetry. Here, normal magnetic fabric exists in this study. Comparison between magnetic fabric and rock fabric is made in samples P 03-1 and P 13-1, for example, by contrasting magnetic fabric with rock fabric as observed visually in the rock and in thin section. As shown in Figure 4.5, samples P 03-1 and P 13-1 are classified as 'normal' since the inclination of their Kmin axis is nearly perpendicular at $3.4^0$ and $4.3^0$, respectively. The plane consisting of Kmax and Kint compare favorably with rock foliation. In
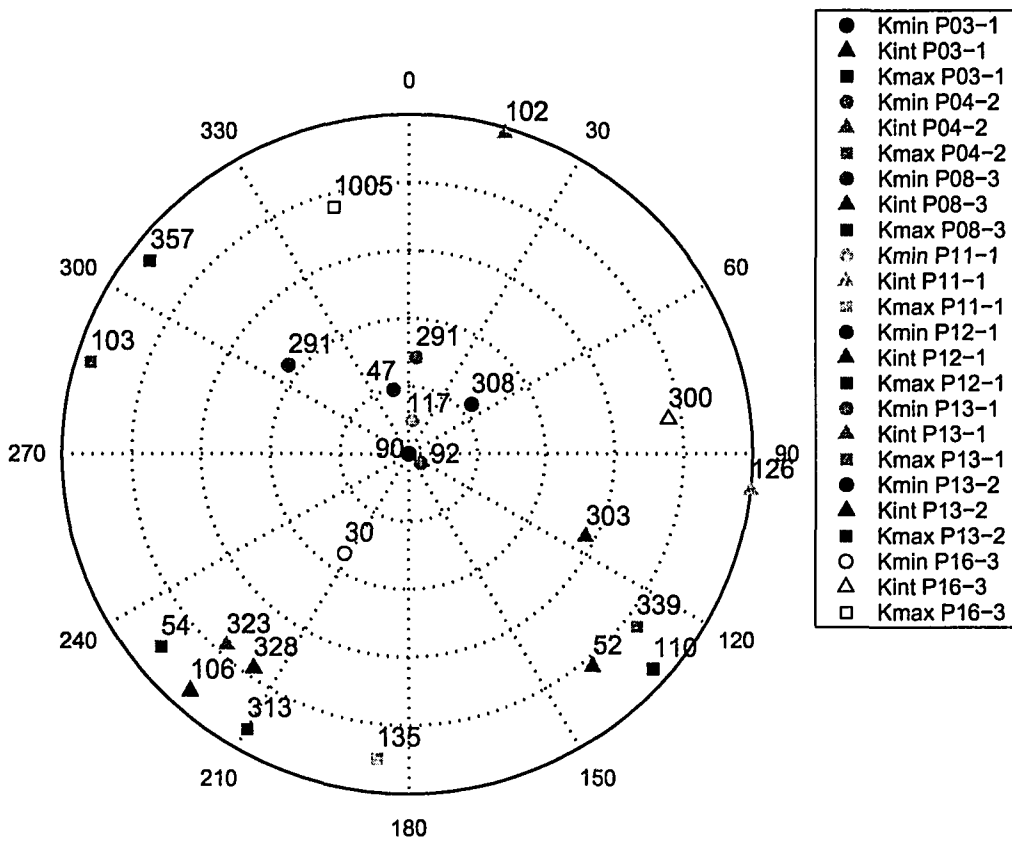
Figure 4.4: The magnitude and direction of all samples' principal axes; projected in lower hemisphere. (Declination: $0^o$ to $360^o$ clockwise; Inclination: $0^o$ to $90^o$ from edge to center)

97

the case of sample P 08-3, where the sampling orientation is not perpendicular to foliation, the principal axes of AMS immediately show its difference comparing with other samples (in case of Z-direction sampling, neither are $K_1$ and $K_2$ perpendicular to the sampling direction, nor is $K_3$ parallel to it), which conversely imply that AMS is a useful indication in rock texture.

The anisotropy degree of AMS as indicated by lineation ($P1$) and foliation ($P3$) is shown in Figure 4.6, with data values shown in Table 4.2. Although there is no clear relationship between $P1$ and $P3$, the result still shows that most samples are below the slope of unit gradient $P_1/P_3 = 1$. That means most are oblate except for P 13-2 (prolate fabrics i.e. above the slope).

The strength and shape of AMS ellipsoid have been expressed using Jelinek's parameters ($T$ and $P_J$) in Figure 4.7, with data values shown in Table 4.2. The figures show that most magnetic susceptibility ellipsoids are oblate for the samples from Pindos and Vourinos Ophiolite. All $P_J$ values vary from 1.03 to 4.72, (average 1.52). The $P_J$ values of all the other samples lie between 1.03 and 1.1 except for P 16-3. That means all samples have weakly magnetic anisotropy except for P 16-3. As illustrated by the distribution of the data, $T$ ranges from -0.12 to 0.7, (average 0.35). All other samples' $T$ values are above the $T = 0$ in the $T - P_J$ graph (Figure 4.7), which means that all others are oblate ($0 < T < 1$) except for P 13-2 ($-1 < T < 0$). The values of P 11-1 and P 08-3 are very small, 0.075 and 0.116, respectively. So, they could be classified as neutral ellipsoids (plot close to $T = 0$).

## 4.5 Conclusion

AMS describes the variation of magnetic susceptibility with direction in a material, and represents the contributions of all rock forming minerals (i.e., dia-, para-, ferri-, and ferromagnetic). Since both paramagnetic and ferrimagnetic minerals are present in this study, the bulk AMS reflects the combination of the anisotropy from the preferred crystallographic orientations of paramagnetic minerals, and the anisotropy of magnetite grains. Normally, $K_{max}$ axis represents the magnetic lineation while $K_{min}$ is the pole of the magnetic foliation (the plane containing $K_{max}$ and $K_{int}$ axes).

(a) P03-1

(b) P03-1

(c) P13-1

(d) P13-1

(e) P08-3

(f) P08-3
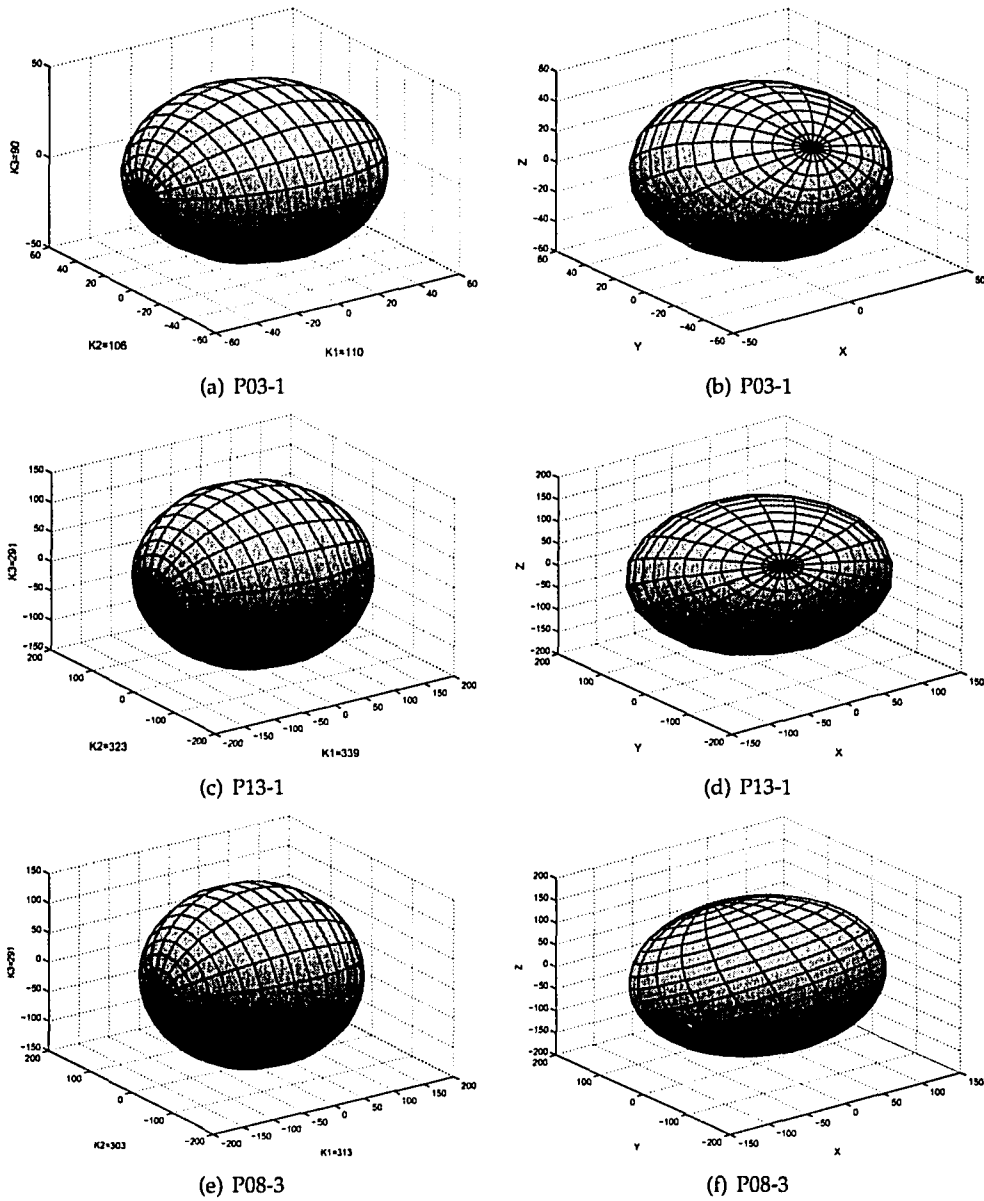
Figure 4.5: The typical ellipsoids of samples P 03-1, P13-1, P08-3; To the left: in coordinates of principal axes of AMS, where Z is parallel to $K_3$. To the Right: in coordinates of reality, where Z is perpendicular to top of the core. The plot is by 3-D visualization, real $K$ values listed in Table 4.1
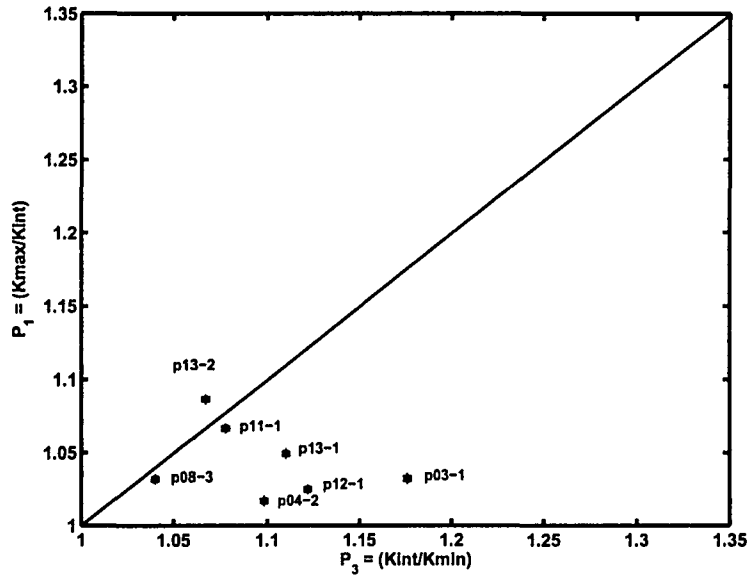
Figure 4.6: Plot of Lineation ($P1$) vs. Foliation ($P3$)
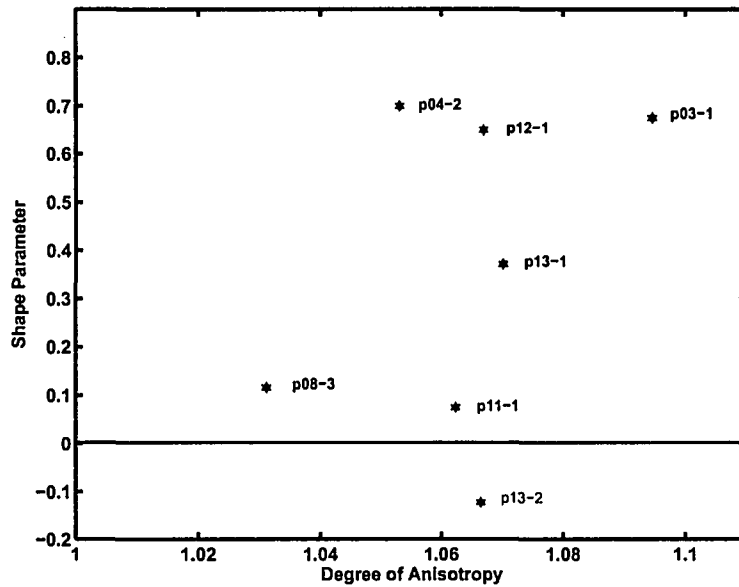


Figure 4.7: Plot of corrected anisotropy degree ($P_J$) with shape parameter ($T$)

100

Table 4.2: Parameters of describing AMS ellipsoid (Parameters defined in 3.3.3)

| Sample | $K_{mean}$ $(10^{-5}SI)$ | Anisotropy (%) | Density $(g/cm^3)$ | $P_J$ | T | Foliation $(K_2/K_3)$ | Lineation $(K_1/K_2)$ | $\beta$ (%) |
|---|---|---|---|---|---|---|---|---|
| P 13-1 | 317.8 | 15.1 | 2.6 | 1.07 | 0.371 | 1.11 | 1.049 | 87.9 |
| P 13-2 | 330.7 | 14.8 | 2.6 | 1.067 | -0.123 | 1.067 | 1.087 | 87.9 |
| P 04-2 | 99 | 10.9 | 2.87 | 1.053 | 0.7 | 1.099 | 1.017 | 53.8 |
| P 08-3 | 302.3 | 7 | 3.06 | 1.031 | 0.116 | 1.04 | 1.032 | 30.4 |
| P 03-1 | 101.9 | 18.9 | 3.19 | 1.095 | 0.675 | 1.176 | 1.032 | 13.6 |
| P 11-1 | 126.1 | 13.9 | 3.28 | 1.062 | 0.075 | 1.078 | 1.067 | 2.3 |
| P 12-1 | 50.9 | 13.7 | 3.25 | 1.067 | 0.649 | 1.122 | 1.049 | 6.8 |
| P 16-3 | 444.8 | 219.2 | 2.82 | 4.723 | 0.313 | 10.06 | 3.351 | 59.9 |
| Average | 221.7 | 39.2 | 2.96 | 1.521 | 0.347 | 2.219 | 1.336 | 42.8 |

Noted: $\beta$ : Serpentinization ratio

Table 4.2 lists the AMS ellipsoid parameters. In general, the variation of the samples' bulk susceptibility is related to their percentage of serpentinization. Samples with a lower density generally have a higher susceptibility, although sample P 08-3 does not fit this trend. A plot of the degree of lineation and foliation (Figure 4.6) and a Jelinek's parameters $T - P_J$ graph (Figure 4.7) show that the magnetic susceptibility ellipsoids are mostly oblate in the samples. The $P_J$ value suggests that the AMS of all the samples, except for P 16-3, are weakly anisotropic. The variation of AMS degree depends on composition and category of samples, usually between 10 to 20 percent. Sample P 16-3 has the largest magnetic susceptibility, probably because of the heterogeneity of magnetite distribution. Very often the accumulation of magnetic minerals can dominate the entire susceptibility signal, even though all minerals contribute to the overall bulk susceptibility.

# Chapter 5

# Comparison between seismic anisotropy and AMS

## 5.1 Introduction

Both magnetic fabric and elastic anisotropy measurements were performed on 8 samples of the Pindos and Vourinos ophiolite (Greece). AMS (anisotropy of magnetic susceptibility) and seismic anisotropy are two external manifestations of the intrinsic physical properties of these samples. The correlation between the AMS fabric and rock fabric has been widely discussed (e.g. *Hrouda*, 1982; *Borradaile and Henry*, 1997; *Rochette et al.*, 1992; *Yaouancq and Macleod*, 2000; *Bascou et al.*, 2002; *Ferré et al.*, 2005); as has been the correlation between seismic anisotropy and rock fabric (e.g. *Mainprice and Silver*, 1993; *Ji and Salisbury*, 1993a; *Ji et al.*, 1993b; *Barruol and Kern*, 1996; *Kern et al.*, 1996; *Dewandel et al.*, 2003). Measurements and theory of the seismic anisotropy and AMS have been reviewed and discussed in the chapter 2 and 3, respectively. This chapter will largely focus on a comparison of the magnetic anisotropy to the elastic anisotropy based on these laboratory results.

## 5.2 Controlling factors of magnetic anisotropy

Serpentinization is a simple and widespread hydrothermal alteration process, which produces serpentine group minerals, brucite, and magnetite (*Best*, 2003). Serpentine replace the olivine grains by hydration reaction along cracks; progressive serpentinization create serpentine-filled fractures and form a grid-pattern on the block of peridotite (e.g. Figure

102

Figure 5.1: Degree of serpentinization vs. mean magnetic susceptibility (log scale); Data from this study and that of *Toft et al.* (1990)

A.7 and A.8). During the serpentinization, ferrous iron reacts with oxygen and forms magnetite (*Best*, 2003). Usually, magnetite occur as the accessory phases. Because the ferrimagnetic minerals have positive and large susceptibilities compared to the para- and diamagnetic minerals, magnetite generated from olivine and pyroxene during the reaction of serpentinization will enhance the magnetic susceptibility of the whole rock assemblage. Hence, serpentinized rock may have high magnetic susceptibilities compared both with protoliths and with typical crustal rocks (*Toft et al.*, 1990). The variation of magnetic susceptibility with serpentinization is plotted in Figure 5.1, and shows a general linear increase of susceptibility with an increase in serpentization. The increase on susceptibility is likely due to the production of magnetite during the serpentization process.

## 5.3 Seismic anisotropy influenced by serpentinization

The influence to seismic anisotropy by serpentinization has been described in depth in chapter 2. The intrinsic seismic anisotropy is controlled by the mineral fabric preferred orientation. In general, an increasing degree of serpentinization results in a decrease in P-

103

and S-wave velocities, in the percentage of P- and S-wave anisotropy, and in shear wave splitting. In the samples from the Pindos and Vourinos ophiolite (Greece), olivine relicts are surrounded by serpentine in partially serpentinized dunite (e.g. see thin sections A.7 and A.8 in Appendix A). The experimental measurements in Chapter 2 also showed that seismic anisotropy decreases with an increase of serpentinization in peridotites in a manner similar to *Christensen* (1966b) and *Horen et al.* (1996).

As stated in Chapter 1 and whole rock analysis in Chapter 2, we have assumed that the degree of serpentinization of our rock samples can be estimated by mass density measurements in accordance with geology observations, using the linear relationship between density and serpentinization established by *Christensen* (1966b). The variations in velocity with changes in degree of serpentinization from our laboratory and those by *Christensen* (1966b) are plotted in Figure 5.2. A clear inverse relationship between Vp and Vs with degree of serpentization is evident. The macroscopic velocity anisotropy of P- and S-wave velocities is attributed to the controlling of olivine in peridotite and to lattice preferred orientation (LPO) in the serpentinite (*Kern*, 1993; *Barruol and Kern*, 1996; *Dewandel et al.*, 2003). According to *Weiss et al.* (1999), orthopyroxene texture is less pronounced in exhibiting a preferred orientation than olivine.

Our laboratory data indicates that most microcracks are closed below confining pressure of 100 MPa or even less. Above this pressure the wave velocities and anisotropies are mainly controlled by preferred orientation of the mineral. Compared to previous research (e.g. *Kern*, 1993; *Dewandel et al.*, 2003) and with knowledge of the constituent minerals for these samples, the anisotropy by LPO of olivine may play an important role at confining pressures above 100 MPa.

Along the direction perpendicular to rock foliation, the P-wave velocities are lowest in the measurements. The serpentine network seems quite regular and homogeneous. The decrease of seismic anisotropy with the degree of serpentinization shows that the bulk anisotropy of these rocks primarily results from preferred olivine orientation and not to the serpentine. The microcracks may also play a role in this, but the relatively uniform values observed at pressures in excess of 50 MPa suggests that this role at best is minor.
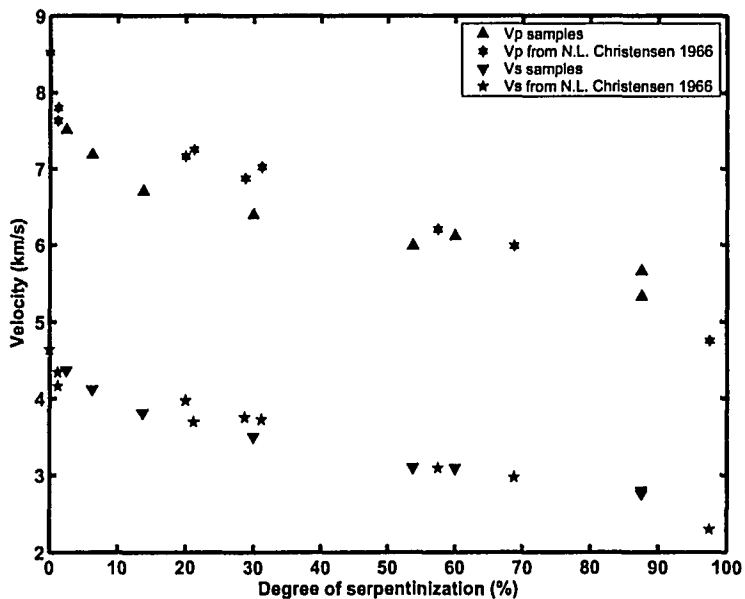
Figure 5.2: Variation of mean velocities (at 200 MPa) vs. Degree of serpentinization
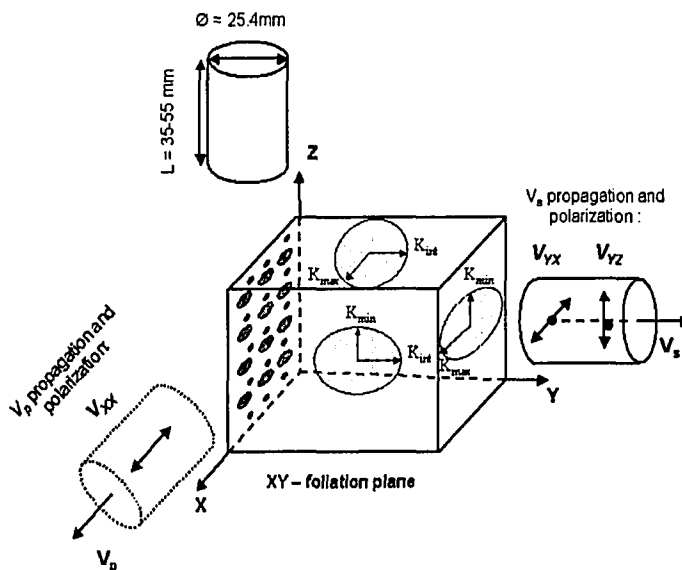


Figure 5.3: Schematic comparison between magnetic fabric and rock texture

105

## 5.4 Comparison between magnetic fabric and seismic anisotropy

A comparison of the orientation and intensity of seismic and magnetic anisotropy was carried out to determine if a correlation exists between magnetic fabric and seismic anisotropy. Using information from Figure 4.4, the AMS fabric orientation is displayed in Figure 5.4 and 5.5 and compared with laboratory slow or fast Vp directions for each sample. All samples show a coincidence between the direction of slow P-wave and $K_{min}$ except P 08-3 and P 16-3 with sampling orientation non-perpendicular to foliation, which prove a coincidence of direction between magnetic fabric and seismic anisotropy. Figure 4.4 suggest that 75 percent of the $K_{min}$ axes of the samples have an inclination of more than 64 degrees, which means the $K_{min}$ axes of most samples cluster in a direction roughly perpendicular to the rock's principal foliation; where the direction of foliation is determined on the basis of visual examination. The magnetic fabric of the samples is distributed into two groups with the following characteristics:

- Normal magnetic fabrics in which $K_{min}$ is nearly perpendicular to the rock foliation plane and is roughly parallel to the Z-axis of velocity measurement;

- Scattered magnetic fabrics (P16-3 and P08-3) for which there is no coincidence between the $K_{min}$ axis of the susceptibility ellipsoid and the Z-axis of velocity measurement;

Approximately 72 percent of the $K_{max}$ and $K_{int}$ axes of samples have inclinations less than 20 degrees. That means there is a reasonable correlation between the plane consisting of $K_{max}$ and $K_{int}$, and the principle rock texture foliation that causes seismic anisotropy. An ideal case of correspondence between magnetic fabric, seismic propagation and rock texture is shown in Figure 5.3. There is a random declination distribution of the AMS axes (Table 4.1 and Figure 4.4). No correlation can be done by comparing $K_{max}$ with the lineation of rock samples, the reason is because there was no geographic orientation of samples related with rock lineation in the field when they were obtained.

The direction of the rock's microcrack distributions may have a direct relationship with the crystal structure of the minerals. The orientations of the olivine microcrack networks are therefore related to the whole rock fabrics. From Figure 5.6, we see the

---

106

(a) P03-1

(b) P04-2

(c) P08-3

(d) P11-1
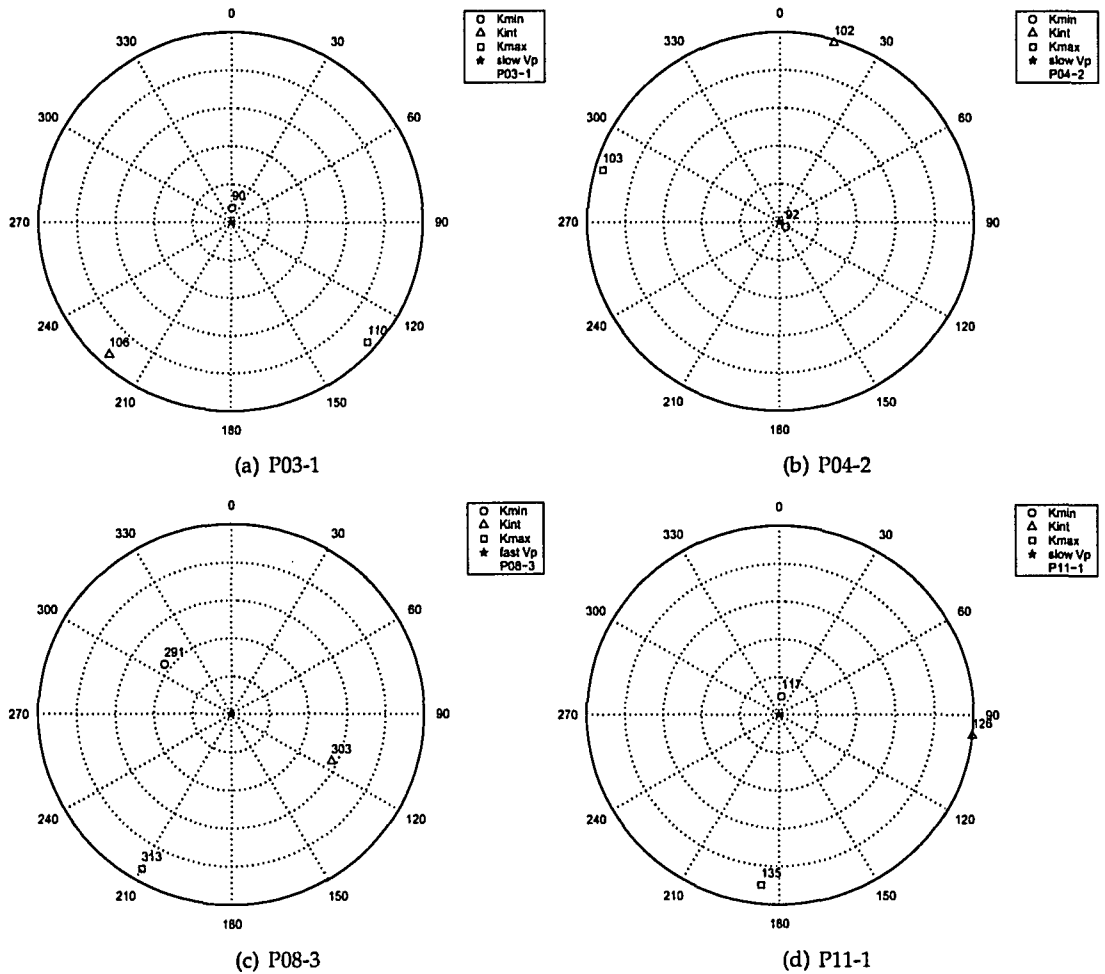
Figure 5.4: AMS Minimum, intermediate, and maximum susceptibility axes of samples. The number near the symbols is magnetic susceptibility of each axis.

107

(a) P12-1

(b) P13-1

(c) P13-2

(d) P16-3
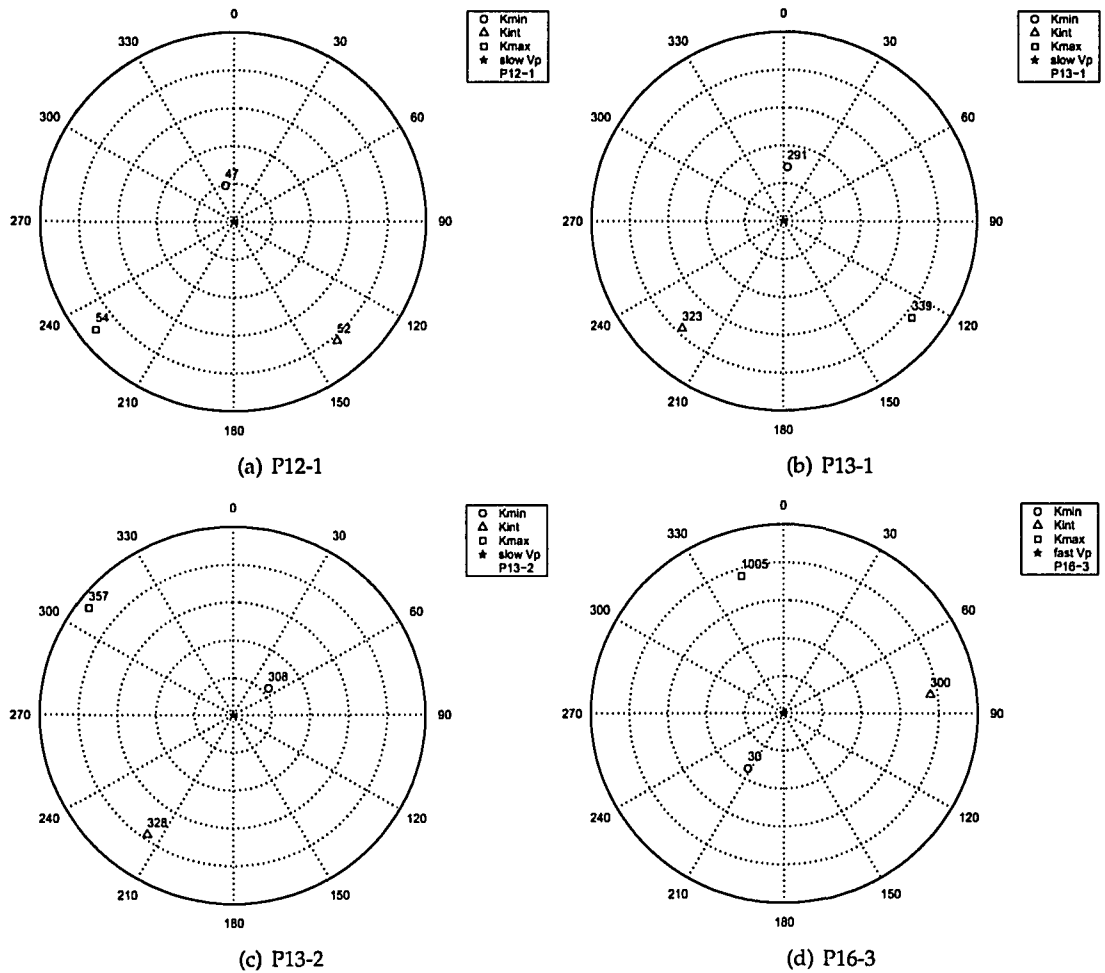
Figure 5.5: Continued, AMS minimum, intermediate, and maximum susceptibility axes of samples. The number near the symbols is magnetic susceptibility of each axis.

serpentine distribution network that surrounds olivine grains. If the original microcrack network influences the secondary magnetic mineral deposition and distribution during serpentinization, then the secondary magnetite produced during serpentinization may simulate the rock fabric along the original microcrack network. Hence, the preferred orientation of magnetite would be linked to olivine grain distribution. Based on AMS and seismic anisotropy experiments, the rock textures deduced from magnetic fabric and seismic anisotropy appear to compare favorably. That is, if the preferred orientation of the AMS carrier minerals consists of original paramagnetic minerals or if the secondary magnetic minerals (i.e. magnitite) mimic the orientation of the main phases, then AMS and seismic anisotropy are well correlated. Thus, AMS may offer useful information with respect to the foliation and the mineral fabric of rocks, regardless of whether magnetic anisotropy is caused by crystalline or shape anisotropy. This could greatly aid laboratory work because even if we know the crystal anisotropy of olivine and other minerals, it remains difficult to properly select the anisotropic direction of rocks for measurement. As a result, it maybe useful to carry out AMS measurements prior to the machining of samples for elastic anisotropic measurements, rather than after seismic measurements. Hence, AMS measurements may be a useful guide for preparing samples for seismic anisotropy and the selection of sites of transducer emplacement.

Most samples display a rough coincidence between the rock foliation and the fabric deduced from AMS measurements except for P08-3 and P16-3. For these two, the interpretation of foliation from AMS and from seismic anisotropy are still similar, but totally different with their sample-cutting planes. Samples P08-3 and P16-3 show abnormal phenomena in AMS measurement, because $K_{min}$ is not perpendicular to the principal rock texture, being the "presumed or observable foliation plane". The velocity measurements are also anomalous for these samples because the sample-cutting plane is not coincidence with the "presumed foliation plane". Usually, sample-cutting surfaces are parallel or perpendicular to the visible principal rock texture, i.e. "presumed foliation plane", but these two samples were without a clear visible texture making selection of the sampling cutting surface problematic. Interestingly, and despite of this difficulty, the data show that both AMS and seismic velocities are sensitive to the rock fabric, and they show the same indication of foliation. In addition, the comparison between AMS and seismic anisotropy in
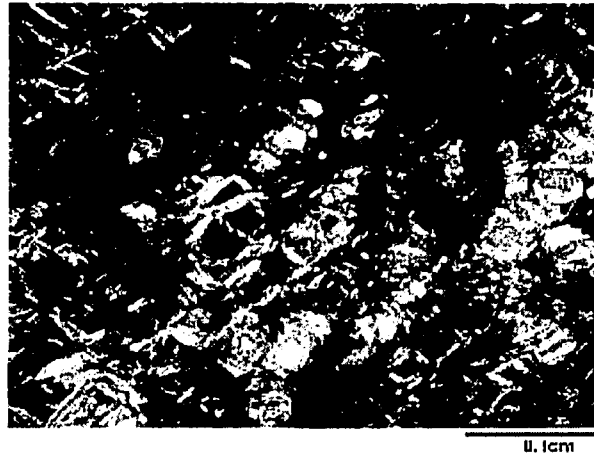
Figure 5.6: Olivine grains are surrounded by serpentine network (P 13-1). Thin section were taken under crossed polars.

Table 5.1: P-wave velocities and magnetic susceptibilities along Z-axis and within XY plane

|  | P13-2 | P13-1 | P11-1 | P08-3 | P04-2 | P03-1 | P12-1 | P16-3 |
|---|---|---|---|---|---|---|---|---|
| Kzz mean | 264.8 | 246.2 | 97.6 | 243 | 79.2 | 79.2 | 39.9 | 439.2 |
| Kxy mean | 329.5 | 314.3 | 125.4 | 292.5 | 98.9 | 105.1 | 50.9 | 627.3 |
| Kzz/Kxy | 0.8 | 0.78 | 0.78 | 0.83 | 0.8 | 0.75 | 0.78 | 0.7 |
| Vp zz (m/s; 200MPa) | 5632 | 5270 | 7454 | 6234 | 5798 | 6428 | 6777 | 6035 |
| Vp yy (m/s; 200MPa) | 5672 | 5359 | 7566 | 6546 | 6151 | 6974 | 7568 | 6174 |
| Vp zz/Vp yy | 0.99 | 0.98 | 0.99 | 0.95 | 0.94 | 0.92 | 0.9 | 0.98 |

Noted: $K_{xy} = \frac{K_{xx} + K_{yy}}{2}$

P16-3 proves that secondary magnetite indeed tracks the preferred orientation of the real rock fabrics. Otherwise, the accumulation of magnetic minerals may overlap the original rock fabrics of P16-3 (Figure A.9 in Appendix), which will lead to non-coincidence between AMS and the seismic anisotropy direction.

Even though the serpentine group minerals have a complex composition, we still hope to try some quantitative comparison between the intensities and directional dependence between AMS and the seismic anisotropy. The results show that there is not only a coincidence in the direction, but also possible in the intensities between AMS and seismic anisotropy. Presently, AMS measurements appear to be more sensitive to the composi-

110

tion of samples than seismic measurements due to the presence of additional minerals, for example, the secondary magnetite. P-wave velocity (200 MPa) ratio $Vpzz/Vpyy$ and magnetic susceptibility ratio $Kzz/Kxy$ in the Z-axis direction and along the X and Y plane are listed in Table 5.1. The ratios show that both magnetic susceptibility and velocity have a smaller value along the Z-axis than along the $XY$ plane. $Kzz$ represents the average magnetic susceptibility along the Z-axis, and $Kxy$ is the average magnetic susceptibility along the X and Y-axes. $Kzz/Kxy$ display a directional dependence in magnetic susceptibility similar to the measurement of velocity anisotropy, but the relative difference in velocities are much smaller than for magnetic susceptibility.

In order to make a more valid comparison between velocity anisotropy and AMS intensities, the anisotropic ratios of different parameters are chosen including P-wave velocities at 200 MPa , $Kzz$, and $Kxy$. For convenience of comparison, the anisotropic ratios are defined by the same calculation method for both seismic and magnetic parameters; being the ratio between the difference and the average value: $(A_{max} - A_{min}) \times 2/(A_{max} + A_{min})$. Figure 5.7 somehow shows that there may exists a possible correlation between these two ratios. A rough trend shows that an increase in magnetic anisotropy maybe corresponds to an increase in seismic anisotropy. We delete the sample P 16-3 in this figure, because in Chapter 2 the whole rock analysis shows that the composition of all other samples are similar to some extent except P 16-3. The reason that P 16-3 does not fit in the trend maybe caused by the extreme value of its magnetic susceptibility (see Table 4.1), which demonstrates another possibility that not only could the secondary magnetite as the major magnetic mineral greatly change the magnitude of AMS, but also may develop along another system of fractures not related to olivine orientation. AMS is much more sensitive to rock composition than seismic anisotropy in case of relatively low temperature metamorphism when only part of rock has been modified. The comparability between magnetic anisotropy ratio and seismic anisotropy ratio should be careful with the existing of the primary olivine and secondary serpentine mixture. In most of high grade metamorphic rocks when absolute majority of minerals are formed at the same time during heat/pressure, the AMS indeed shows the rock fabrics.

The variances of accessory magnetic minerals should be noted as an important influence in quantitative comparison in the future. We should obtain more useful information

111
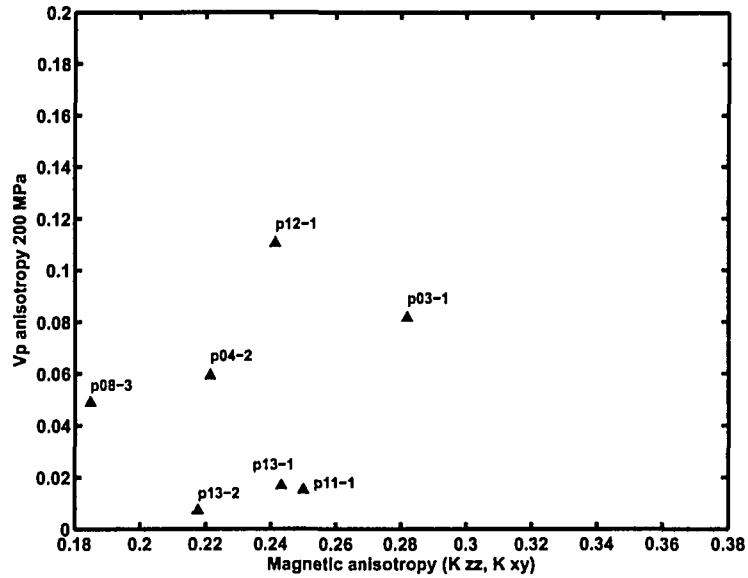
Figure 5.7: Vp anisotropy (200 MPa) vs. Magnetic anisotropy $(2 \times \frac{K_{xy}-K_{zz}}{K_{xy}+K_{zz}})$

quantitatively concerning the factors to influence the relationship between the intensity of magnetic susceptibility and the rock magnetic fabric for more pure minerals and typical rocks. These may further allow us to compare rock fabrics with the magnetic fabrics.

## 5.5 Conclusion

In this chapter, we compared AMS with seismic anisotropy in a suite of samples from the Pindos and Vourinos ophiolite (Greece), with densities ranging from 2.6 to 3.28 $g/cm^3$. The magnitude of bulk magnetic susceptibility in laboratory measurements shows that bulk AMS of the rocks is derived from both paramagnetic minerals and magnetite. Because the serpentinization reaction can produce magnetite, the magnetic anisotropy ratio increases with seismic anisotropy properly only within the necessary limit that there is not too much variability of the magnetic minerals among samples. There is a generally good coincidence between the direction of magnetic fabric and rock texture deduced from the seismic method. The $K_{min}$ axis of the AMS ellipsoid trends to be perpendicular to the rock foliation plane for most samples; while, the plane of magnetic fabric (con-

112

sisting of $K_{max}$ and $K_{int}$) trends to coincide with the rock foliation plane. In agreement with other research (*Hrouda et al.*, 1988; *Bina and Henry*, 1990; *Siegesmund and Dahms*, 1994; *Yaouancq and Macleod*, 2000; *Lagroix and Borradaile*, 2000; *Bascou et al.*, 2002; *Lawrence et al.*, 2002), AMS could act as a proxy for the orientation distribution of rock fabric (Figure 5.3). But, caution is necessary in the direct interpretation of preferred crystallographic orientations of crustal rocks before determining the reliability of AMS in some samples.

Although we cannot exclude that paramagnetic and ferromagnetic components can have different AMS orientation when serpentization occurred not along the olivine's LPO, but based on the orientation of fractures around olivine grains in the thin section photos we may assume that the fracture preferred orientation is co-axial with the LPO. That explains why AMS and seismic anisotropy correlate each other. Further, from the paper by *Ashworth and Chambers* (2000) magnetite has "crystallographic orientation related to that of olivine" in symplectites. They found that the thin platelets of magnetite is parallel to [100] of olivine. So, this may be an alternative explanation why the AMS should be co-axial with seismic anisotropy in serpentinized samples.

In this research, AMS arises from paramagnetic minerals and the secondary magnetite that follows the orientation of the main textural phases of the samples. Velocities and calculation of elastic properties in chapter 3 evaluated the symmetries and rock texture of samples. The axis of symmetry of the samples exhibit a good correlation with $K_{min}$ axis of the AMS ellipsoid. The plane of rock fabric deduced from the AMS ellipsoid generally correlates with the observed principal texture of the rocks. Therefore, this research suggests that magnetic fabric analysis could be a useful proxy for prediction of petrofabric measurement.

# Chapter 6

# Future work

Vourinos Ophiolite with high magnetic susceptibility is a good candidate for comparison between AMS studies and seismic anisotropy . Magnetic fabrics are usually representative of the secondary magnetite in serpentinization and the primary paramagnetic minerals assemblage. The secondary magnetite produced in serpentinization can somehow mimic the principal rock texture. The studies show that generally there are coincidences in both directions and possible intensities between anisotropy of magnetic susceptibility and seismic anisotropy, although some angular departures between axes in two different systems are present. Nonetheless, studying and understanding the similarity between AMS and seismic anisotropy may help to develop a new method using fabrics deduced from fast and simple AMS measurements instead of traditional laboratory ultrasonic methods. This could guide the design of elastic anisotropy measurement in the future.

Magnetic susceptibility, AMS, P- and S-wave velocities, and seismic anisotropy are all external manifestations of the intrinsic crystallographic properties of rock-forming minerals. Magnetic fabrics were obtained from the AMS measurements; petrofabric was evaluated based on P- and S-wave velocity measurement on the same samples. The relationship between petrofabric and magnetic fabric and their mutual directional dependence, compared favorably. This study presents only a semi-qualitative conclusion at this point in the research, but it identified an interesting correlation between anisotropy of magnetic susceptibility (AMS) and seismic anisotropy, this will allow us to develop numerical method to quantitatively evaluate the comparability in the future. On the

114

other hand, anisotropy of low field magnetic susceptibility (AMS), as a sensitive indicator of rock texture and strain by its intrinsic petrofabric meanings, is used to measure and deduce the petrofabric of rocks. But, although sensitive, its interpretation could be easily complicated by tiny compositional changes, for example, magnetite in reaction of serpentinization. So, caution is always necessary. In general, the degree of preferential orientation of the magnetic and other rock-forming minerals contained in a rock has significant effects both in the magnetic ellipsoid and the seismic anisotropy. Although we conclude that the magnetic fabrics could be an useful proxy in determining the petrofabric, this is not to imply that the comparability between magnetic anisotropy and seismic anisotropy is simple. Some problems could arise in the interpretation of the magnetic fabrics of rocks just as in other techniques of petrofabric analysis. Quantitatively comparison between AMS and seismic anisotropy will be the important topic in the future work. To accurately evaluate the influence of mineral orientation and composition, theoretical work on the quantitative relationship between the magnetic fabric and rock fabric is imperative. In addition, to really compare rock texture and quantitatively describe mineral orientation, more quantitative texture information will need to be obtained from X-ray, neutron, or electron (EBSD) background scattered diffraction techniques to improve the texture analysis in this phase.

The numerical modeling method offers a good approach to assess the petrofabric quantitatively for single crystal and polymineralic assembly both for seismic anisotropy and AMS. For seismic anisotropy, velocities are closely related to the intrinsic structure. Seismic velocities by laboratory experiment can be used to evaluate anisotropies, elasticity, and symmetries for the whole mineral assembly. Since seismic properties of single crystals are known for many rock-forming minerals, the overall seismic velocities and anisotropies of polycrystalline rocks could be computed according to the Christoffel equation and Voigt-Reuss-Hill averaging scheme by considering the LPO and the fraction volume of each constituent mineral. There are many theoretical works to explain the relationship between seismic anisotropy and the texture of the constituent minerals by considering the single crystal properties and quantifying the elastic properties. But, comparison to seismic anisotropy, however, there are few laboratory and theoretical works devoted to AMS calculation. In principle, we could calculate AMS from texture,

LPO, and the properties of single crystal by considering their fraction volume, using similar methods as used for computation of seismic properties. For the theoretical work of AMS, one of the major problems concerning with the source of magnetic susceptibility is the quantitative relationship between the magnetic fabric and rock fabric. Another problem is a lack of detailed magnetic database of minerals and rock, because magnetic susceptibilities of single crystal usually vary in a range instead of a constant value by the sensitivity to its composition.

We still need to obtain more useful information quantitatively concerning the factors influencing relationships between the intensity of magnetic susceptibility and the magnetic fabric. A more sophisticated theoretical model of AMS will help to understand the complexities of magnetic fabric by different minerals and rocks.

# Bibliography

Abramson, E. H., J. M. Brown, L. J. Slutsky, and J. Zaug, The elastic constants of san carlos olivine to 17 gpa, *J. Geophys. Res., 102(B6)*, 12,253–12,264, 1997.

Allen, D. E., and W. E. Seyfried, Compositional controls on vent fluids from ultramatic-hosted hydrothermal systems at mid-ocean ridges: An experimental study at 400 degrees c, 500 bars, *GEOCHIMICA ET COSMOCHIMICA ACTA, 67*, 1531–1542, 2003.

Ashworth, J. R., and A. D. Chambers, Symplectic reaction in olivine and the controls of intergrowth spacing in symplectites, *Journal of Petrology, 41*, 285–304, 2000.

Au, D., and R. M. Clowes, Crustal structure from am obs survey of the nootka fault zone off western canada, *Geophysical Journal of the Royal Astronomical Society, 68*, 27–47, 1982.

Auld, B. A., *Acoustic fields and waves in solids*, R.E. Krieger, 1990.

Baker, D. W., and N. L. Carter, Seismic velocity anisotropy calculated for ultramafic minerals and aggregates, *Geophys. Monogr., Am. Geophys. Union, 16*, 157–166, 1972.

Balsey, J. R., and A. F. Buddington, Magnetic susceptibility anisotropy and fabric of some adirondack granites and orthogneisses, *Am. J. Sci., 258(A)*, 6–20, 1960.

Barruol, G., and H. Kern, Seismic anisotropy and shear-wave splitting in the lower-crustal and upper-mantle rocks from the ivrea zone-experimental and calculated data, *Phys. Earth Planet. Inter., 95*, 175–194, 1996.

Bascou, J., G. Barruol, A. Vauchez, D. Mainprice, and M. E. Silva, Ebsd-measured lattice-preferred orientations and seismic properties of eclogites, *Tectonophysics, 342*, 61–80, 2001.

Bascou, J., M. I. B. Raposo, A. Vauchez, and M. E. Silva, Titanohematite lattice-preferred orientation and magnetic anisotropy in high temperature mylonites, *Earth and Planet. Sci. Lett., 198*, 77–92, 2002.

Bass, J. D., Elasticity of minerals, glasses, and melts, in *Mineral Physics and Crystallgraphy,A Handbook of Physical Constants*, edited by A. R. S. 2, 1995.

Ben-Ismail, W., and D. Mainprice, An olivine fabric database: an overview of upper mantle fabrics and seismic anisotropy, *Tectonophysics, 296(1-2)*, 145–157, 1998.

Best, M. G., *Igneous and metamorphic petrology*, Blackwell publishing, 2003.

117

Bina, M., and L. Daly, Mineralogical change and self-reversed magnetizations in pyrrhotite resulting from partial oxidation; geophysical implications, *Physics of the Earth and Planetary Interiors, 85,* 83–99, 1994.

Bina, M., and B. Henry, Magnetic properties, opaque mineralogy and magnetic anisotropies of serpentinized peridotites from odp hole 670a near the mid-atlantic ridge, *Physics of the Earth and Planetary Interiors, 65,* 88–103, 1990.

Birch, F., The velocity of compressional waves in rocks to 10 kilobars. 1, *J. Geophys. Res., 65,* 1083–1102, 1960.

Birch, F., The velocity of compressional waves in rocks to 10 kilobars. 2, *J. Geophys. Res., 66,* 2199–2224, 1961.

Blum, P., *Physical properties handbooks: a guide to the shipboard measurement of physical properties of deep-sea cores,* ODP Tech. Note, 26, 1997.

Borradaile, G., Magnetic susceptibility, petrofabrics and strain, *Tectonphysics, 156,* 1–20, 1988.

Borradaile, G., Correlation of strain with anisotropy of magnetic susceptibility (ams), *Pure and Applied Geophysics, 135,* 15–29, 1991.

Borradaile, G., Magnetic fabrics and petrofabrics: their orientation distributions and anisotropies, *J. Struct. Geol., 23,* 1581–1596, 2001.

Borradaile, G., and D. Gauthier, Interpreting anomalous magnetic fabrics in ophiolite dike, *J. Struct. Geol., 25,* 171–182, 2003.

Borradaile, G., and B. Henry, Tectonic applications of magnetic susceptibility and its anisotropy, *Earth Sci. Rev., 42,* 49–93, 1997.

Borradaile, G., and F. Lagroix, Magnetic fabrics reveal upper mantle flow fabrics in the troodos ophiolite complex, cyprus, *J. Struct. Geol., 23,* 1299–1317, 2001.

Borradaile, G. J., and Stupavsky, Anisotropy of magnetic susceptibility: Measurement schemes, *Geophysical Research Letters, 22,* 1957–1960, 1995.

Borradaile, G. J., W. Keeler, C. Alford, and P. Sarvas, Anisotropy of magnetic susceptibilty of some metamorphic minerials, *Physics of the Earth and Planetary Interiors, 48,* 161–166, 1987.

Bostock, M. G., R. D. Hyndman, S. Rondenay, and S. M. Peacock, An inverted continental moho and serpentinization of the forearc mantle, *NATURE, 417,* 536–538, 2002.

Carlson, R., Seismic velocities in the uppermost oceanic crust: Age dependence and the fate of layer 2a, *J. Geophys. Res., 103 (B4),* 7069–7077, 1998.

Carlson, R., and D. J. Miller, A new assessment of the abundance of serpentinite in the oceanic crust, *Geophysical Research Letters, 24,* 457–460, 1997.

Cheadle, S. P., R. J. Brown, and D. C. Lawton, Orthorhombic anisotropy: A physical seismic modeling study, *Geophysics, 56,* 1603–1613, 1991.

118

Cholach, P., *The elasticity of intrinsically anisotropic rocks*, PhD. thesis, University of Alberta, 2005.

Cholach, P., J. Molyneux, and D. R. Schmitt, Flin flon belt seismic anisotropy: elastic symmetry, heterogeneity, and shear wave splitting, *in press Can. J. Earth Sciences, manuscript pp. 50.*, 2005.

Christensen, N. I., Compressional wave velocities in metamorphic rocks at pressures to 10 kilobars, *J. Geophys. Res., 70*, 6147–6164, 1965.

Christensen, N. I., Shear wave velocities in metamorphic rocks at pressures to 10 kilobars, *J. Geophys. Res., 71*, 3549–3556, 1966a.

Christensen, N. I., Elasticity of ultrabasic rocks, *J. Geophys. Res., 71*, 5921– 5931, 1966b.

Christensen, N. I., The abundance of serpentinites in the oceanic crust, *J. of Geology, 80*, 709– 719, 1972.

Christensen, N. I., Ophiolites, seismic velocities and oceanic crustal structure, *Tectonophysics, 47*, 131–157, 1978.

Christensen, N. I., Serpentinites, peridotites, and seismology, *Int. Geol. Rev., 46*, 795–816, 2004.

Christensen, N. I., and R. S. Crosson, Seismic anisotropy in the upper mantle, *Tectonophysics, 6*, 93– 107, 1968.

Christensen, N. I., and R. Ramanana, Elasticity and anisotropy of dunite to 10 kbars, *J. Geophys. Res., 76*, 4003– 4010, 1971.

Christensen, N. I., and M. H. Salisbury, Structure and constitution of the lower oceanic crust, *Rev. Geophys. Space Phys., 13*, 57– 86, 1975.

Christensen, N. I., and M. H. Salisbury, Seismic anisotropy in the oceanic upper mantle: Evidence from the bay of islands ophiolite complex, *J. Geophys. Res., 84*, 4601– 4610, 1979.

Christensen, N. I., and J. D. Smewing, Geology and seismic structure of the northern section of the oman ophiolite, *J. Geophys. Res., 81*, 2545–2555, 1981.

Coleman, R. G., *Ophiolites - Ancient Oceanic Lithosphere?*, Springer-Verlag, New York, 229 pp., 1977.

Collison, D., *Methods in Rock Magnetism and Paleomagnetism*, Chapman and Hall, London, 503p., 1983.

Covey-Crump, S. J., P. Schofield, and I. C. Stretton, Using neutron diffraction to investigate the elastic properties of anisotropic rocks: Results from an olivine plus orthopyroxene mylonite, *Journal of Geophysical Research, 108 (B2)*, No. 2092, 2003.

Cox, A., and R. R. Doell, Review of paleomagnetism, *Bull. Geol. Soc. Am., 71*, 645–768, 1960.

Crampin, S., Seismic wave propagation through a cracked solid: polarization as a possible dilatancy diagnostic, *Geophy. J. R. Astron. Soc., 53*, 467–496, 1978.

Crampin, S., A review of wave motion in anisotropic and cracked elastic-media, *Wave Motion, 3*, 343–391, 1981.

Crosson, R. S., and J. W. Lin, Voigt and reuss prediction of anisotropic elasticity of dunite, *J. Geophys. Res., 76(2)*, NO 570, 1971.

Dankers, P., Relationships between median destructive field and remanent coercive forces for dispersed natural magnetite, titanomagnetite, and hematite, *Geophys. J. R. Astr. Soc., 64*, 447–461, 1981.

Deer, Z., Howie, *An introduction to The Rock - Forming Minerals*, 2nd ed., Longman Scientific and Technical, 1992.

Detrick, R., J. Collins, R. Stephen, and S. Swift, In situ evidence for the nature of the seismic layter 2/3 boundary in oceanic crust, *Nature, 370*, 288–290, 1994.

Dewandel, B., F. Boudier, H. Kern, W. Warsi, and D. Mainprice, Seismic wave velocity and anisotropy of serpentinized peridotite in the oman ophilite, *Tectonophysics, 370*, 77–94, 2003.

Dilek, Y., Ophiolite pulses, mantle plumes and orogeny, in *Ophiolites in Earth History*, edited by Y. Dilek and P. Robinson, vol. Geological Society, London, Special Publications, pp. 218, 9–19, 2003.

Dilek, Y., M. Shallo, and H. Furnes, Rift-drift, seafloor spreading, and subduction tectonics of albanian ophiolites, *Int. Geol. Rev., 47*, 147–176, 2005.

Dodony, I., and P. R. Buseck, Serpentines close-up and intimate: An hrtem view, *International Geology Review, 46*, 507–527, 2004.

Dunlop, D., and O. Özdemir, *Rock magnetism: Fundamentals and frontiers*, Cambridge University Press, 1997.

Dunlop, D., and M. Prévot, Magnetic properties and opaque mineralogy of drilled submarine intrusive rocks, *Geophys. J. Roy. Astron. Soc., 69*, 763–802, 1982.

Dunn, R. A., and D. R. Toomey, Crack induced seismic anisotropy in the oceanic crust across the east pacific rise, *Earth and Planetary Res. Lett., 189*, 9–17, 2001.

Evans, B. W., The serpentinite multisystem revisited: Chrysotile is metastable, *International Geology Review, 46*, 479–506, 2004.

Falini, G., E. Foresti, M. Gazzano, A. F. Gualtieri, M. Leoni, I. G. Lesci, and N. Roveri, Tubular-shaped stoichiometric chrysotile nanocrystals, *Chem. Eur. J., 10*, 3043–3049, 2004.

Fedorov, F. I., *Theory of elastic waves in crystals*, Plenum Press, 1968.

Ferré, E. C., F. Martín-Hernández, C. Teyssier, and M. Jackson, Paramagnetic and ferromagnetic anisotropy of magnetic susceptibility in migmatites: measurements in high and low fields and kinematic implications, *Geophy. J. Int., 157*, 1119–1129, 2004.

Ferré, E. C., B. Tikoff, and M. Jackson, The magnetic anisotropy of mantle peridotites: Examples for the twin sisters dunite, washington, *Tectonophysics, 398*, 141–166, 2005.

120

Flower, M. F. J., and Y. Dilek, Arc-trench rollback and forearc accretion: 1. a collision-induced mantle flow model for tethyan ophiolite, in *Ophiolites in Earth History*, edited by Y. Dilek and P. Robinson, vol. Geological Society, London, Special Publications, pp. 218, 9–19, 2003.

Gaherty, J. B., D. Lizarralde, and C. J. A., Mantle defomation during slow seafloor spreading constrained bv observations of seismic anisotropy in the western atlantic, *Earth and Planetary Science Letters, 228(3-4)*, 255–265, 2004.

Gangi, A. F., and R. L. Carlson, An asperity-deformation model for effective pressure, *Techtonophysics, 256(1-4)*, 241–251, 1996.

Girdler, R. W., The measurement and computation of anisotropy of magnetic susceptibility of rocks, *Geophys. J. R. Astr. Soc., 5*, 34–44, 1961.

Granar, L., Magnetic measurements on swedish varved sediments, *Arkiv. F. Geofysik, 3*, 1–40, 1958.

Grevemeyer, I., and W. Weigel, Increase of seismic velocities in upper oceanic crust: The 'superfast' spreading east pacific rise at $14^\circ 14's$, *Geophys. Res. Lett., 24*, 217–220, 1997.

Hanna, W. F., Weak-field magnetic susceptibility anisotropy and its dynamic measurement, *U. S. Geol. Surv. Bull., 1418*, 1–73, 1977.

Hargraves, R. B., D. Johnson, and C. Y. Chan, Distribution anisotropy: the cause of ams in igneous rocks?, *Geophys, Res. Lett., 18*, 2193–2196, 1991.

Helbig, K., *Foundations of anisotropy for exploration seismics*, Pergamon, 1994.

Hess, H. H., Seismic anisotropy of the upper mantle under oceans, *Nature, 230*, 629–631, 1964.

Holbrook, W. S., W. D. Mooney, and N. I. Christensen, The seismic velocity structure of the deep continental crust, in *The Continental Lower Crust, Developments in Geotectonics*, edited by D. M. Fountain, R. Arculus, and R. Kay, vol. 23, pp. 1–34, 1992.

Horen, H., M. Zamora, and G. Dubuisson, Seismic waves velocities and anisotropy in serpentinized peridotites from xigaze ophiolite: abundance of serpentine in slow spreading ridge, *Geophys. Res. Lett., 23*, 9 – 12, 1996.

Hornby, B. E., Experimental determination of the anisotropic elastic properties of shales, in *Seismic anisotropy*, edited by E. Fjar and R. M. Holt, vol. Society of Exploration Geophysicists, pp. 238–296, 1996.

Hrouda, F., Magnetic anisotropy of rocks and its application in geology and geophysics, *Geophys. Surv., 5*, 37–82, 1982.

Hrouda, F., S. Jacko, and J. Hanák, Parallel magnetic fabrics in metamorphic, granitoid and sedimentary rocks of the branisko and Čierna hora mountains (e slovakia) and their tectonometamorphic control, *Physics of the Earth and Planetary Interiors, 51*, 271–289, 1988.

Ising, E., On the magnetic properties of varved clay, *Arkiv Astron. Fysik, 29 A(5)*, 1–37, 1942.

Jackson, M., Anisotropy of magnetic remanence: a brief review of mineralogical sources, physical origins and geological applications, and comparison with susceptibility anisotropy, *Pure Appl. Geophys., 136*, 1–28, 1991.

Janák, F., Determination of anisotropy of magnetic susceptibility of rocks, *Studia geoph. et geod., 9*, 290–300, 1965.

Jelinek, V., The statistical theory of measuring anisotropy of magnetic susceptibility of rocks and its applcation, *Brno, Geofyzika*, pp. 1–88, 1977.

Jelinek, V., Statistical processing of anisotropy of magnetic susceptibility measured on groups of specimens, *Studia geoph. et geod., 22*, 50–62, 1978.

Jelinek, V., Characterization of the magnetic fabric of rocks, *Tectonophysics, 79*, 63–67, 1981.

Ji, S., and M. Salisbury, Shear-wave velocities, anisotropy and splitting in high grade mylonites, *Tectonphysics, 221*, 453–473, 1993a.

Ji, S., and Z. Wang, Elastic properties of fosterite-enstatite composites up to 3.0 gpa, *J. Geodynamics, 28*, 147–174, 1999.

Ji, S., M. Salisbury, and S. Hanmer, Petrofabric, p-wave anisotropy and seismic reflectivity of high-grade tectonites, *Tectonphysics, 222*, 195–226, 1993b.

Ji, S., X. Zhao, and D. Francis, Calibration of shear-wave splitting in the subcontinental upper mantle beneath active orogenic belts using ultramafic xenoliths from the canadian cordillera and alaska, *Tectonphysics, 239*, 1–28, 1994.

Johnston, J. E., and N. I. Christensen, Seismic anisotropy of shales, *J. Geophys. Res., 100(B4)*, 5991–6003, 1995.

Jones, T., and A. Nur, Seismic velocity and anisotropy in mylonites and the reflectivity of deep crustal fault zones, *Geology, 10*, 260–263, 1982.

Jones, T., and A. Nur, The nature of seismic reflections from deep crustal fault zones, *J. Geophys. Res., 89(B5)*, 3153–3171, 1984.

Juteau, T., M. Cannat, and Y. Lagabrielle, Serpentinized peridotites in the upper ocean crust away from transform zones: A comparison of the results of previous dsdp and odp legs, *Proc. Ocean Drilling Prog., Scientific Results, 106*, 303–3o8, 1990.

Kaarsberg, E. A., Introductory studies of natural and artificial argillaceous aggregates by sound-propagation and x-ray diffraction methods, *J. Geol., 67*, 447–472, 1959.

Kelso, P. R., B. Tikoff, M. Jackson, and W. Sun, A new method for the separation of paramagnetic and ferromagnetic susceptibility anisotropy using low field and high field methods, *Geophysical Journal International, 151*, 345–359, 2002.

Kern, H., P- and s-waves velocities in a crustal and mantle rocks under the simultaneous action of high confining pressure and high temperature and the effect of the rock microstructure, in *High-Pressure Research in Geosciences*, edited by W. Schreyer, vol. Schweitzerbart, Stuttgart, pp. 15–45, 1982.

Kern, H., P- and s-wave anisotropy and shear wave splitting at pressure and temperature in possible mantle rocks and their relation to the rock fabric, *Phys. Earth Planet. Inter.*, *78*, 245–256, 1993.

Kern, H., Relationship between crystallographic fabric (texture) and elastic properties of rocks: Implications from experiments and calculations, *Materials Science Forum, 426(4)*, 3635–3642, 2003.

Kern, H., and J. M. Tubia, Pressure and temperature-dependence of p-wave and s-wave velocities, seismic anisotropy and density of sheared rocks from the sierra alpujata massif (ronda pertdotites, southern spain), *Earth and Planetary Science Letters, 119*, 191–205, 1993.

Kern, H., L. Burlini, and I. V. Ashchepkov, Fabric-related seismic anisotropy in upper-mantle xenoliths: evidence from measurements and calculations, *Phys. Earth Planet. Inter.*, *95*, 195–209, 1996.

Kern, H., B. Liu, and T. Popp, Relationship between anisotropy of p and s wave velocities and anisotropy of attenuation in serpentinite and amphibolite, *J. Geophys. Res.*, *102(B2)*, 3051–3065, 1997.

Lagroix, F., and G. Borradaile, Magnetic fabric interpretation complicated by inclusions in mafic silicates, *Tectonophysics, 325*, 207–225, 2000.

Lawrence, R. M., J. S. Gee, and J. A. Karson, Magnetic anisotropy of serpentinized peridotites from the mark area: Implications for the orientation of mesoscopic structures and major fault zones, *J. Geophys. Res., 107*, No. 2073, 2002.

Leiss, B., K. Ullemeyer, K. Weber, H. G. Brokmeier, H. J. Bunge, M. Drury, U. Faul, F. Fueten, A. Frischbutter, H. Klein, W. Kuhs, P. Launeau, G. E. Lloyd, D. J. Prior, C. Scheffzuk, T. Weiss, K. Walther, H. R. Wenk, and F. K. Levin, Recent developments and goals in texture research of geological materials - preface, *Journal of Structural Geology, 22*, 1531–1540, 2000.

Long, C., and N. I. Christensen, Seismic anisotropy of south african upper mantle xenoliths, *Earth and Planetary Science Letters, 179*, 551–565, 2000.

Lowrie, W., *Fundamentals of Geophysics*, Cambridge University Press, 1997.

MacDonald, W. D., and B. B. Ellwood, Magnetic fabric of peridotite with interscting petrofabric surfaces, tinaquillo, venezuella, *Physics of the Earth and Planetary Interiors, 51*, 301–312, 1988.

Mah, M., *Experimental determination of the elastic coefficients of anisotropic materials with the slant-stack method*, M. Sc. thesis, University of Alberta, 1999.

Mah, M., and D. R. Schmitt, Experimental determination of the elastic coefficients of an orthorhombic material, *Geophysics, 66*, 1217–1225, 2001.

Mah, M., and D. R. Schmitt, Determination of the complete elastic stiffness from ultrasonic velocity measurements, *J. Geophys. Res., 108(B1)*, 2016, 2003.

Mainprice, D., and M. Humbert, Methods of calculating petrophysical properties from lattice preferred orientation data, *Surv. Geophys., 15*, 575–592, 1994.

123

Mainprice, D., and P. Silver, Interpretation of sks-waves using samples from the subcontinental lithosphere, *Phys. Earth Planet. Inter.*, *78*, 257–280, 1993.

Markham, M. F., Measurement of elastic constants by the ultrasonic pulse method, *British J. Appl. Phys.*, *6*, 56–63, 1957.

Martin-Hernandez, F., and A. M. Hirt, The anisotropy of magnetic susceptibility in biotite, muscovite and chlorite single crystals, *Tectonophysics*, *367*, 13–28, 2003.

Miller, D. J., and N. I. Christensen, Seismic velocities of lower crustal and upper mantle rocks from the slow-spreading mid-atlantic ridge, south of the kane transform zone (mark), *Proc. Ocean Drill. Program Sci. Results*, *153*, 437–454, 1997.

Molyneux, J. B., and D. R. Schmitt, First break timing: Arrival times by direct correlation, *Geophysics*, *64*, 1492–1501, 1999.

Molyneux, J. B., and D. R. Schmitt, Compressional-wave velocities in attenuating media: A laboratory physical modeling study, *Geophysics*, *65*, 1162–1167, 2000.

Moores, E. M., L. H. Kellogg, and Y. Dilek, Tethyan ophiolites, mantle convection, and tectonic 'historical contingency': A resolution of the 'ophiolite conundrum', in *Ophiolites and Oceanic Crust: New Insights from Field Studies and the Ocean Drilling Program: Boulder, Colorado*, edited by Y. Dilek, E. M. Moores, D. Elthon, and A. Nicoas, vol. Geological Society of America Special Paper 349, pp. 3–12, 2000.

Musgrave, M. J. P., *Crystal acoustics*, Holden Day, 1970.

Nagata, T., *Rock magnetism*, 2 ed., Maruzen, Tokyo, 1961.

Nicholas, A., and N. I. Christensen, Formation of anisotropy in upper mantle peridotites - a review, in *Composition, Structure and Dynamics of the Lithosphere - Ashenosphere system*, edited by K. Fuchs and C. Froidevaux, vol. Geodyn. Series, 16, pp. 111–123, 1987.

Nickel, E. H., and M. Nichols, *Mineral reference manual*, Van Nostrand Reinhold. New York, 1991.

Nur, A., and G. Simmons, Stress-induced velocity anisotropy in rocks: an experimental study, *J. Geophys. Res.*, *74*, 6667–6674, 1969.

Nye, J. F., *Physical properties of Crystal*, Oxford University, 1957.

O'Hanley, D. S., *Serpentinites: Records of petrologic and tectonic history. Oxford Monographs in Geology and Geophysics. no. 34*, Oxford University, 1996.

O'Reilly, B. M., F. Hauser, A. W. B. Jacob, and P. M. Shannon, The lithosphere below the rockall trough: Wide-angle seismic evidence for extensive serpentinisation, *Tectonophysics*, *255*, 1–23, 1996.

Oufi, O., M. Cannat, and H. Horen, Magnetic properties of variably serpentinized abyssal peridotites, *J. Geophy. R.*, *107*, No. 2095, 2002.

Owens, W. H., Mathematical model studies on factors affecting the magnetic anisotropy of deformed rocks, *Tectonphysics*, *24*, 115–131, 1974.

Peselnick, L., A. Nicolas, and P. R. Stevenson, Velocity anisotropy in a mantle peridotite from the ivrea zone: application to upper mantle anisotropy, *J. Geophys. Res.*, 79, 1175–1182, 1974.

Pros, Z., and V. Babuska, A method for investigating the elastic anisotropy on spherical rock samples, *Z. Geophys.*, 33, 289–291, 1967.

Pros, Z., T. Lokajicek, R. Prikryl, and K. Klima, Direct measurement of 3d elastic anisotropy on rocks from the ivrea zone (southern alps, nw italy), *Tectonophysics*, 370, 31–47, 2003.

Ranero, C. R., and V. Sallares, Geophysical evidence for hydration of the crust and mantle of the nazca plate during bending at the north chile trench, *Geology*, 32, 549–552, 2004.

Rassios, A., L. Beccaluva, V. Bortolotti, A. Mavrides, and E. M. Moores, The vourinos ophiolitic complex, *Ofioliti*, 8, 275–292, 1983.

Rassios, A. G., A. ad Smith, Constraints on the formation and emplacement age of western greek ophiolites (vourinos, pindos, and othris) inferred from deformation structures in peridotites, in ophiolites and oceanic crust, in *New insights from Field Studies and the Ocean Drilling Program*, edited by Y. Dilek, E. Moores, D. Elthon, and A. Nicolas, vol. Geological Soc. Amer. Special Paper, 349, pp. 473–483, 2000.

Robertson, A., Development of concepts concerning the genesis and emplacement of tethyan ophiolite in the eastern mediterranean and oman regions, *Earth-Science Reviews*, 66, 331–387, 2004.

Rochette, P., M. Jackson, and C. Aubourg, Rock magnetism and the interpretation of anisotropy of magnetic susceptibility, *Rev. Geophys.*, 30, 209–226, 1992.

Ross, J. V., and J. Zimmerman, Comparison of evolution and tectonic significance of the pindos and vourinos ophiolite suite, northern greece, *Tectonophysics*, 256, 1–15, 1996.

Ross, J. V., J. C. C. Mercier, H. G. Avelallemant, N. L. Carter, and J. Zimmerman, The vourinos ophiolite complex, greece - the tectonite suite, *Tectonophysics*, 70, 63–83, 1980.

Salisbury, M., and N. I. Christensen, The seismic velocity structure of a traverse through the bay of islands ophiolite complex, newfoundland, and exposure of oceanic crust and upper mantle, *J. Geophys. Res.*, 83 (B2), 805–817, 1978.

Salisbury, M., N. I. Christensen, and R. H. Wilkens, Nature of the layer 2/3 transition from comparison of laboratory and logging velocities and petrology at the base of hole 504b, *Proc. Ocean Drilling Prog., Scientific Results*, 148, 409–414, 1996.

Savage, M. K., Seismic anisotropy and mantle deformation: What have we learned from shear wave splitting?, *Reviews of Geophysics*, 37 (1), 65–106, 1999.

Shearer, P. M., and J. A. Orcutt, Compressional and shear-wave anisotropy in the oceanic lithosphere - the ngendei seismic refraction experiment, *Geophysical Journal of the Royal Astronomical Society*, 87, 967–1003, 1986.

Siegesmud, S., T. Takeshita, and H. Kern, Anisotropy of vp and vs in an amphibolite of the deep crust and its relationship to the mineralogical, microstructural and textural characteristics of the rock, *Tectonophysics*, 157, 25–38, 1989.

Siegesmund, S., and M. Dahms, Fabric-controlled anisotropy of elastic, magnetic and thermal properties of rocks, in *Textures of Geological Materials Deutsche Gesellschaft fr Materialkunde-Informationsgesellschaft-Verlag*, edited by H. J. Bunge, S. Siegesmund, S. Skrotzki, and K. Weber, vol. Oberursel, pp. 353–379, 1994.

Silver, P. G., Seismic anisotropy beneath the continents: Probing the depths of geology, *Annu. Rev. Earth Space Sci.*, 24, 385–432, 1996.

Smith, A. G., The tectonic significance of the hellenic-dinaric ophiolites, *Geological Society of London Spec. Pub.*, 76, 213–243, 1993.

Song, I., M. Suh, Y. K. Woo, and T. Hao, Determination of the elastic modulus set of foliated rocks from ultrasonic velocity measurements, *Engineering Geology*, 72, 293–308, 2004.

Stacey, F. D., Magnetic anisotropy of igneous rocks, *J. Geophys. Res.*, 65, 2429–2442, 1960.

Stampfi, G. M., and G. Borel, The transmed transects in space and time: constrainst on the paleotectonic evolution of the mediterranean domain, in *The Transmed Atlas: The Mediterranean Region from Crust to Mantle*, edited by W. Cavazza, F. M. Roure, W. Spakman, G. M. Stampfli, and P. A. Ziegler, vol. Springer-Verlag, Berlin, pp. 53–80, 2004.

Stephenson, A., Distribution anisotropy: two simple models for magnetic lineation and foliation, *Phys. Earth Planet. Inter.*, 82, 49–54, 1994.

Tarling, D. H., *Palaeomagnetism*, Chapman and Hall, London, 1983.

Tarling, D. H., and F. Hrouda, *The Magnetic Anisotropy of Rocks*, Chapman and Hall, London, 1993.

Thomsen, L., Weak elastic anisotropy, *Geophysics*, 51, 1954–1966, 1986.

Toft, P. B., J. Arkani-Hamed, and S. E. Haggerty, The effects of serpentinization on density and magnetic susceptibility: a petrophysical model, *Phys. Earth Planet. Inter.*, 65, 137–157, 1990.

Tommasi, A., B. Tikoff, and A. Vauchez, Upper mantle tectonics: three-dimensional deformation, olivine crystallographic fabrics and seismic properties, *Earth and Planetary Science Letters*, 168, 173–186, 1999.

Tong, C. H., R. S. White, M. R. Warner, and the ARAD working group, Effects of tectonism and magmatism on crack structure in oceanic crust: A seismic anisotropy study, *Geology*, 32, 25–28, 2004.

Ullemeyer, K., P. Spalthoff, B. Leiss, and K. Weber, Tof texture investigations of geological samples, *PHYSICA, B 276*, 878–879, 2000.

Van Buskirk, W. C., S. C. Cowin, and R. Carter Jr, A theory of acoustic measurement of the elastic constants of a general anisotropic solid, *J. Mater. Sci.*, 21, 2759–2762, 1986.

Vernik, L., and A. Nur, Ultrasonic velocity and anisotropy of hydrocarbon source rocks, *Geophysics*, 57, 727–735, 1992.

Vestrum, R. W., *Group and phase-velocity inversions for the general anisotropic stiffness tensor*, M. Sc. thesis, University of Calgary, 1994.

Weiss, T., S. Siegesmund, and T. Bohlen, Seismic, structural, and petrological models of the subcrustal lithosphere in southern germany: A quantitative revaluuation, *Pure and applied geophysics, 156*, 53–81, 1999.

Wendt, A. S., I. O. Bayuk, S. J. Covey-Crump, R. Wirth, and G. E. Lloyd, An experimental and numerical study of the microstructural parameters contributing to the seismic anisotropy of rocks, *J. Geophys. Res., 108(B8)*, No. 2365, 2003.

Wenk, H. R., Texture and anisotropy. plastic deformatin of minerals and rocks, *Reviews in Mineralogy and Geochemistry, 51*, 291–329, 2002.

Wenk, H. R., and P. Van Houtte, Texture and anisotropy, *Reports on Progress in Physics, 67*, 1367–1482, 2004.

Winterstein, D. F., Velocity anisotropy terminology for geophysicists, *Geophysics, 55*, 1070–1088, 1990.

Yaouancq, G., and C. J. Macleod, Petrofabric investigation of gabbros from the oman ophiolite: Comparsion between ams and rock fabric, *Marine Geophysical Researchs, 21*, 289–305, 2000.

Yin, H., *Acoustic velocity and attenuation of rocks: isotropy, intrinsic anisotropy, and stress induced anisotropy*, Ph.D. thesis, Stanford University, 1992.

# Appendix A

# Thin section

128

(a)
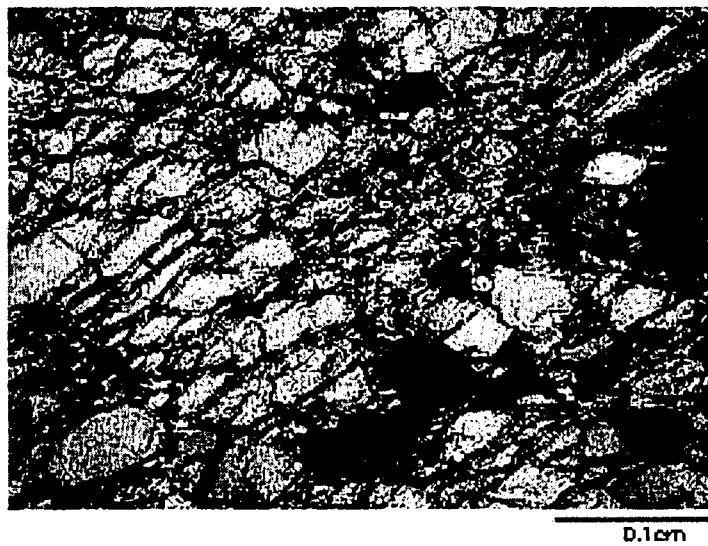


(b)

Figure A.1: Thin section of sample P 03-1; Top: Parallel to the foliation (×50). Bottom: Normal to the foliation (×50). Thin section were taken under crossed polars.

129

0. lcm

(a)



0.1cm
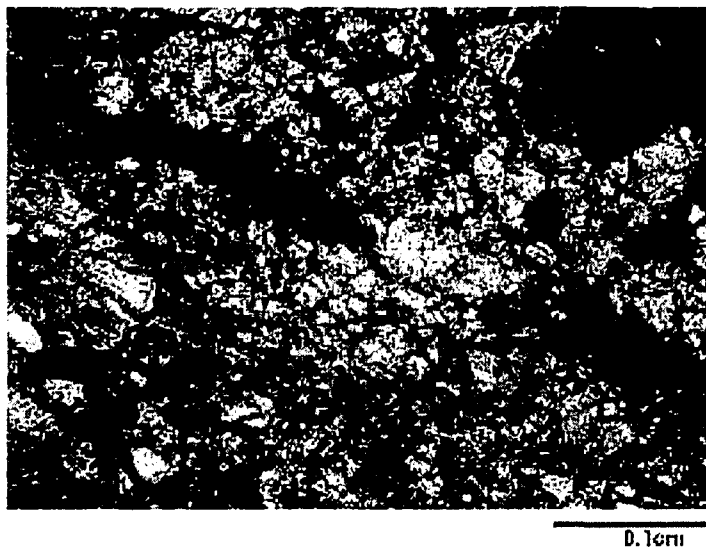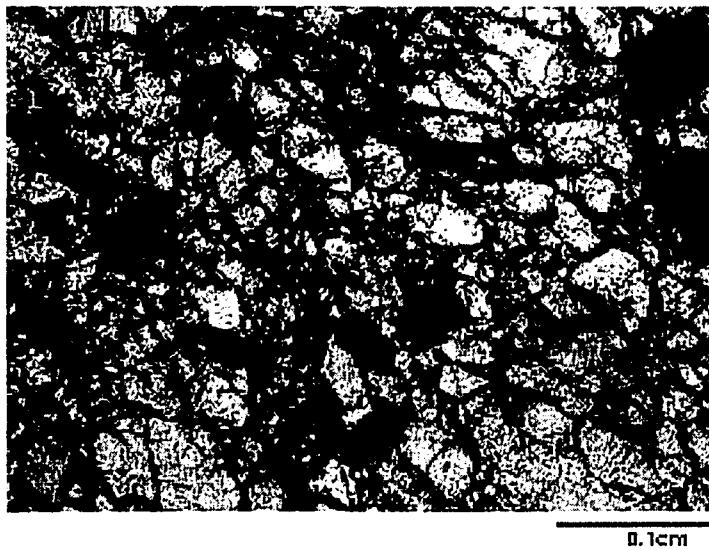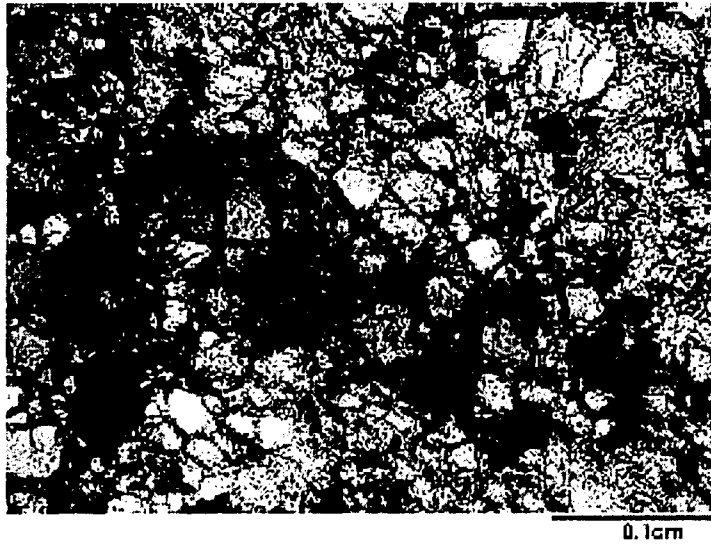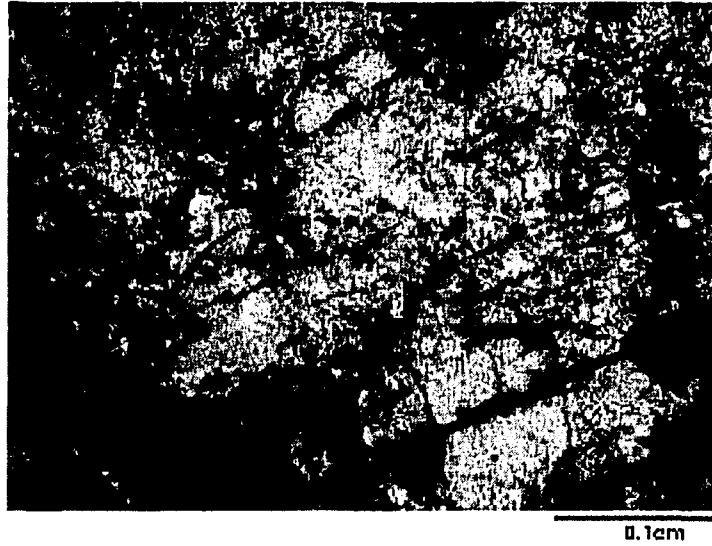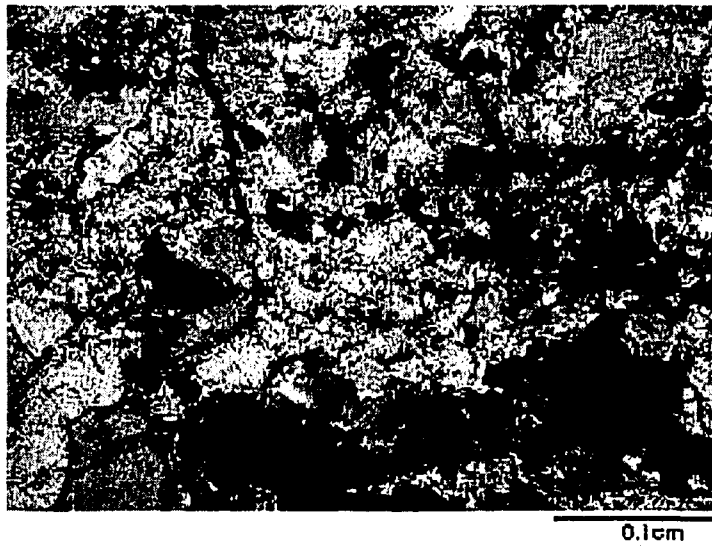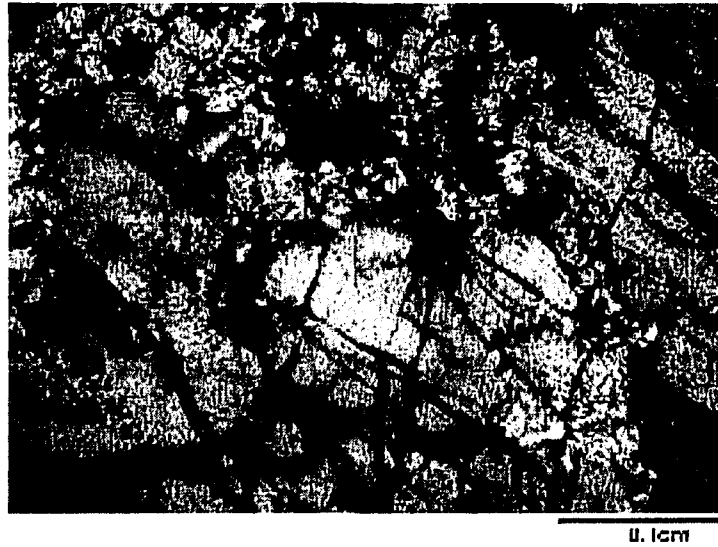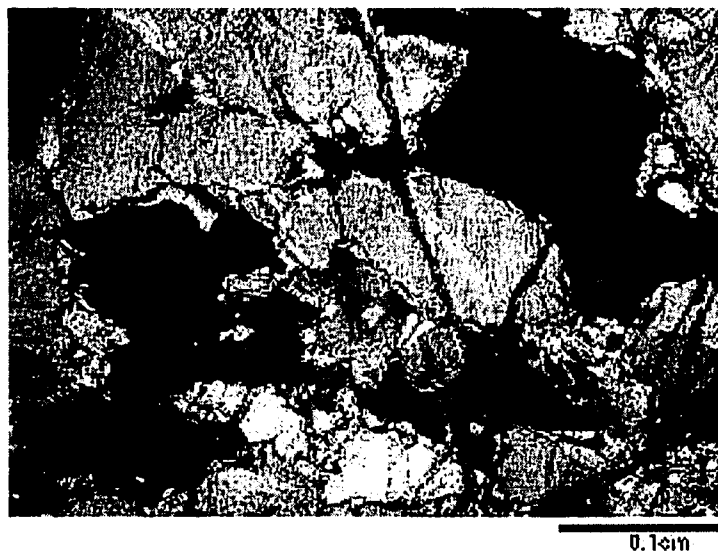
(b)

Figure A.2: Thin section of sample P 04-2; Top: Parallel to the foliation (×50). Bottom: Normal to the foliation (×50). Thin section were taken under crossed polars.
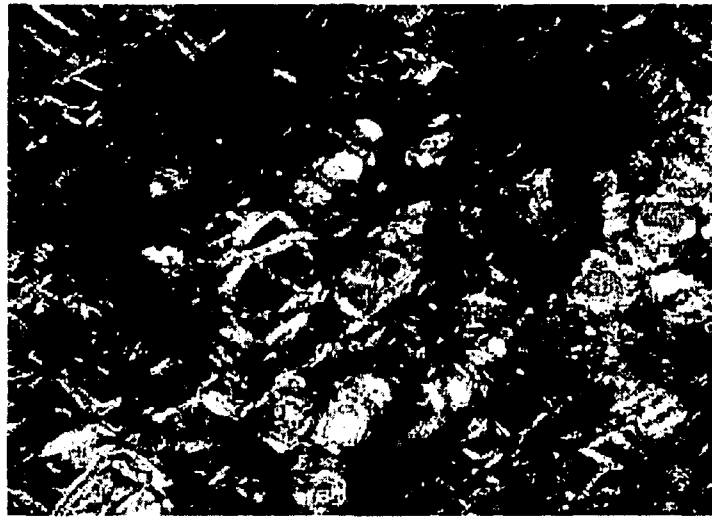
130

0.1cm

(a)



0.1cm

(b)

Figure A.3: Thin section of sample P 08-3; Top: Parallel to the foliation (×50). Bottom: Normal to the foliation (×50). Thin section were taken under crossed polars.

131

0.1cm

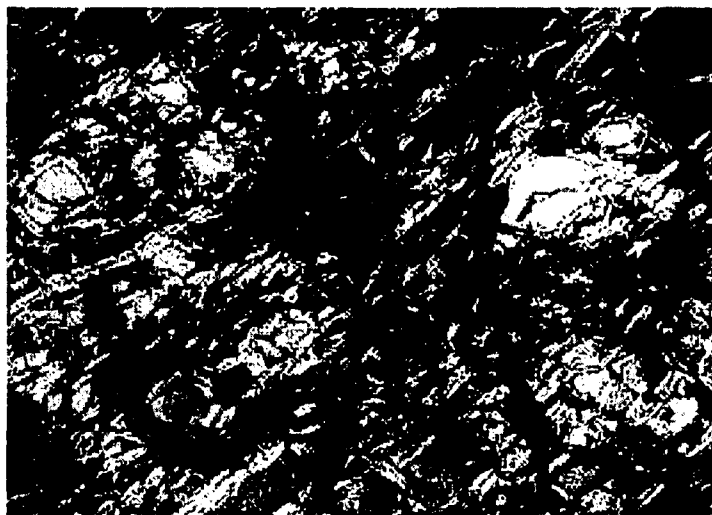Figure A.4: Thin section of sample P 08-4 (×50). Thin section were taken under crossed polars.
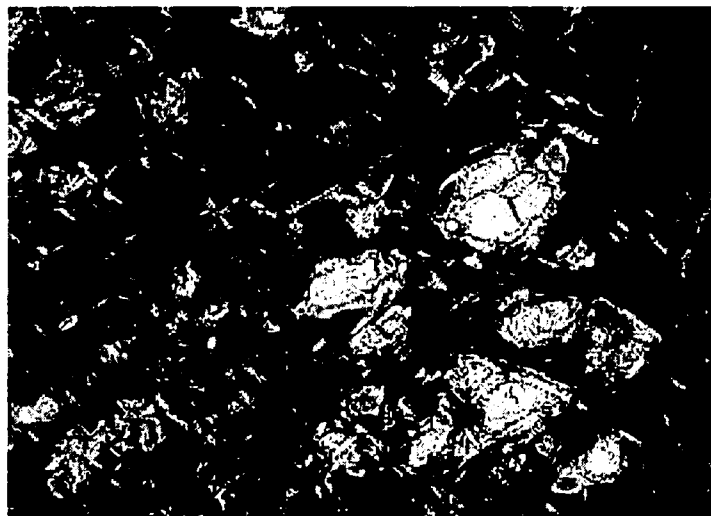
(a)



(b)

Figure A.5: Thin section of sample P 11-1; Top: Parallel to the foliation (×50). Bottom: Normal to the foliation (×50). Thin section were taken under crossed polars.

133

(a)



(b)

Figure A.6: Thin section of sample P 12-1; Top: Parallel to the foliation (×50). Bottom: Normal to the foliation (×50). Thin section were taken under crossed polars.

(a)



(b)

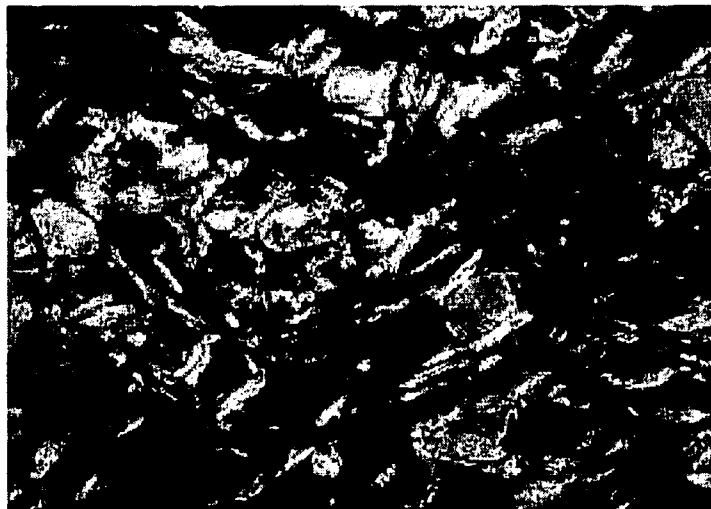Figure A.7: Thin section of sample P 13-1; Top: Parallel to the foliation (×50). Bottom: Normal to the foliation (×50). Thin section were taken under crossed polars.

(a)



(b)

Figure A.8: Thin section of sample P 13-2; Top: Parallel to the foliation (×50). Bottom: Normal to the foliation (×50). Thin section were taken under crossed polars.

(a)



(b)

Figure A.9: Thin section of sample P 16-3; Top: Parallel to the foliation (×50). Bottom: Normal to the foliation (×50). Thin section were taken under crossed polars.
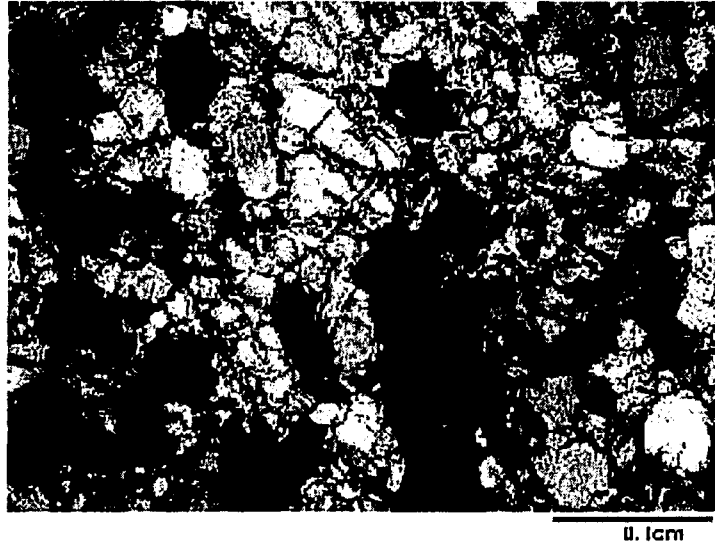
137

U. Icm

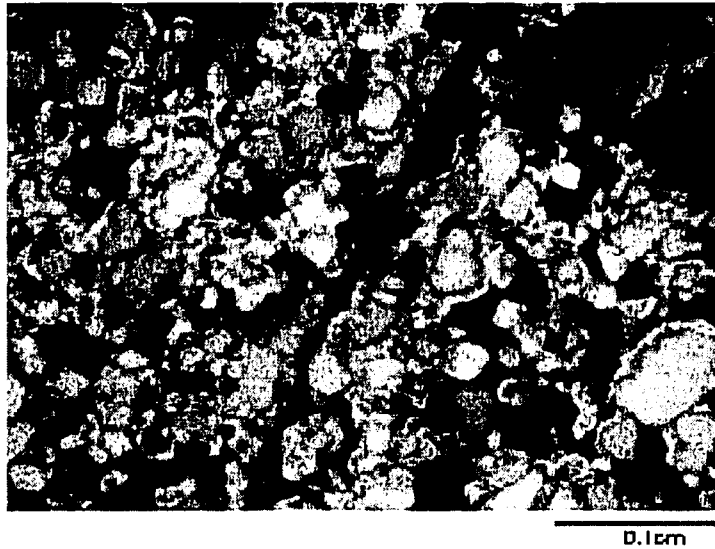Figure A.10: Thin section of sample V 03-11 (×50). Thin section were taken under crossed polars.



D. Icm

Figure A.11: Thin section of sample V 03-7 (×50). Thin section were taken under crossed polars.

138

139